TIME-RESOLVED MEASUREMENTS OF THE UNDERPOTENTIAL DEPOSITION OF COPPER ONTO PLATINUM(111) IN THE PRESENCE OF CHLORIDE

A Dissertation

Presented to the Faculty of the Graduate School

of Cornell University

in Partial Fulfillment of the Requirements for the Degree of

Doctor of Philosophy

by

Adam Craig Finnefrock

August 1998

TIME-RESOLVED MEASUREMENTS OF THE UNDERPOTENTIAL DEPOSITION OF COPPER ONTO PLATINUM(111) IN THE PRESENCE OF CHLORIDE

Adam Craig Finnefrock, Ph.D.

Cornell University 1998

We have studied *in situ* the ordering of a two-dimensional Cu–Cl crystal electrodeposited on a Pt(111) surface. We simultaneously measured high-resolution time-resolved x-ray scattering and chronoamperometric (current vs. time) transients. Both measurements were synchronized with the leading edge of an applied potential step that stimulated the desorption of Cu and subsequent ordering of the Cu–Cl crystal. In all cases, the current transient occurs on a shorter time-scale than the development of crystalline order. The time-dependent x-ray intensity data (2×10^4 data points) are well fit by an Avrami-like function with only three parameters. By performing a series of voltage-step experiments, we demonstrate that the ordering time diverges with applied potential ϕ as $\tau \sim \exp[1/(\phi - \phi_0)]$, consistent with the nucleation and growth of two-dimensional islands. Monitoring the time-dependent widths of the x-ray peak, we see a narrowing corresponding to the growing islands.

BIOGRAPHICAL SKETCH

Adam Craig Finnefrock was born in Long Beach, California in 1970. Before the age of 18, his family had moved over a dozen times. In spite of this emotional trauma (or perhaps, because of it) the young preppie left New England to study in Houston, Texas in 1987. He graduated from Rice University with bachelor degrees in Physics and Mathematical Sciences in May 1992. He matriculated to Cornell University and joined Professor Joel Brock's research group in late 1992. He will be taking a postdoctoral position with Professor Sol Gruner, where he will attempt to overcome his crushing ignorance of all things biological. The culpability for his questionable choice of career resided on his parents' bookshelves, teeming with optimistic science fiction from the '60s and early '70s.

ACKNOWLEDGEMENTS

The results presented in this dissertation would not be possible without the assistance of many people.

First, I have worked in the laboratories of Joel Brock for the past six years. Alternately serving as teacher, taskmaster, advisor, and friend, he has provided the motivation and means for all of the work described herein. He has been extremely generous with his time, and has taught me most of my experimental skills, and what I know of x-ray scattering.

Professor Abruña has been my unofficial mentor. A primary collaborator, he has also given me excellent advice throughout and helped me to find the "larger picture". He has also provided courage (and food, occasionally) in the face of hardship, on and off of the beamline. His advice on the entire academic process was invaluable.

Lisa Buller has been my counterpart in the research group of Professor Abruña. Her assistance was crucial, especially during the earliest stages of this project, where hours were long and data were few. She has provided for the practical aspects of the electrochemical results described herein.

Kristin Ringland has been an enormous help throughout this project. She has been present for virtually all of the data acquisition and has assisted in many other ways too numerous to detail. Throughout the rigors of grim and intense synchrotron runs, she has uttered not even one complaint. As has been remarked, she is still probably “the perfect graduate student”. Arthur Woll has been a constant friend in the lab, and I have appreciated his good humor throughout. He and I have had many discussions on x-ray scattering from surfaces, and have discussed the need for a comprehensive treatment that we can understand. I hope to see more about this in his dissertation. Emma Sweetland, the first student to graduate, helped me through the earliest years. She is also responsible for much of the laboratory infrastructure that we often take for granted.

Samantha Glazier was the newest member of this collaboration. Her dauntless enthusiasm and relentless curiosity have been refreshing for us veterans. I would also like to thank two other x-ray electrochemists. Mike Toney of IBM gave me some early encouragement and practical advice on cell design and x-ray measurements. Ben Ocko of NSLS has also given me lots of advice, and acted as the most steadfast critic. Jean Jordan-Sweet at IBM has been responsible for the beamline where this x-ray data was taken. Supervising the steady stream of users, ensuring that the beamline is ready for use, and repairing the broken/altered equipment afterwards is a thankless job. I would like to thank her for it.

I would like to thank the members of my special committee, who have taken the time to read this dissertation, and are likely to be the ones to ever do so. (Though if you are reading this, who knows?) I really appreciated their comments and careful readings; they have made this dissertation far better and more readable that I could have done alone. I would particularly like to thank the Chair, Carl Franck, for his encouragement, support, and advice (particularly on the choice of postdoctoral appointments) throughout most of my graduate studies. I also would like to thank him for hosting the Easy Physics seminars, which have been an interesting staple of my physics diet.

This would not be possible without my family, who got me to this stage in the first place and gave me the tools to continue. Jennifer Mass, my fianceé, has helped me through this dissertation from the other side of a Ph.D. I could not have made it without her patience and support throughout the entire process. I would simply be lost without her.

The U.S. taxpayer has provided generously, if somewhat unwittingly, for this research. This work was supported by Cornell's Materials Science Center (NSF Grant No. DMR-96-32275). Additional support was provided by the NSF (Grant Nos. DMR-92-57466 and CHE-94-07008) and the Office of Naval Research. The x-ray data were collected at the Cornell High Energy Synchrotron Source (CHESS), which is supported by the National Science Foundation (Grant No. DMR-93-11772), and at the IBM–MIT beam line X20A at the National Synchrotron Light Source (NSLS), Brookhaven National Laboratory. NSLS is supported by the U.S. Department of Energy, Division of Materials Sciences and Division of Chemical Sciences. (Contract No. DE-AC02-76CH00016).

Table of Contents

List of Tables

List of Figures

Chapter 1

Introduction

The electrodeposition of a metal adsorbate onto a solid surface is a key aspect of important technological processes such as electroplating and corrosion inhibition. In a number of cases, metal overlayers can be electrodeposited onto a dissimilar metal substrate at a potential that is less negative than the Nernst potential (that required for bulk deposition). Experimentally, this "underpotential deposition" (UPD) provides a precise means for quantitatively and reproducibly controlling coverage in the submonolayer to monolayer (and in some cases multilayer) regime [89, 7, 128].

The initial stages of adsorption/deposition, along with the growth mechanism, dictate the structure and properties of the deposit. UPD is an important experimental technique for investigating the early stages of deposition, and the diverse factors that influence it, for several reasons. First, in contrast to vacuum-surface experiments, the electrochemical interface provides direct control over the chemical potential of adsorbed species. This has been recently exploited by Ocko and coworkers [105] to study two-dimensional Ising lattice dynamics. Second, the charged double-layer (section 2.3) produces enormous (up to 10^7 V/cm) electric fields, capable of driving surface rearrangements [106]. Third, UPD is generally reversible. Thus, it is possible to perform repeated measurements of a deposition/desorption transition using the same sample and systematically varying the control parameters.

The strongest interaction in a UPD process is between the metal to be deposited and the substrate [89, 6, 51]. Thus, UPD is usually restricted to the deposition of one monolayer prior to the onset of bulk deposition; in some systems, however, up to three atomic layers can be deposited. Although the metal-substrate interaction usually dominates, other interactions can also be important. For example, strongly adsorbing anions in the electrolyte are particularly important as both anion-metal and anion-substrate interactions significantly affect UPD processes. Furthermore, the adsorbed species rarely loses its charge completely during the early stages of deposition [119, 120, 149, 129, 94, 155, 156]. Rather, it becomes completely reduced only when the applied potential is close to the Nernst potential. This variable charge state alters the electrostatic interaction between the deposit and the anions. At more positive potentials, there is a strong attractive electrostatic interaction that disappears as the metal is discharged. This attractive interaction can produce a metal-anion bilayer on the electrode surface at intermediate potentials [156, 123, 91, 133, 131].

In addition to the surface coverage, both the presence of other adsorbates, especially anions, and the surface structure of the substrate can profoundly affect the structural and electronic characteristics of the deposit [90, 149, 94, 150, 71]. Although there is a great deal of existing work on UPD lattice formation, the early stages of deposition are not well-understood [121, 33]. In much of this earlier work, the structure of a UPD overlayer was determined by transferring the electrode into an ultra-high vacuum (UHV) chamber and employing established surface science techniques such as low-energy electron diffraction (LEED). However, such measurements are inherently *ex situ* and cannot provide information on the kinetics of deposition.

Recently, *in situ* probes such as scanning tunneling microscopy (STM) [92, 64, 76], atomic force microscopy (AFM) [93], and surface x-ray scattering (SXS) [101, 132, 133, 139, 140, 107] have been applied to UPD systems. In addition to eliminating the ambiguity of *ex situ* measurements, they offer the possibility of studying the kinetics of deposition. Kinetic studies are crucial for identifying the rate-limiting steps in the electrochemical growth of not only metals but also of technologically relevant materials such as GaAs [136] and CdTe [135]. Such studies can also provide important tests of the large body of theoretical work on nonequilibrium statistical physics, especially on the kinetics of growing surfaces and interfaces [17].

The UPD of metal overlayers onto single crystal electrodes provides an excellent family of experimental systems for studying fundamental aspects of materials growth. In particular, Cu UPD on Pt(111) has been extensively studied by a variety of techniques. The process is very sensitive to the presence of anions and appears to be kinetically controlled. The exact structure and nature of the overlayer, particularly at intermediate coverages, has been the subject of some controversy. Based on

LEED studies, Michaelis *et al.* [102] identified the intermediate overlayer as a 4×4 structure. However, more recent *in situ* anomalous x-ray diffraction measurements of the overlayer structure as a function of potential by Tidswell *et al.* [131] indicate that the intermediate overlayer structure is a more complicated incommensurate CuCl bilayer.

Surface x-ray scattering techniques have been previously applied to UPD. For example, Toney and coworkers have studied Pb, Tl, and Cu UPD on Ag and Au surfaces [101, 132, 133]. In addition, Ocko and coworkers have studied a variety of equilibrium surface structures as a function of both the solution concentration of the adsorbate (especially anions) and the surface charge, with emphasis on gold substrates [139, 140, 107]. However, all of these studies have been static in nature and have not addressed the kinetics of adlayer formation. This is due, in part, to the severe experimental challenges that such measurements present.

Time-resolved surface x-ray scattering represents a nearly ideal probe for studying the time evolution of the overlayer structure during UPD. X rays in the 0.5 Å to 1.5 Å region are not significantly absorbed by aqueous solutions allowing for the *in situ* study of the electrode/solution interface. In addition, the line shape of the scattered x rays can be interpreted simply in terms of well-known correlation functions, allowing direct tests of theory. Using signal averaging techniques, transient structures with lifetimes as short as a few microseconds can be studied [127].

In this dissertation, I report the first time-resolved surface x-ray scattering measurements of metal electrodeposition. The specific system chosen system is the UPD of Cu^{2+} onto Pt(111) in the presence of Cl^- anions. Some of the results have been already published [65, 78, 5, 66]; inclusion of these results in this dissertation is with the written permission of these journals.

To my knowledge, these are the only time-resolved x-ray measurements of any UPD process. This is not surprising, because these measurements are extremely difficult to perform. UPD is extremely sensitive to contaminants, requiring special protocols and rigorous cleanliness throughout the preparations of the sample, the solutions, and the electrochemical cell. To observe the scattering from only a single monolayer, a synchrotron x-ray source is necessary. Additional scattering from the solution and the film that contains it can easily overwhelm the signal of interest. These considerations imply that static x-ray scattering measurements from the UPD layer are quite difficult. Compounding this by performing time-resolved measurements of the nonequilibrium UPD system adds another challenge. The signal to noise ratio must be sufficiently high in each time bin to obtain useful data. This ratio can be improved by depositing the UPD layer under voltage control, and then pulling out most of the solution. This is the traditional method for studying UPD structures *in situ*. However, this configuration completely prevents further manipulation of the UPD layer; the contact between the sample face and the other electrochemical electrodes is diminished. The kinetics of the UPD formation or dissolution are then completely inhibited.

Because of all these difficulties, the conventional wisdom was that time-resolved x-ray scattering measurements of UPD were not possible. To resolve these challenges, we had to develop and successively improve several aspects of our experiment. The first and most dramatic improvement came in the observation that annealing the sample at high temperature for up to an hour dramatically improved the crystal mosaic (an indication of the size and relative alignment of domains within the crystal). Similar behavior has been observed in single noble metal crystals in UHV [69]. The next limitation was the misorientation of our samples' faces with respect to the crystal axis. Ultimately, this imposed a constraint on the maximum terrace size. Following Joel Brock's suggestion, I designed a crystal polishing apparatus that could orient the sample in any arbitrary direction with a precision of $0.001°$. The sample could be repolished along this axis, producing a crystal face with the desired orientation. (Other experimental groups in Clark Hall have adopted our design and procedures to obtain dramatic improvements in sample quality.) Lisa Buller had a electrochemical cell built, based upon Mike Toney's original design. The final challenge was to interface the potentiostat to the rest of our timing hardware and software. This involved months of programming and testing.

After overcoming these challenges, we were able to obtain very useful and interesting data. We have studied *in situ* the ordering kinetics of the two-dimensional Cu–Cl crystal electrodeposited on a Pt(111) surface. We simultaneously measured high-resolution time-resolved x-ray scattering and chronoamperometric (current vs. time) transients. Both measurements were synchronized with the leading edge of an applied potential step that stimulated the desorption of Cu and subsequent ordering of the Cu–Cl crystal. In all cases, the current transient occurred on a shorter timescale than the development of crystalline order. The time-dependent x-ray intensity data (2×10^4 data points) were well fit by an Avrami-like function with only three parameters. By performing a series of voltage-step experiments, we demonstrated that the ordering time diverged with applied potential ϕ as $\tau \sim \exp[1/(\phi - \phi_0)]$, consistent with the nucleation and growth of two-dimensional islands. Monitoring the time-dependent widths of the x-ray peak, we observed a narrowing corresponding to the growing islands.

This dissertation is organized into chapters as follows. Chapters 2 and 3 are introductory in nature. Chapter 2 is an introduction to electrochemistry, specifically oriented to the phenomenon of UPD. It is aimed at a physicist who may be unfamiliar with electrochemical phenomena, and the presentation is from a fundamental perspective. Wherever possible, I have made analogies to examples familiar to most physicists. Chapter 3 is a derivation of some x-ray phenomena, starting with the classical x-ray scattering from an electron.

The experimental apparatus and procedures are documented in chapter 4. These include sample preparation and data acquisition procedures. Static x-ray measurements and their subsequent analysis are in chapter 5. Kinetic (time-resolved) x-ray and chronoamperometric (current vs. time) measurements are found in chapter 6. These data are analyzed in terms of a nucleation and growth model. Finally, conclusions are presented in chapter 7. Long derivations and discussions are relegated to the appendices.

Chapter 2

Introduction to Electrochemistry

2.1 Introduction

In this chapter, I will introduce and discuss some of the rudiments of electrochemistry from a physics perspective. The first section introduces the electrochemical potential. The second section concerns the nature of the electrode – solution interface, and discusses several models for the electric charged double-layer. Then, the behavior and transport of ions in solution is discussed. The following sections describe bulk deposition and underpotential deposition. Finally, specific adsorption is explained and adsorption isotherms are examined.

What is electrochemistry? I like the definition with which Schmickler [114] begins his recent book:

> Electrochemistry is the study of structures and processes at the interface between an electronic conductor (the electrode) and an ionic conductor

(the electrolyte) or at the interface between two electrolytes.

The first electrochemical experiments were also some of the first biophysical experiments. These are the famous studies of electrified frog legs, performed by Luigi Galvani [68, 67]. Since then, experimental science has fragmented into a multitude of disciplines and spawned many industries. Presently, electrochemical processes are crucial to a wide variety of commercial processes. These include batteries, which are of great importance in the quest for low-emission electric vehicles. Corrosion is an electrochemical process under active study, especially in industry. Electroplating, for either the prevention of oxidation, or coating one metal with a more precious one (such as in jewelry) is another process of importance. Recently, specific multilayer semiconductor structures have been electrochemically synthesized.

Two more examples illustrate the importance of electrochemistry. Electroanalytic processes alone account for $68.2 billion worldwide [134]. The primary products include chlorine, aluminum, copper, and sodium hydroxide. Electrolysis of water is still used in Europe to produce high purity hydrogen and oxygen. The global production of aluminum consumes the same amount of electricity as 10% of the United States electricity sales. Electrochemistry is also crucial to electrochemical biosensors, which are now used in medical settings. They monitor the concentrations of various gases dissolved in the blood (such as carbon dioxide, oxygen, pH) or electrolyte levels (sodium, potassium, calcium, chloride). These sensors are portable and give continuous real-time results at the patients' bedside. Previously, the alternative was to periodically take blood samples and send them to the hospital lab for analysis.

2.2 Electrochemical Potential

In analogy to the chemical potential μ_i, let us define the electrochemical potential of species i with charge q_i in an electric potential ϕ [22]:

$$\widetilde{\mu}_i = \mu_i + q_i\phi \; . \tag{2.1}$$

Obviously, for a neutral species, the electrochemical potential and the chemical potential are identical.

For convenience, chemists often separate the chemical potential into a concentration-dependent term and a concentration-independent term.

$$\mu_i(T, c_i) = \mu_{0,i}(T) + kT \ln a_i(T, c_i) \tag{2.2}$$

where a_i is called the *chemical activity* of species i. Values for the standard chemical potentials $\mu_{0,i}$ are tabulated in the chemical reference literature. Although only T is listed here, the chemical potential may depend upon numerous parameters (pressure, pH, etc.), depending upon the nature of the experiment.

This separation in (2.2) is reminiscent of the isolation of the pressure-dependent terms in gas mixtures:

$$\mu_i(T, p) = \mu_{0,i}(T) + kT \ln(p_i/p_{0,i}) \; , \tag{2.3}$$

where the pressures p_i take the place of the concentrations c_i and the pressure ratios $p_i/p_{0,i}$ take the place of the activities a_i. For ideal gases, $p_{0,i} = 1$, and the chemical potential of an ideal gas is recovered [96],

$$\mu_i(T, p) = \mu_{0,i}(T) + kT \ln p_i \; . \tag{2.4}$$

Likewise, we define the *activity coefficients* γ_i,

$$a_i = \gamma_i c_i \ , \tag{2.5}$$

and require that $\gamma_i = 1$ for an "ideal" solution (like an ideal gas, there is no interaction among ions of species i), such that the analogous equation obtains:

$$\mu_i(T, c_i) = \mu_{0,i}(T) + kT \ln c_i \ . \tag{2.6}$$

This approximation is expected to hold in the limit of very dilute solutions ($c_i \to 0$), or when the ions are well-screened.

Returning to the electrochemical potential (2.1), the definition of chemical activity (2.2) can be incorporated as

$$\widetilde{\mu}_i = \mu_{i,0} + kT \ln a_i + q_i \phi \tag{2.7}$$

For a pure phase (for instance, a solid metal electrode), the activity is unity and $\widetilde{\mu}_i = \mu_{i,0}$. The electrons within that metal have an electrochemical potential $\widetilde{\mu}_{e^-} = \mu_{e^-,0} - \phi$. Their concentration never varies appreciably, so we can ignore the effects of activity within the metal.

2.3 Electrode – Solution Interface

A complete model of the electric double layer [23, 39, 115] was given by Bockris, Devanathan, and Müller [34]. This is illustrated in figure 2.1. It contains positively charged species adsorbed onto the electrode, polar solvent (water) molecules, and solvated species both near and far from the electrode surface. We will take these components in turn, and gradually build up to this complex arrangement.

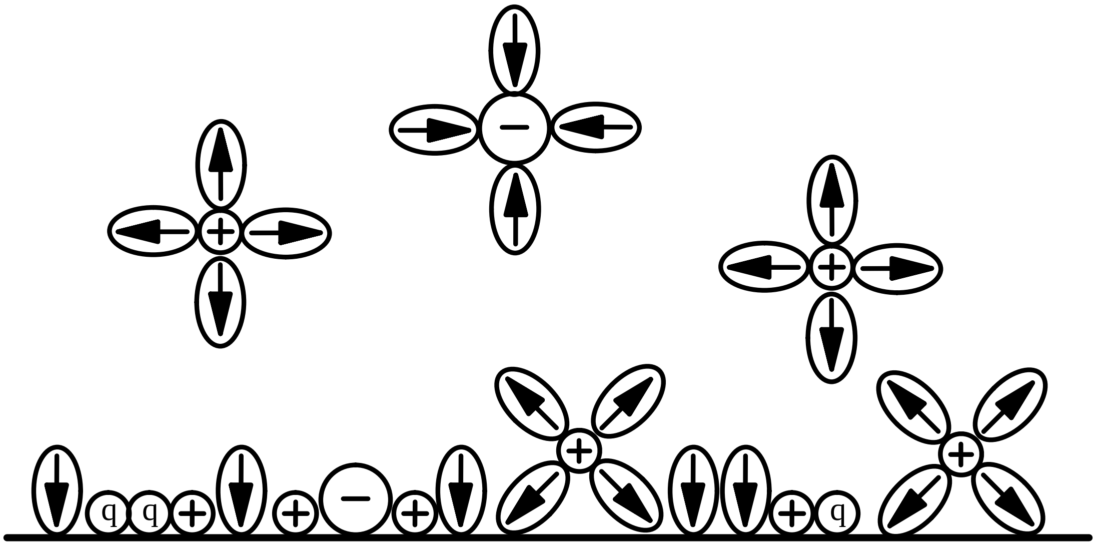

Figure 2.1: BDM model of charged double layer. Adapted from [38, 18]. The polar solvent molecules are shown as ellipses, with the arrows pointing toward the positive end. The specifically adsorbed (section 2.7) ions of indeterminate charge are labeled as "q". Note that some of the ions are solvated, which limit the closest approach distance.

If we apply a negative charge onto our electrode surface, then it will attract positive ions from solution. This will have the effect of making the charge of the electrode appear to be less negative to a test charge deep in the bulk solution. This "charge screening" is exactly analogous to the screening of point particles described by Debye, which is present in a broad range of physical contexts. Charge screening is discussed again in section 2.4.

Throughout this section, the potential far from the electrode (in the "bulk solution") is set to zero. Relative to this potential, the electrode is at an electric potential ϕ_0.

The earliest model of the double layer was proposed by Helmholtz [137, 138] in 1879. He considered just the a layer of positively charged ions, tightly bound to the negatively charged electrode surface. The centers of these ions were postulated to lie on a single "Helmholtz" plane at a distance z_H from the electrode surface. The resulting potential is identical to that within a capacitor, and is a linear interpolation between the electrode and bulk potentials, as shown in 2.2.

$$\phi(z) = \begin{cases} \phi_0 \left(1 - \frac{z}{z_H}\right) & z \leq z_H \\ 0 & z \geq z_H \end{cases} \tag{2.8}$$

In analogy with a parallel-plate capacitor, the capacitance is a constant independent of voltage. This is in conflict with experimental observations, indicating that this model is incomplete.

An entirely opposite approach was undertaken by Gouy in 1910 [73] and Chapman in 1913 [54]. They proposed that none of the ions were tightly bound to the surface. Each ion is not constrained to lie in a tight double layer, but is sensitive to

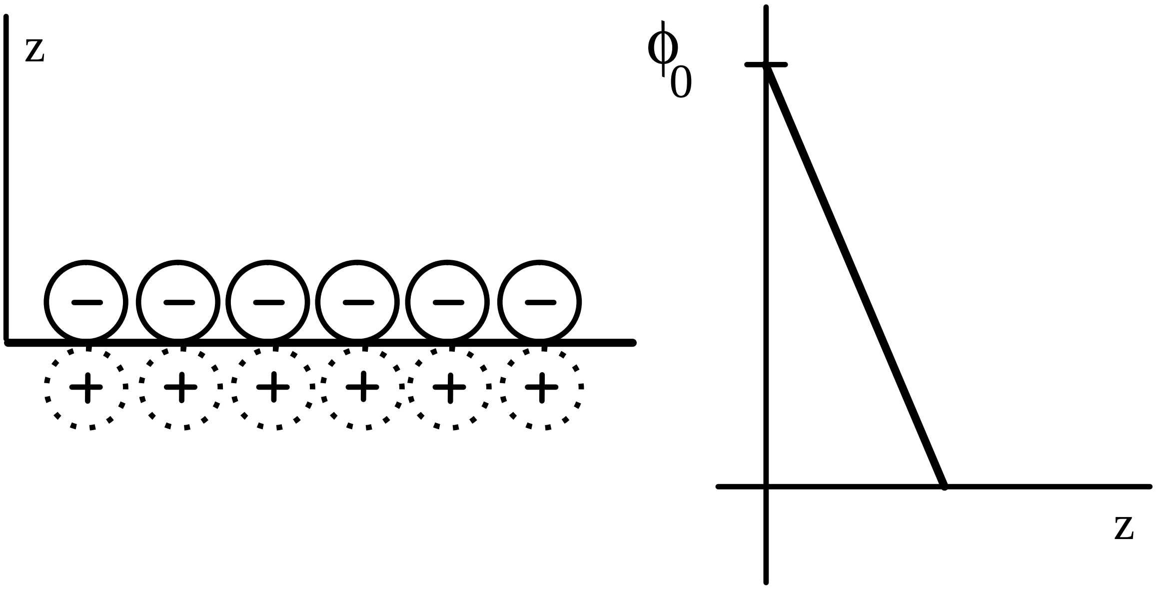

Figure 2.2: (a) Diagram of the Helmholtz model. The negative ions adsorbed onto the surface are shown with solid lines. The positive “image” charges are shown with dotted lines. (b) Potential ϕ vs. distance z from the electrode.

the electric potential formed by the other ions. In this way, the positions of the ions are not predetermined, but are the result of a statistical equilibrium with respect to this potential. This is only a mean-field model; individual ions are expected to react only to the overall field produced by all the other ions.

This mean-field model can be analyzed with some rigor. First, the electric potential ϕ depends on the charge density ρ as stated by Poisson's equation (in Gaussian units),

$$\frac{d^2\phi^2}{dz^2} = -\frac{4\pi\rho}{\epsilon} \tag{2.9}$$

where the ϵ is the dielectric constant of the solution.

The charge density is the sum of the charges from species i

$$\rho(z) = \sum_i q_i c_i(z) \ . \tag{2.10}$$

In equilibrium, each charge density follows a Boltzmann distribution, determined by the mean field $\phi(z)$,

$$c_i(z) = c_i(z = \infty) \exp \frac{-q_i\phi(z)}{kT} \tag{2.11}$$

Combining these two equations leads to the Poisson-Boltzmann equation

$$\frac{d^2\phi^2}{dz^2} = -\frac{4\pi}{\epsilon} \sum_i q_i c_i(z = \infty) \exp \frac{-q_i\phi(z)}{kT} \tag{2.12}$$

Using the relation

$$\frac{d^2\phi^2}{dz^2} = \frac{1}{2}\frac{d}{d\phi}\left(\frac{d\phi}{dz}\right)^2 \tag{2.13}$$

we can rewrite (2.12) and integrate to find

$$\left(\frac{d\phi}{dz}\right)^2 = \frac{8\pi kT}{\epsilon} \sum_i c_i(z = \infty) \exp \frac{-q_i\phi(z)}{kT} + \text{constant} \tag{2.14}$$

To solve for the constant, we apply the boundary conditions that far from the electrode the potential and its derivative fall to their bulk value (zero). That is,

$$\begin{aligned} \lim_{z\to\infty} \phi(z) &= 0 \qquad (2.15) \\ \lim_{z\to\infty} d\phi(z)/dz &= 0 \qquad (2.16) \\ & \qquad (2.17) \end{aligned}$$

Then, (2.14) becomes

$$\left(\frac{d\phi}{dz}\right)^2 = \frac{8\pi kT}{\epsilon} \sum_i c_i(z=\infty) \left(\exp \frac{-q_i\phi(z)}{kT} - 1\right) \qquad (2.18)$$

In order to continue and keep the equations manageable, it is helpful to restrict the discussion to a "symmetrical" electrolyte. These are also called $z : z$ electrolytes, because they consist of only one cationic and one anionic species, of equal charge magnitude (often denoted z). The electrolyte used in these experiments, $HClO_4$ (which dissociates into H^+ and $(ClO_4)^-$), is an example of a symmetrical electrolyte. Then (2.18) becomes

$$\left(\frac{d\phi}{dz}\right)^2 = \frac{16\pi kTc_\infty}{\epsilon} \left(\cosh \frac{q\phi(z)}{kT} - 1\right) \qquad (2.19)$$

where c_∞ denotes the common $c_i(z = \infty)$, and q the magnitude of the charges. Taking the square root,

$$\frac{d\phi}{dz} = -\left(\frac{32\pi kTc_\infty}{\epsilon}\right)^{1/2} \sinh \frac{q\phi(z)}{2kT} \qquad (2.20)$$

We take the negative square root by our assumption that the electrode sits at a positive potential with respect to the bulk solution. Substitute

$$\psi = \frac{q\phi(z)}{2kT} \qquad (2.21)$$

to rewrite (2.20) as

$$\frac{d\psi}{dz} = \kappa \sinh \psi \tag{2.22}$$

where we have also substituted for the inverse of the "Debye length"

$$\frac{1}{L_{\text{Debye}}} = \kappa = \left(\frac{8\pi q^2 c_\infty}{\epsilon kT}\right)^{1/2}. \tag{2.23}$$

The significance of this length will become apparent below. Rewriting as

$$\int \frac{d\psi}{\sinh \psi} = \int dz\ (-\kappa) \tag{2.24}$$

and then integrating,

$$\ln \tanh \psi/2 = -\kappa z + \text{constant} \tag{2.25}$$

The constant can be determined by using $\psi(z=0) = \psi_0$, and then

$$\frac{\tanh(q\phi/4kT)}{\tanh(q\phi_0/4kT)} = \exp(-\kappa z) \tag{2.26}$$

In the limit that $\phi_0 \to 0$, we obtain

$$\phi = \phi_0 \exp(-\kappa z) \tag{2.27}$$

For aqueous solutions, $\epsilon = 78.49$ [24] at 25°C, and then $\kappa = 3.29 \times 10^7 (q/e) c_\infty$, where κ is given in cm^{-1} and c_∞ in M (moles/liter). Our electrolyte is 0.1 M $HClO_4$, so $\kappa = 3.3 \times 10^6\ \text{cm}^{-1}$ or 3.3×10^{-2} Å^{-1}. This constitutes an enormous voltage gradient, on the order of 10^6 to 10^7 V/m.

The Gouy-Chapman model is an improvement over the Helmholtz model, but it does not take into account the finite size of ions. There must be a plane of closest approach, just as predicted by Helmholtz. The minimum distance of this plane

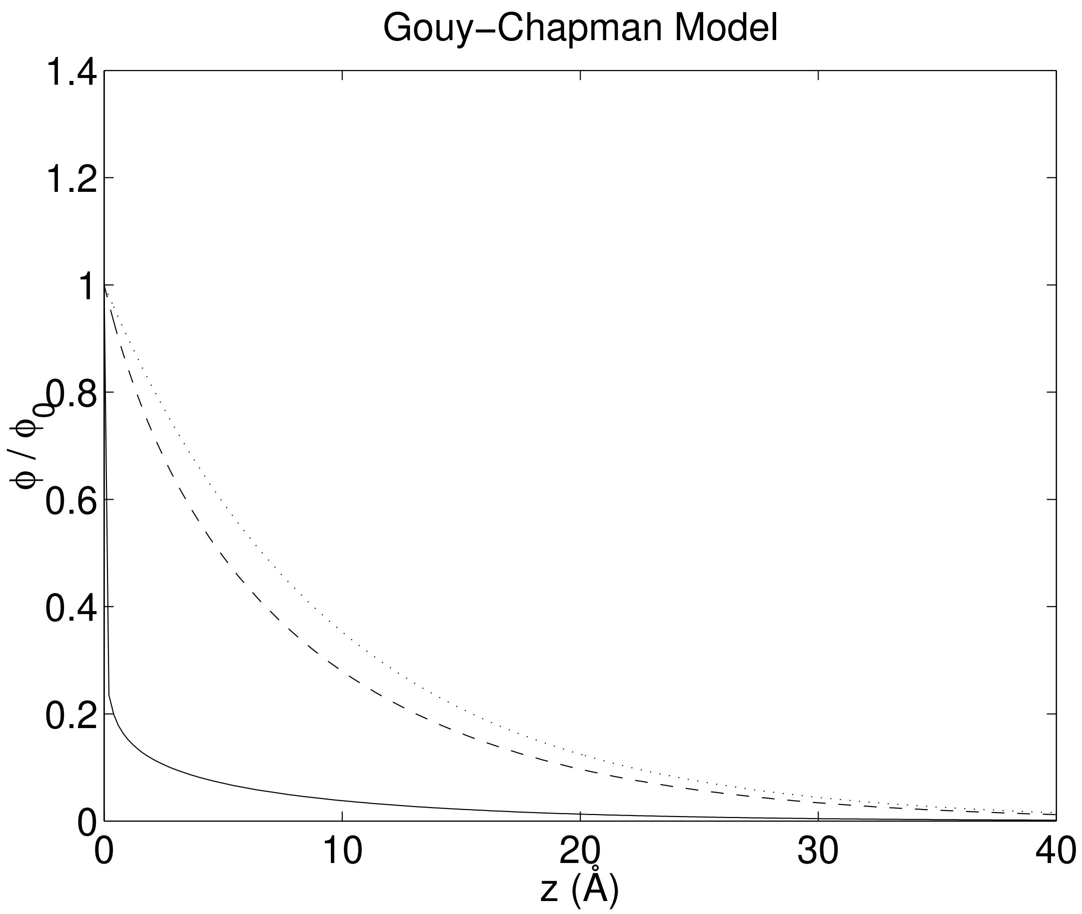

Figure 2.3: Normalized potential profiles ϕ/ϕ_0 vs. z for the Gouy-Chapman model at $\phi_0 = 1000$ mV (solid), 100 mV (dashed), 10 mV (dotted). The $\phi_0 = 10$ mV case is indistinguishable from the $\phi_0 \to 0$ limiting form (2.27) . Note that larger values of ϕ_0 have steeper descents. I have used the case of 0.1 M $HClO_4$, just as in the experiments described later. For this case, the Debye length is $L_{\text{Debye}} = 9.6$ Å. Adapted from a similar figure in [19].

from the electrode surface is the ionic radii. If the ions are solvated, then they will not even be able to approach that closely. Stern realized this in 1924 [125] and proposed a model to incorporate this. Essentially, it is a combination of the two previous models.

Call the distance of closest approach z_{OHP}. (OHP stands for "Outer Helmholtz Plane". The "Inner" plane will be defined shortly.) The Helmholtz description applies for $z \leq z_{\mathrm{OHP}}$, and the Gouy-Chapman description applies for $z \geq z_{\mathrm{OHP}}$. At this boundary, we require continuity in the potential ϕ_{OHP} and its derivative. In the $z \leq z_{\mathrm{OHP}}$ region, we have the Helmholtz linear potential drop

$$\phi(z) = \phi_0 - \left.\frac{d\phi}{dz}\right|_{\mathrm{OHP}} z \tag{2.28}$$

In the $z \geq z_{\mathrm{OHP}}$ region, the potential follows the previous Poisson-Boltzmann result, but displaced by z_{OHP},

$$\frac{\tanh(q\phi/4kT)}{\tanh(q\phi_{\mathrm{OHP}}/4kT)} = \exp[-\kappa(z - z_{\mathrm{OHP}})] \tag{2.29}$$

If we choose z_{OHP}, then we can find ϕ_{OHP} by applying (2.20) and (2.28) at $z = z_{\mathrm{OHP}}$ and requiring the continuity of $d\phi/dz$ there. Numerically solving these self-consistent equations produces a value for ϕ_{OHP}. The Stern model adds only this one additional parameter, z_{OHP}.

We will discuss the following models only qualitatively. As we add more components to the model, additional variables are added that are difficult to measure. But it is important to keep the additional components in mind, if only to appreciate the difficulty of predicting exact quantitative behavior.

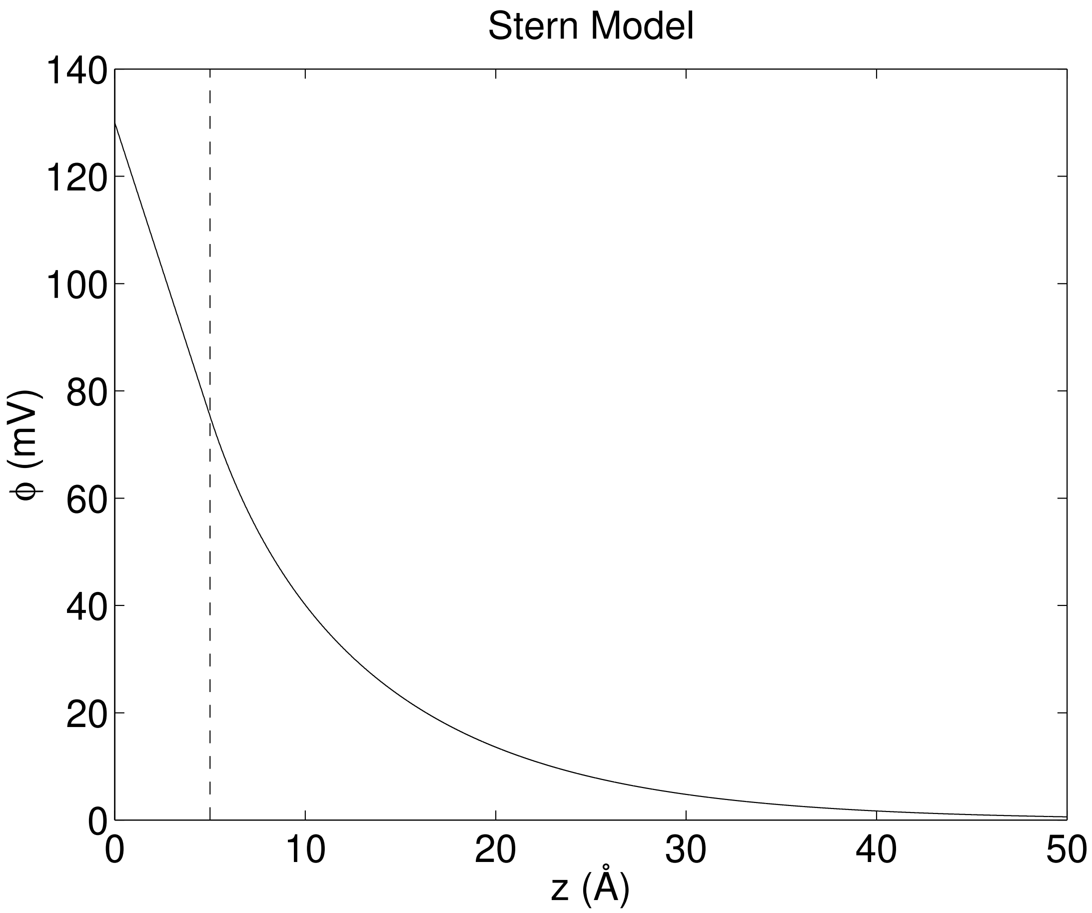

Figure 2.4: Potential profile ϕ vs. z for the Stern model at $\phi_0 = 130$ mV. The transition point is set at $z_{\mathrm{OHP}} = 5$ Å (dashed line), which then corresponds to a transition voltage of $\phi_{\mathrm{OHP}} = 75$ mV. I have used the case of 0.1 M $HClO_4$, as in the experiments described later. Adapted from a similar figure in [20].

The Grahame model [74] (1947) includes the possibility of ions specifically adsorbed (section 2.7) on the electrode surface. This specific adsorption is chemical in nature, and cannot be explained simply by electrostatic arguments. These ions can have either positive, negative, or no charge. We expect, however, that their ionization state and degree of attraction to the electrode will be influenced by the electrode's potential. The closest approach of these adsorbates defines the "Inner Helmholtz Plane".

The Bockris-Devanathan-Müller model includes (polar) solvent molecules that bring us to our complete picture shown earlier 2.1. In retrospect, all of this model-building may seem somewhat *ad hoc*. A contrasting approach has been put forth recently by Borukhov *et al.* [36]. The authors start with the Poisson-Boltzmann equation but include the contributions to the free energy from the finite size of the ions. This remediates some of the defects of the Gouy-Chapman model and is in agreement with experiments they cite where large multivalent ions are adsorbed onto a charged Langmuir monolayer.

2.4 Charged Ions in Solution

Having discussed the electrode surface and its ionic neighborhood, we turn to the charged ions in bulk solution. First, the various modes of transport of charged ions to the electrode surface are discussed and compared. These play an important role in the kinetics of deposition at that interface. Second, the importance of a supporting electrolyte in electrochemical experiments is described.

2.4.1 Transport of Ions

In any deposition/growth system, the transport of particles to the surface is an important consideration. Often, the evolution of the surface morphology is determined by the relative rates of transport to the surface and reactions at the surface. Two familiar limiting cases are diffusion-limited aggregation (DLA) [153, 154] and kinetic-limited growth (such as the KPZ model [86]). All electrochemical reactions take place only at the electrode surface, so transport of ions to that interface is of paramount importance.

We expect the current of species i to be proportional to its respective electrochemical potential gradient,

$$\mathbf{J}_i = -\frac{c_i D_i}{kT} \nabla \widetilde{\mu}_i + c_i \nu \tag{2.30}$$

with the usual diffusion constant D. $\mathbf{J}$ is the flux of ions and has units of concentration times velocity. We consider the possibility that the solution itself is in motion, with velocity ν. If the concentrations are small, the ideal gas approximation can be used (2.6):

$$\widetilde{\mu}_i = \mu_{0,i} + kT \ln c_i + q_i \phi. \tag{2.31}$$

The electrochemical potentials, which are not directly measurable, have been replaced by concentrations and the electrostatic potential energy. Substituting (2.31) into (2.30), we obtain the Nernst-Planck equation

$$\mathbf{J}_i(\mathbf{r}) = -D_i \nabla c_i(\mathbf{r}) - \frac{D_i c_i(\mathbf{r}) q_i}{kT} \nabla \phi(\mathbf{r}) + c_i(\mathbf{r}) \nu(\mathbf{r})\ . \tag{2.32}$$

Using the continuity equation

$$\frac{\partial c}{\partial t} + \nabla \cdot \mathbf{J} = 0 \tag{2.33}$$

we obtain an equation of motion for the concentration profile

$$\frac{\partial c_i(\mathbf{r})}{\partial t} = D_i \nabla^2 c_i(\mathbf{r}) + \frac{D_i c_i(\mathbf{r}) q_i}{kT} \nabla^2 \phi(\mathbf{r}) - \nabla \cdot (c_i(\mathbf{r}) \nu(\mathbf{r})) \,. \tag{2.34}$$

These three terms respectively represent diffusion, electromigration, and convection.

Diffusion refers to the random, Brownian motion of particles that follow Fick's first and second laws of diffusion:

$$\mathbf{J}(\mathbf{r}) = -D \nabla c(\mathbf{r}) \tag{2.35}$$

$$\frac{\partial c(\mathbf{r})}{\partial t} = D \nabla^2 c(\mathbf{r}) \tag{2.36}$$

Fick's first law can be derived by considering the Brownian motion of particles. A simple treatment can be found in [25], which considers a random walk of fixed step size. More sophisticated treatments make use of the Langevin equation [97]. Fick's second law of diffusion (2.36) follows from the first (2.35) by the continuity equation (2.33).

The diffusion constant can be solved for by using a Fourier transform (appendix B)

$$\langle r^2(t) \rangle = 2dDt \tag{2.37}$$

where d is the spatial dimensionality ($d = 3$ for a typical solution vessel, although $d = 1$ is probably more appropriate for the thin-layer cell described in section 4.3.4).

The second mode, electromigration, refers to the motion of charged ions under the influence of a The final mode of ionic transport is due to the transport of the solution itself. Formally, this is termed *hydrodynamic* transport, though it is usually known as convection. Because of the extremely small solution volume in our x-ray cell, hydrodynamic transport is not a consideration. However, it is an important consideration in larger electrochemical cells. When the solution is stirred or the electrode rotated, this will give rise to hydrodynamic effects. Rotating ring-disk techniques [50] make use of this effect, for instance. Convection must also be taken into account for sensitive measurements that take place over several minutes and where significant depletion occurs near the electrode.

2.4.2 Supporting Electrolyte and Charge Screening

In addition to the species of interest, most electrochemical experiments incorporate a *supporting electrolyte*. This is either the solution or is dissolved in the solution at a high concentration with respect to the species of interest. For instance, in our experiments the primary solution was H_2O, and the supporting electrolyte was 0.1M $HClO_4$. A brief and practical discussion of supporting electrolytes can be found in Brett and Brett [40].

There are several advantages to using a supporting electrolyte. First, the double-layer does not extend far into the solution; the majority of the potential drop is very close to the electrode (section 2.3). Second, ions are well-screened. As described by Debye-Hückel theory (see, for example, McQuarrie [98]), a charge in solution tends to attracts charges of opposite sign. The gives rise to an effective "ionic atmosphere" that diminishes the effective net charge felt by a test charge some distance away. Third, because there are far more charged ions in solution, the overall resistance of the solution is much diminished. Fourth, most of the current is carried by the electrolyte, not the dilute ions. This has implications on the dominant mode of transport.

In any electrochemical system, it is important to determine what fraction of the measured current is derived from diffusion as opposed to electromigration. When both effects are present, the analysis becomes complicated. However, electrochemical experiments are generally carried out with a large concentration of a supporting electrolyte relative to the concentrations of active species. The supporting electrolyte does not take part in the reaction at the electrode, but does carry the majority of the current through the solution. The electrolyte serves to screen the ions, making the "ideal gas" approximation more realistic. Hence, the deposited ions arrive mostly via diffusion, and electromigration effects can be neglected [26].

2.5 Bulk Deposition

In this section I will discuss the deposition of "bulk" amounts of material onto an electrode surface. In the next chapter I will turn to "underpotential" deposition, which occurs at voltages closer to the rest potential, and is sometimes the precursor to bulk deposition.

As a prelude to understanding underpotential deposition, it is necessary to understand something about bulk deposition. First I will discuss the Nernst equation, which determines the onset of bulk deposition. Then I will introduce the Cottrell equation, which is a simple realization of bulk deposition. Both of these are covered in the more analytical electrochemistry texts.

2.5.1 Nernst Equation

In discussing chemical activities (section 2.2) and and electrochemical potentials (section 2.2), we have already developed the necessary machinery to write down the Nernst equation. The following treatment parallels Bard and Faulkner [27].

Using the relation between chemical potentials and chemical activities (2.2), the Gibbs free energy is

$$\Delta G = \Delta G_0 + kT \sum_i \nu_i \ln a_i \tag{2.38}$$

In an electrochemical reaction, the change in Gibbs free energy is equal in magnitude to the electrical energy dissipated or produced. Conventionally, the sign of the voltage difference ΔV is taken to be $\Delta V > 0$ when the reaction is spontaneous ($\Delta G < 0$). Then

$$\Delta G = -ne\Delta V \tag{2.39}$$

The "standard" (when all activities are unity) potential of the reaction ΔV_0 is just $\Delta G_0 = -neV_0$. Then,

$$\Delta V = \Delta V_0 - \frac{kT}{ne} \sum_i \nu_i \ln a_i \tag{2.40}$$

This equation, known as the *Nernst equation* is of great importance to electrochemistry. Knowing the stoichiometry of a reaction ν_i and the activities a_i, one can predict the electric potential necessary to drive the reaction forward (or spontaneously generated). The voltage ΔV is often termed the *Nernst potential.* In electrochemistry textbooks, ΔV is often written as E, and ΔV_0 as E^0. I am using my notation to emphasize that this voltage is the potential difference across the electrodes, and to avoid confusion with the electric field.

It is also common to write the Nernst equation in terms of concentrations, which are easily measured. (The activities are often not known.) Using activity coefficients (2.5) $a_i = \gamma_i c_i$,

$$\Delta V = \Delta V_0 - \frac{kT}{ne} \sum_i \nu_i \ln \gamma_i c_i \tag{2.41}$$

$$= \Delta V_0' - \frac{kT}{ne} \sum_i \nu_i \ln c_i \tag{2.42}$$

where the *formal potential* $\Delta V_0'$ incorporates the activity coefficients. The formal potentials for various reactions can be easily measured and are tabulated in the literature.

Bulk deposition is just an example of these reversible reactions we have been discussing. Consider the deposition of copper ions from solution onto an inert electrode. This is written as

$$\mathrm{Cu}^0(\mathrm{ads}) \longleftrightarrow \mathrm{Cu}^{2+}(\mathrm{sol}) + 2e^- \tag{2.43}$$

For bulk deposition, we must have $\Delta V < 0$ for this reaction (as written). For potentials above the Nernst potential, we expect to see no deposition. As the potential of the working electrode is lowered below the Nernst potential, deposition is possible. The more negative the applied potential, the more favored the reaction becomes, and the faster it goes. Measuring the deposition by the current flow, we find a response as in figure 2.5.

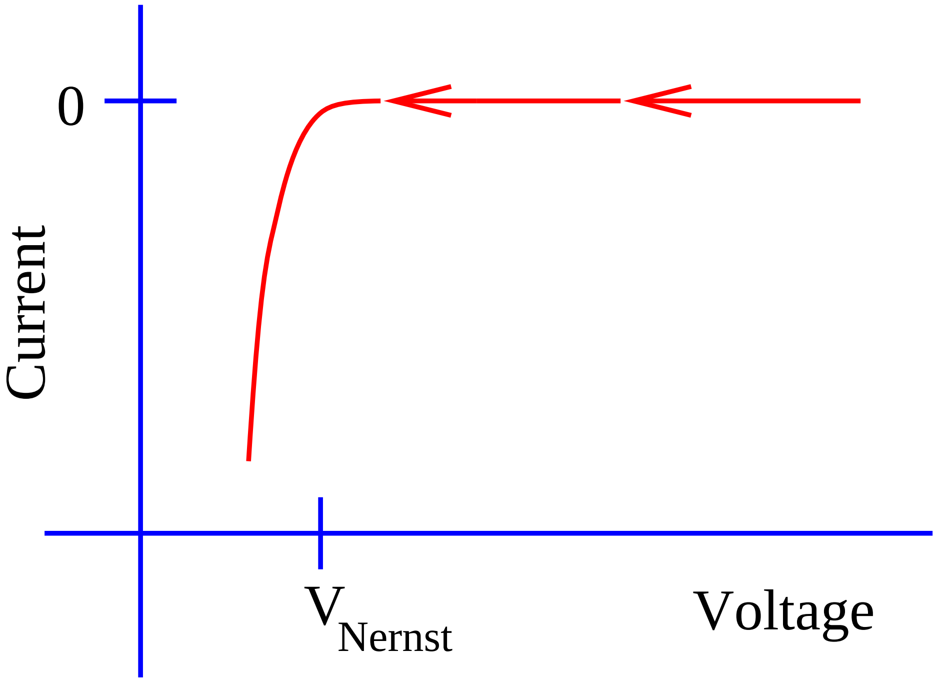

Figure 2.5: Cartoon of Bulk Deposition

2.5.2 Cottrell Equation

Consider a deposition experiment where the potential is abruptly shifted from above the Nernst potential (no deposition) to below the Nernst (bulk deposition). Before $t = 0$, the system is in equilibrium with a mean concentration of c_∞ everywhere; $c(z, t \leq 0) = c_\infty$. At $t = 0$, the voltage is altered such that deposition occurs. The electrode surface is assumed to be perfectly adsorbing so that it is a perfect sink for the adsorbing ions; $c(z = 0^+, t > 0) = 0$. Each of these adsorbed ions transfers n electrons to/from the electrode. Furthermore; the solution container is semi-infinite and hence inexhaustible. Far from the electrode, the bulk solution concentration will be maintained; $c(z \to \infty, t) = c_\infty$. We must solve the linear diffusion equation

$$\frac{\partial c(z,t)}{\partial t} = D\frac{\partial^2 c(z,t)}{\partial z^2} \tag{2.44}$$

subject to the initial condition $c(z, t \leq 0) = c_\infty$ and the boundary conditions

$$\begin{aligned} c(z = 0^+, t > 0) &= 0 && (2.45) \\ c(z \to \infty, t) &= c_\infty && (2.46) \end{aligned}$$

The standard method [28, 41] is to Laplace transform (2.44) and the initial condition:

$$s\, c(z,s) - c_\infty = D\frac{d^2 c(z,s)}{dz^2} \tag{2.47}$$

This ordinary differential equation has the solution

$$c(z,s) = A(s)\exp\left[(s/D)^{1/2}z\right] + B(s)\exp\left[-(s/D)^{1/2}z\right] + c_\infty/s \tag{2.48}$$

Applying (2.46) requires $A(s) = 0$ and (2.45) then requires $B(s) = -c_\infty/s$. The solution to the transformed equation is

$$c(z,s) = \frac{c_\infty}{s}\left\{1 - \exp\left[-(s/D)^{1/2}z\right]\right\} \tag{2.49}$$

Taking the inverse Laplace transform yields the concentration profile

$$c(z,t) = c_\infty\left\{1 - \mathrm{erfc}\left[\frac{z}{2(Dt)^{1/2}}\right]\right\} = c_\infty \mathrm{erf}\left[\frac{z}{2(Dt)^{1/2}}\right] \tag{2.50}$$

Using the continuity equation (2.33) and assuming each ion transfers a charge of ne, then the current density $j(t)$ measured at the electrode (normalized to electrode area) is

$$j(t) = \lim_{z\to 0} = neD\frac{\partial c(z,t)}{\partial z} \tag{2.51}$$

The derivative $\partial c/\partial z$ can be evaluated by applying the Fundamental Theorem of calculus to the definition of the error function,

$$\mathrm{erf}(x) = \frac{2}{\sqrt{\pi}}\int_0^x dy\ y^2 \tag{2.52}$$

and then substituting back into (2.51) to arrive at

$$j(t) = nec_\infty\left(\frac{D}{\pi t}\right)^{1/2} \tag{2.53}$$

The concentration profile and current density are plotted in figure 2.6 for $D = 9 \times 10^{-6}\mathrm{cm}^2/\mathrm{s}$, typical of aqueous solutions. Note that the current is arbitrarily large at early times (limited by extrinsic factors), and decays away as a power-law. The concentration profile begins as a steep distribution, but broadens at later times as diffusion makes more ions available.

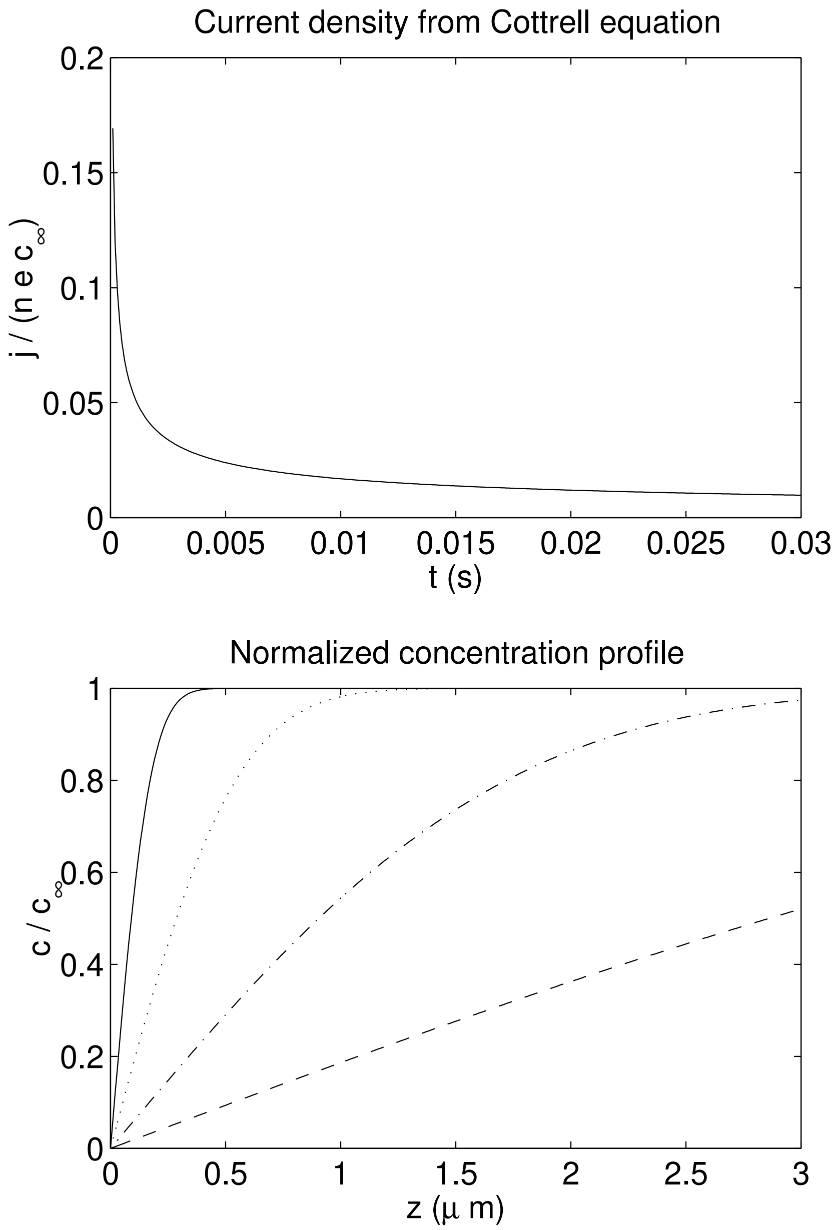

Figure 2.6: (a) Current density at the electrode surface from (2.53). (b) Concentration profiles from (2.53), for $t = 0.001$s (solid), 0.01s (dotted), 0.1s (dot-dashed), and 1s (dashed).

2.6 Underpotential Deposition

Imagine that we start at the rest potential and slowly sweep the potential in a negative direction. In contrast to the cartoon of bulk deposition (figure 2.5), small peaks in the current response can be observed. This phenomenon is not ubiquitous. These peaks are only observed for particular species deposited onto particular electrodes. In addition, this phenomena is very surface-sensitive. For instance, the peak positions and heights when Cu is deposited onto Pt vary depending upon the particular Pt crystal face: (111), (100), or (110). This process is termed *underpotential deposition*, because the deposition takes place at potentials "under" the Nernst potential (closer to the rest potential). A potential applied beyond the Nernst potential is often termed the *overpotential*, as in (6.2).

Although underpotential deposition (UPD) is a complex process, we can qualitatively justify this behavior. Presuming that a Cu ion has a greater affinity to bond to a Pt atom than it does to another Cu atom, then we can imagine that the underpotential deposition situation shown in the top panel of figure 2.8 would be favored at some potentials for which bulk deposition, shown in the bottom panel, would not. In the top panel, each deposited Cu is directly in contact with the Pt surface. In the bottom panel, the subsequent Cu layers are only in contact with the prior Cu layers.

In the next section, I present simple models of "specific adsorption", of which underpotential deposition is a particular example.

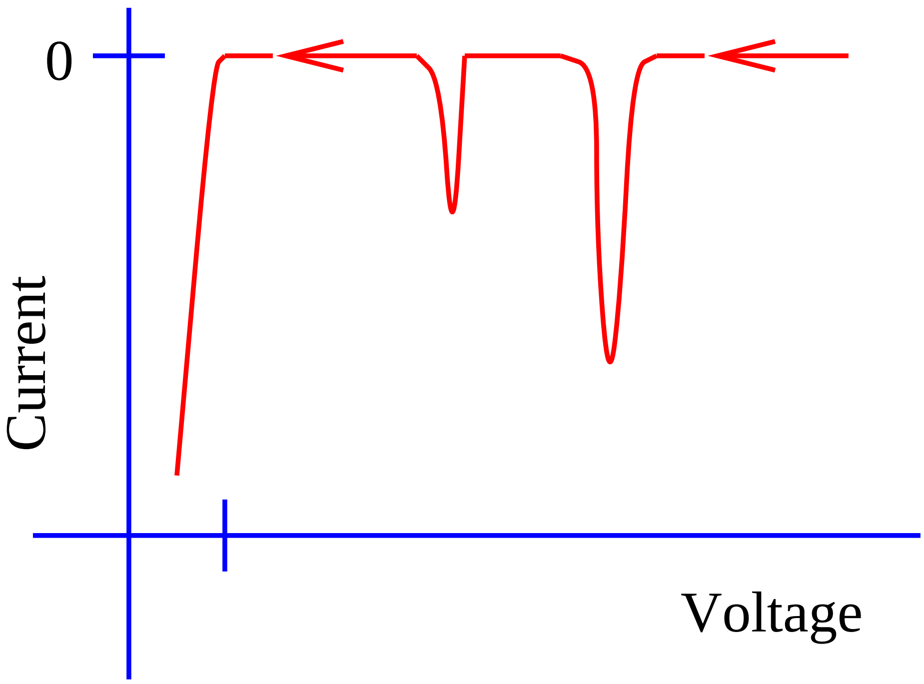

Figure 2.7: Indication of underpotential deposition during a voltage sweep.

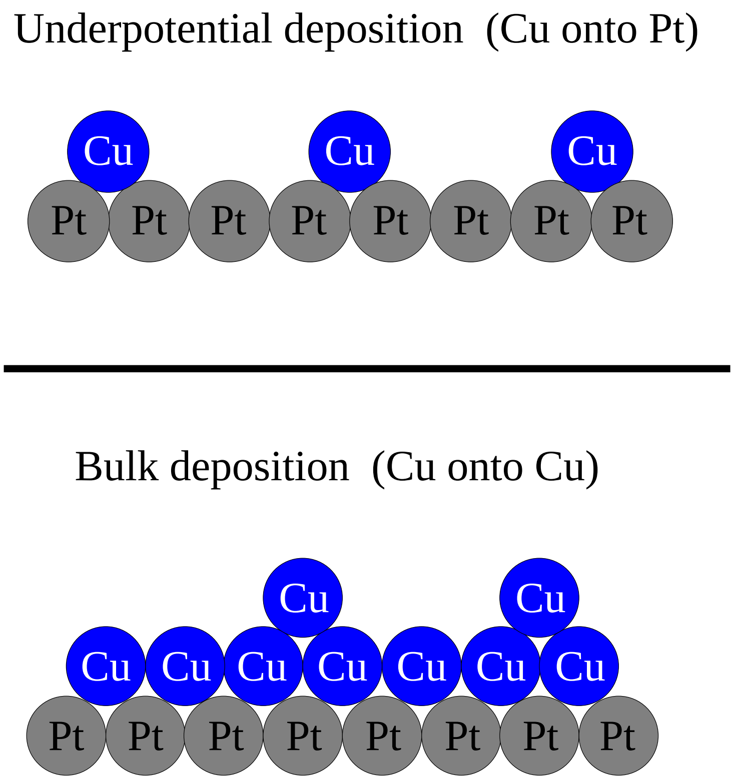

Figure 2.8: Difference between bulk deposition and underpotential deposition

2.7 Specific Adsorption

In the discussion of the double layer (section 2.3) we considered the electrostatic interaction of charged ion species with the charged electrode. In our most sophisticated model, we assumed that no ion could approach closer than the radius of its solvation sphere. Ions that do lose their solvation spheres and penetrate within the outer Helmholtz plane are said to be specifically adsorbed. Their interaction is more than electrostatic, and is comparable to a chemical bond. Bard and Faulkner [29] make the analogy:

> The difference between nonspecific and specific adsorption is analogous to the difference between the presence of an ion in the ions atmosphere of another oppositely charged ion in solution (e.g., as modeled by the Debye-Hückel theory) and the formation of a bond between the two solution species (as in a complexation reaction).

Needless to say, these interactions will be very complex. Models of these processes need to combine the ionization of charges near surfaces, solvation, chemical bonding, charge-screening, and surface phenomena such as work functions.

2.8 Adsorption Isotherms

Even in the absence of any adsorption, there would be some concentration (equal to the bulk concentration) of ions of species i in a region near the electrode surface. The surface excess concentration Γ_i [116, 30] is defined to be the concentration of species i in excess of the bulk concentration, normalized by the area of the electrode. The "coverage" θ is defined to be the surface excess normalized by its saturation value, $\theta = \Gamma/\Gamma_{\text{sat}}$, so that $0 < \theta < 1$. The definition of this region "near" the electrode surface is somewhat arbitrary. In principle, it can include the diffuse double-layer. However, the Γ_i in the diffuse double layer will have little effect if we have a supporting electrolyte. First, most of the the ions drawn into the diffuse double layer will be from the supporting electrolyte, not the species i. Second, the width of the diffuse double-layer narrows exponentially as the concentration of ions increases.

In the limit that the adsorbates on the surface to do not interact, we can write down a simple model for the adsorption onto a surface. This is very similar to standard the simplest lattice-gas models of adsorption discussed in introductory statistical mechanics courses. I also assume that there is no interaction between the species and the solution itself, and that there is no species-species interaction in the solution. If concentrations are not too high, then the supporting electrolyte screens these charges.

The rate of adsorption is proportional to the concentration of ions in solution c, the number of sites available for adsorption $(1-\theta)$, and a Boltzmann factor involving the Gibbs free energy of the activated complex G' (see figure 2.9) and the Gibbs free energy of the ion in solution G_{sol}. Isotherms, by definition, are equilibrium measurements. Hence we usually assume that the system has come to equilibrium such that the concentration near the electrode is equal to that in the bulk solution, c_∞. We are also implicitly neglecting the diffuse double layer (which is described by the Poisson-Boltzmann distribution).

$$\text{adsorption:} \quad \frac{d\theta}{dt} = Kc(1-\theta)\exp\left(-\frac{G' - G_{\text{sol}}}{kT}\right) \,. \tag{2.54}$$

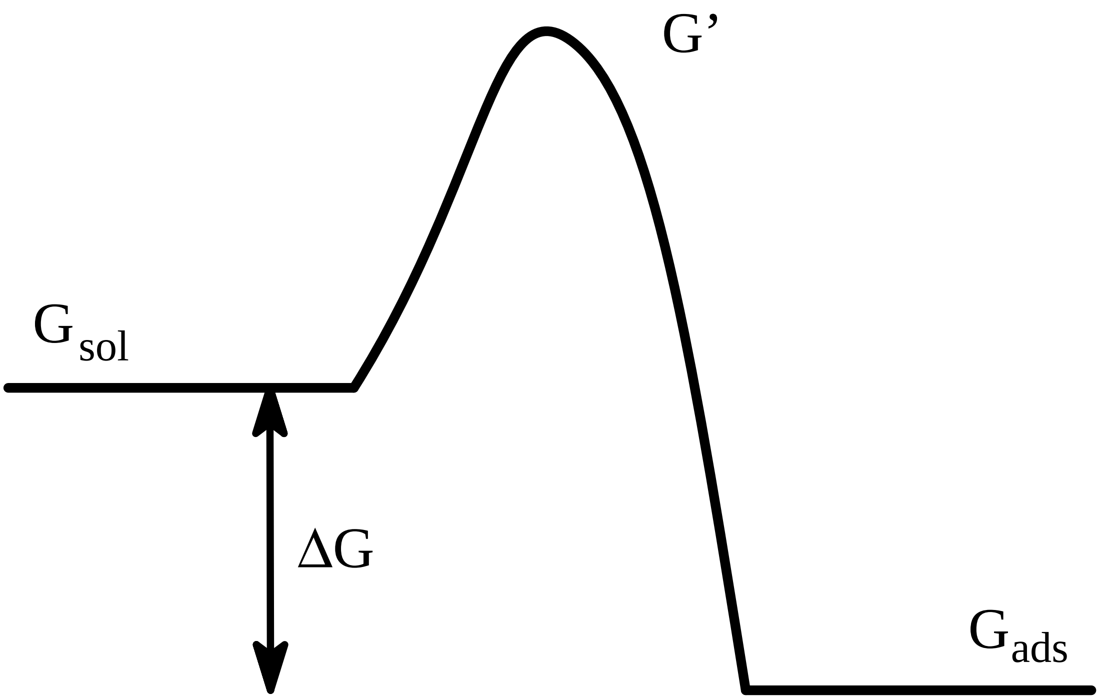

Figure 2.9: Diagram of energy levels for adsorption process. In this case, adsorption is energetically favored by an amount ΔG, but the system must first overcome an energy barrier G'.

Similarly, the rate of desorption is proportional to the concentration on the surface θ and another Boltzmann factor involving G' and the Gibbs free energy of the adsorbed ion G_{ad}.

$$\text{desorption:} \quad \frac{d\theta}{dt} = -K\theta\exp\left(-\frac{G' - G_{\text{ad}}}{kT}\right) \,. \tag{2.55}$$

In equilibrium, these θ are constant, and these two rates are equal in magnitude. Then,

$$\frac{\theta}{1-\theta} = c\exp\left(-\frac{\Delta G_0}{kT}\right) \tag{2.56}$$

where $\Delta G_0 = G_{\text{sol}} - G_{\text{ad}}$. This describes the *Langmuir* isotherm.

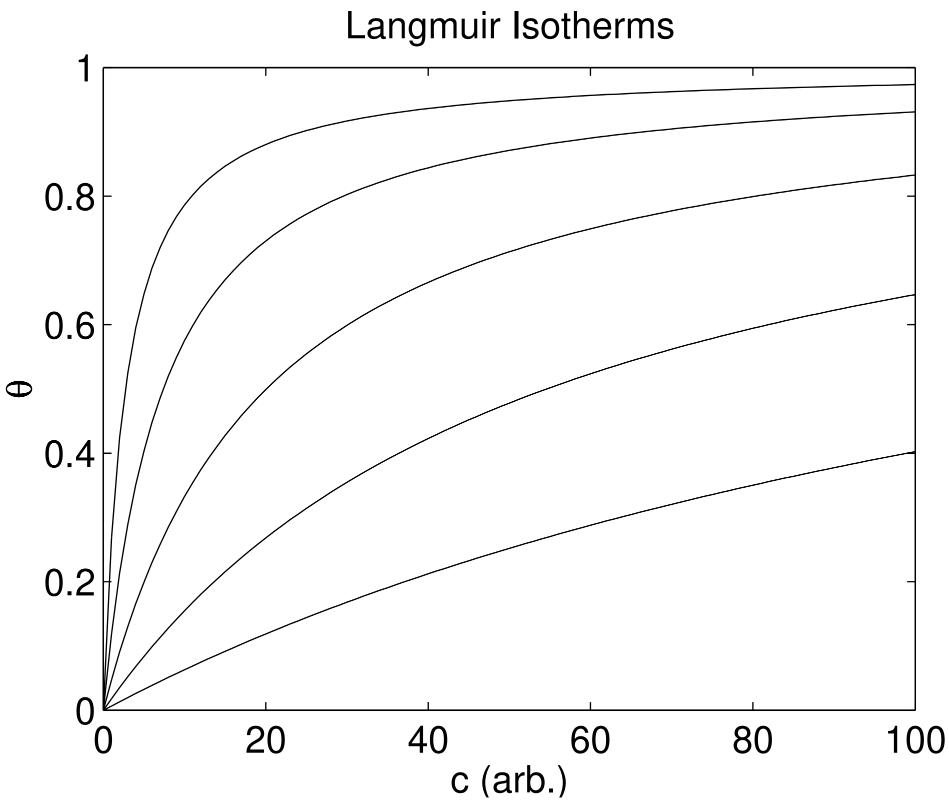

Figure 2.10: Langmuir isotherms for various values of $\Delta G_0/kT$.

To make a slightly more realistic model, we assume that there is some interaction between the adsorbates. Using a mean-field approach, let $\Delta G = \Delta G_0 + \gamma\theta$. If the adsorbates attract one another, then $\gamma > 0$. If they repel, then $\gamma < 0$. In the case that $\gamma = 0$, we recover the Langmuir result. Typically this isotherm is written as

$$\frac{\theta}{1-\theta} = c \exp\left(-\frac{\Delta G_0}{kT}\right) \exp(-g\theta) \tag{2.57}$$

where $g = \gamma/kT$. This is known as the *Frumkin* isotherm. (Note that I am defining g as following Schmickler [117], other sources [42, 24] define $2g = \gamma$. My g is equal to g' of Bard and Faulkner [24].) Also frequently used is the *Temkin* isotherm, which is just (2.57) in the $\theta \to 1/2$ limit and is often rearranged like

$$\theta = \frac{1}{g} \ln\left[c \exp\left(-\frac{\Delta G_0}{kT}\right)\right] . \tag{2.58}$$

The choice of which isotherm to use depends upon experimental conditions. The Langmuir isotherm is an accurate description for small coverages (θ), or equivalently, small concentrations. In this regime the adsorbates are sufficiently sparse that they do not interact. Because of the approximation used to derive it, the Temkin isotherm is only used for $0.2 < \theta < 0.8$ and g not approaching zero. The Langmuir and Frumkin isotherms are virtually indistinguishable as $\theta \to 0$, and both are linear in that regime. These two points become apparent upon expanding (2.57) in this limit and keeping terms to second order,

$$\theta + (1+g)\theta^2 \approx c \exp\left(-\frac{\Delta G_0}{kT}\right) . \tag{2.59}$$

They are also evident from inspection of figure 2.11. Often, only the terms linear in θ is kept, and the resulting equation is called the “linearized (Langmuir) isotherm”.

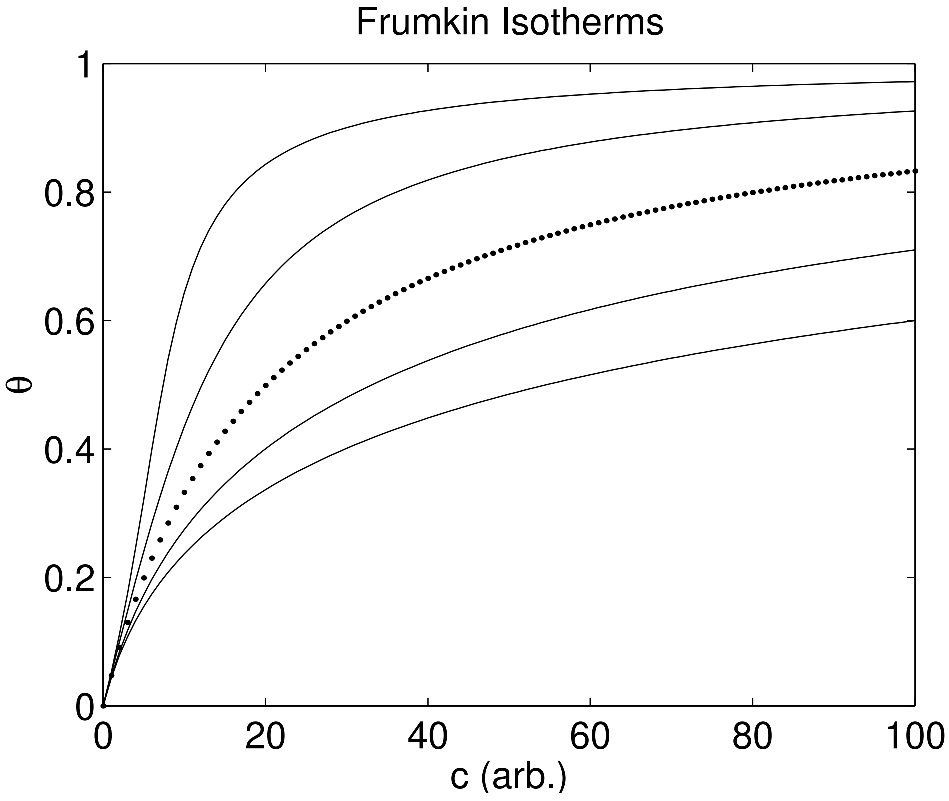

Figure 2.11: Frumkin isotherms for various values of g. The dotted line corresponds to $g = 0$, which is identical to the Langmuir isotherm.

Chapter 3

Introduction to X-ray Scattering

3.1 Introduction

This chapter provides an introduction to x-ray scattering, suitable for a first-year graduate student studying physics, chemistry, or a related field. It covers a broader range of material than is necessary simply to interpret the results in chapters 5 and 6. The reader may safely decide to skip ahead and return back to the specific sections that are referenced in those chapters.

3.2 Generation of X Rays

Early x-ray experiments were performed with x-ray tubes, and today most still are. Presently there are at least two other available sources, both superior to tubes. *Rotating anode* sources, while expensive, can easily fit within a room. *Synchrotron sources* are extremely large multi-user facilities, of which only a handful exist in the world. The benefits include an enormous gain in flux and angular collimation. Both of these sources were used for this dissertation, and I will discuss them in turn.

3.3 Conventional X-ray Sources

"Conventional" x-ray sources [57] work on the same principle as Röntgen's original apparatus; electrons are accelerated into an block of material (the anode), generating x-rays. While the x-ray tube of Röntgen used electrons ionized from gas, today the electrons are produced by a high-current filament. These electrons are then accelerated by an electric field into the anode. When struck by the electrons, the anode produces a broad, continuous spectrum of x-rays, due to the electron deceleration within the anode. This is typically called *bremsstrahlung* from the German "braking radiation".

The more useful spectral components are the "characteristic" radiation lines, which arise from electronic transitions within the anodic atoms. If an electron kicks out an electron from an atom, the atom will be in an excited, ionized state. Subsequently, one of the remaining atomic electrons will fall into the unoccupied state, releasing an x-ray photon and conserving energy. Due to the quantized energy levels, the resultant x-ray spectrum is also discrete, and characteristic of the atomic element. The wavelengths are labeled according to the energy transition. For instance, the $K\alpha$ lines correspond to transitions from L $(n = 2)$ to K $(n = 1)$, the $K\beta$ from M $(n = 3)$ to K, and $L\alpha$ from M to L. The principal quantum number here is denoted by n. These characteristic lines can be exceedingly narrow

(< 0.001 Å), so it is possible to have nearly monochromatic radiation for an x-ray experiment. Sometimes it is even possible to resolve the lines even further. The $K\alpha$, for instance, can split into the $K\alpha_1$ and $K\alpha_2$. These correspond to transitions from L states with slightly different energies (the fine structure).

The intensity (per $d\lambda$) in the characteristic lines is higher than the *bremsstrahlung* by a few orders of magnitude. Nevertheless, the flux per solid angle is low because the radiation is spread isotropically into all directions. The overall intensity can be boosted by using the highest electron beam current possible. In practice, this requires both water-cooling the anode and rotating it to prevent a single focus spot from overheating. These *rotating anodes* provide the highest flux presently available in a "bench top" laboratory setting.

For the work presented in this dissertation, a Rigaku (Model RU200) rotating anode was used primarily for orientation of samples, training, and as a testing bed for the experiments. This instrument has a tungsten filament that can support up to 200 mA current. The electrons are accelerated over potentials as large as 60 kV into a rotating, water-cooled copper anode.

3.4 Synchrotron X-ray Sources

A synchrotron x-ray source begins with an ultra-high vacuum (10^{-9} Torr) storage ring. Within the ring are electrons circulating at near-light speeds. Whenever a charge is accelerated (for instance, if constrained to a circular path) it emits radiation. In doing so, it loses energy. To keep the electrons moving in stable orbits, energy in the radio frequency range is added at intervals synchronized with the electron "bunches". While electromagnetic radiation is produced for any acceleration, it is advantageous to place additional accelerating devices at specific locations. In our experiments, these were simple "bending magnets" that sharply steer the electron beam. More sophisticated devices, such as "wigglers" and "undulators" cause the electron beam to be accelerated up and down several times within a narrow spatial region. This leads to a corresponding increase in the intensity of the overall x-ray beam delivered.

A brief, if dated (1979), review of synchrotron radiation can be found in [56]. An even shorter overview is presented in [87]. A thorough and very recent (not yet in print) account of synchrotron radiation and related devices is [77]. The remainder of this section will use a few results derived in [130].

The most striking feature of synchrotron sources is the high degree of collimation (unlike conventional sources, which radiate into all 4π solid angle). The "opening angle" for the radiation is peaked sharply forward and determined by the speed of the electrons. The full-width at half-maximum is [130]

$$\theta_{\mathrm{FWHM}} \approx 1/\gamma \,, \tag{3.1}$$

where

$$\gamma = \frac{1}{\sqrt{1 - v^2/c^2}} \tag{3.2}$$

is the usual relativistic Lorentz factor [81]. For a 2 GeV beam of electrons (whose rest mass is 511 eV), $\gamma \approx 4000$, leading to an opening angle of $\theta_{\mathrm{FWHM}} = 0.015°$. For a comparable energy resolution, synchrotrons deliver 10^6 – 10^7 times the flux of rotating anodes.

A second feature is that synchrotron radiation has different polarization characteristics from the unpolarized conventional sources. The ratio of power in the parallel polarization (in the plane of the synchrotron ring) to that in the perpendicular polarization is

$$\frac{P_{\parallel}}{P_{\perp}} = \frac{6 + (v/c)^2}{2 - (v/c)^2} \tag{3.3}$$

where v is the electronic speed. For a highly relativistic beam, the electric field is mostly (by a factor of seven) polarized in the plane of the electrons' motion.

The third feature is that synchrotron x-ray radiation has a broad, continuous energy spectrum. The upper value is limited by the electronic velocity, but the range is also dependent upon the characteristics of the beamline acceleration device and "optics" within the beamline itself. Some experiments make use of the entire multifrequency ("white") beam. The majority (including the ones described herein) use a monochromator to select a comparatively narrow range of frequencies. A typical monochromator consists of one or more Bragg diffractions (3.67) from single crystals or specially engineered multilayer structures.

3.5 Single-Electron Scattering

Although x-ray scattering is inherently a quantum phenomenon, many important features can be correctly derived from a classical treatment [141]. A quantum mechanical treatment can be found in [46, 112]. We will also take the nonrelativistic limit and use Gaussian units.

Following the general treatment in [82] assume a "free" charge of magnitude q and mass m. This is subject to an incident electromagnetic plane wave of frequency ω, wavevector $\mathbf{k}_1 = k\mathbf{n}_1$, electric field amplitude E_1, and polarization $\boldsymbol{\epsilon}_1$

$$\mathbf{E}_1(t) = E_1 \boldsymbol{\epsilon}_1 e^{i(\mathbf{k}_1 \cdot \mathbf{x} - \omega t)} \tag{3.4}$$

$$\mathbf{B}_1(t) = \mathbf{n}_1 \times \mathbf{E}_1 \tag{3.5}$$

As usual for electromagnetic radiation, $\mathbf{E}_1$, $\mathbf{B}_1$, and $\mathbf{n}_1$ are mutually orthogonal.

By the Lorentz force law and Newton's second law, a free point charge q will then accelerate as

$$\mathbf{a}(t) = \frac{q}{m} \mathbf{E}_1 e^{i(\mathbf{k}_1 \cdot \mathbf{x} - \omega t)}. \tag{3.6}$$

We know that accelerating charges emit radiation. Following (14.18) from [83], the radiation field observed from a distance $\mathbf{R}$ along a unit vector $\mathbf{n}_2$ is

$$\begin{aligned} \mathbf{E}_2(t) &= \frac{q}{c^2} \left[\frac{\mathbf{n}_2 \times (\mathbf{n}_2 \times \mathbf{a})}{R} \right]_{\mathrm{ret}} && (3.7) \\ \mathbf{B}_2(t) &= \left[\mathbf{n}_2 \times \mathbf{E}_2 \right]_{\mathrm{ret}} && (3.8) \end{aligned}$$

so the radiation will be an electromagnetic spherical wave, of the same frequency. The "ret" refers to the fact that the quantities within the square brackets must be calculated at "retarded" time $t' = t - R/c$. Writing the electric field more definitely,

$$\mathbf{E}_2(t) = \frac{q^2}{mc^2} \frac{E_1}{R} \, e^{i(\mathbf{k}_2 \cdot \mathbf{x} - \omega t)} \, \mathbf{n}_2 \times (\mathbf{n}_2 \times \boldsymbol{\epsilon}_1) \, . \tag{3.9}$$

The instantaneous energy flux is described by the Poynting vector,

$$\mathbf{S} = \frac{c}{4\pi} \mathbf{E}_2 \times \mathbf{B}_2 = \frac{c}{4\pi} |\mathbf{E}_2|^2 \mathbf{n}_2. \tag{3.10}$$

and the power radiated per solid angle is (3.10) multiplied by R^2:

$$\frac{dP}{d\Omega} = \frac{c}{4\pi} R^2 |\mathbf{E}_2|^2 \ . \tag{3.11}$$

If we define intensity as the average power per solid angle and recall that the time-average of a sinusoidally varying function over a period is $\langle \sin \omega t \rangle = \frac{1}{2}$, then

$$I = \left\langle \frac{dP}{d\Omega} \right\rangle = \frac{c}{8\pi} R^2 |E_2|^2 \ . \tag{3.12}$$

Now think of this as a *scattering process*, and so define a scattering cross-section. For the usual particle-scattering situation, this is

$$\frac{d\sigma}{d\Omega} = \frac{\text{number of particles scattered into a unit solid angle per unit time}}{\text{number of incident particles crossing unit area per unit time}} \ . \tag{3.13}$$

In analogy to this, we can define the relevant cross-section as

$$\frac{d\sigma}{d\Omega} = \frac{\text{energy radiated into a unit solid angle per unit time}}{\text{incident energy per unit area per unit time}} \ . \tag{3.14}$$

The denominator in (3.14) is the time-averaged incident energy flux $(c/8\pi)|E_1|^2$, so

$$\frac{d\sigma}{d\Omega} = R^2 \left| \frac{E_2}{E_1} \right|^2 = \left(\frac{q^2}{mc^2} \right)^2 \mathcal{P}(\boldsymbol{\epsilon}_1, \mathbf{n}_2) \tag{3.15}$$

where

$$\mathcal{P}(\boldsymbol{\epsilon}_1, \mathbf{n}_2) = |\mathbf{n}_2 \times (\mathbf{n}_2 \times \boldsymbol{\epsilon}_1)|^2 \tag{3.16}$$

is a factor dependent upon the incoming polarization and the observation point. Using the vector relation

$$\mathbf{a} \times (\mathbf{b} \times \mathbf{c}) = (\mathbf{a} \cdot \mathbf{c})\mathbf{b} - (\mathbf{a} \cdot \mathbf{b})\mathbf{c} \ , \tag{3.17}$$

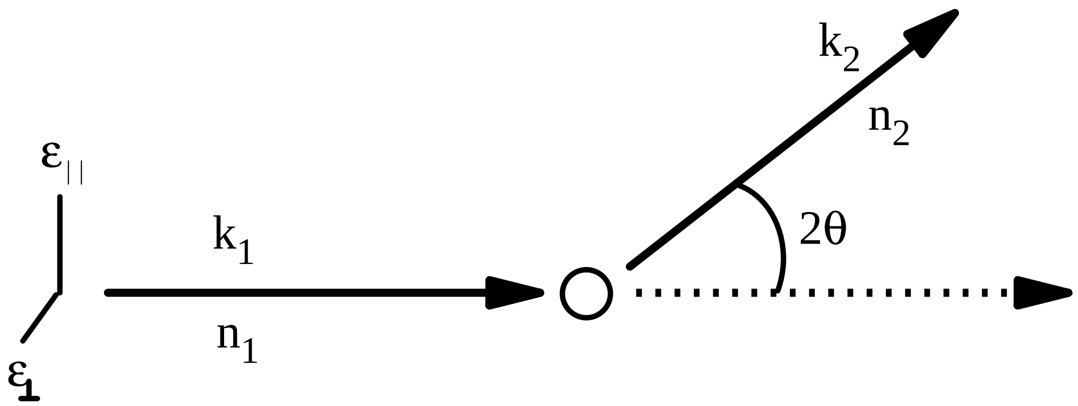

Figure 3.1: Diagram for classical x-ray scattering

we have

$$\mathcal{P}(\boldsymbol{\epsilon}_1, \mathbf{n}_2) = \left|\mathbf{n}_2 \times (\mathbf{n}_2 \times \boldsymbol{\epsilon}_1)\right|^2 = \left|(\mathbf{n}_2 \cdot \boldsymbol{\epsilon}_1)\mathbf{n}_2 - (\mathbf{n}_2 \cdot \mathbf{n}_2)\boldsymbol{\epsilon}_1\right|^2 \ . \tag{3.18}$$

Take $\mathbf{n}_1$ and $\mathbf{n}_2$ to define the "scattering plane", and define the angle 2θ to lie between them:

$$\mathbf{n}_1 \cdot \mathbf{n}_2 = \cos 2\theta \ . \tag{3.19}$$

The initial polarization $\boldsymbol{\epsilon}_1$ is orthogonal to $\mathbf{n}_1$; separate it into components $\boldsymbol{\epsilon}_{\|}$ and $\boldsymbol{\epsilon}_{\perp}$ that lie parallel and perpendicular to the scattering plane. Noting that $\mathbf{n}_2 \cdot \boldsymbol{\epsilon}_1 = a_{\|} \sin(2\theta)$ for an incoming plane wave polarization $\boldsymbol{\epsilon}_1 = a_{\|}\boldsymbol{\epsilon}_{\|} + a_{\perp}\boldsymbol{\epsilon}_{\perp}$, we have

$$\mathcal{P}(2\theta) = 1 - a_{\|}^2 \sin^2(2\theta). \tag{3.20}$$

For an incoming wave with the electric field polarized perpendicularly to the scattering plane ($a_{\|} = 0$), this polarization factor is unity. This case is applicable (3.3) to synchrotron radiation (section 3.4), where the scattering plane is usually perpendicular to the synchrotron ring. This takes advantage of the high resolution along that direction, determined by the opening angle (3.1). For a parallel polarization ($a_{||} = 1$), this factor becomes $\cos^2(2\theta)$. Conventional sources (section 3.3), such as rotating anodes, produce randomly polarized radiation that has the factor $\frac{1}{2}(1 + \cos^2(2\theta))$.

The intensity of scattered peaks also is proportional to $\sin(2\theta)$. This factor is a consequence of the Jacobian between angle space and reciprocal space; a volume element in reciprocal space is smaller than its generating volume in angle space by a factor $\sin(2\theta)$. These polarization factors $\mathcal{P}(2\theta)$ are sometimes bundled into the "Lorentz-polarization" factor, which is just $\mathcal{P}(2\theta)/\sin(2\theta)$.

3.6 Scattering from Multiple Objects

In this section, I will discuss scattering from multiple objects. By considering the phase difference between scattered waves from spatially separated objects, I introduce the structure factor. Then I discuss the connection between the structure factor and the correlation function.

3.6.1 Fourier Transforms

I assume the reader is familiar with the use of Fourier transforms. This section merely defines the Fourier transform as I will use it, as there is some variety in the normalization and sign conventions in the literature.

Throughout this dissertation, the Fourier transform of a function $f(\mathbf{r})$ in d dimensions is defined to be

$$f(\mathbf{q}) = \int d\mathbf{r}\ e^{-i\mathbf{q}\cdot\mathbf{r}} f(\mathbf{r}) \ , \tag{3.21}$$

and the corresponding inverse Fourier transform to be

$$f(\mathbf{r}) = \left(\frac{1}{2\pi}\right)^d \int d\mathbf{q}\ e^{+i\mathbf{q}\cdot\mathbf{r}} f(\mathbf{q}) \ . \tag{3.22}$$

Without explicit limits, the integration should be read as taking place over all space. Some authors place a $1/(2\pi)^{d/2}$ normalization on each transform, and my choice of assigning the $e^{-i\mathbf{q}\cdot\mathbf{r}}$ to the direct Fourier transform (as opposed to $e^{+i\mathbf{q}\cdot\mathbf{r}}$) is arbitrary. This is the common choice in x-ray scattering texts. In quantum mechanics and solid-state texts, the opposite sign convention is more common. From the definition of a plane-wave

$$\psi(\mathbf{q}, t) = A_{\mathbf{q}} e^{-i(\mathbf{q}\cdot\mathbf{r} - \omega t)} \tag{3.23}$$

I will likewise define the Fourier transform in the time domain to be

$$f(\omega) = \int_{-\infty}^{+\infty} dt\ e^{+i\omega t} f(t) \tag{3.24}$$

and the inverse Fourier transform to be

$$f(t) = \frac{1}{2\pi} \int_{-\infty}^{+\infty} d\omega\ e^{-i\omega t} f(\omega) \ . \tag{3.25}$$

3.6.2 Structure Factors

Take the cross section derived in (3.15) and let the charge q equal the charge of an electron, $-e$. Defining the classical electron radius, $r_0 = e^2/mc^2 = 2.818 \times 10^{-5}$ Å, we have

$$\frac{d\sigma}{d\Omega} = r_0^2 \mathcal{P}(2\theta) \ . \tag{3.26}$$

We see that electrons scatter x-rays only weakly (the cross section is very small). Were it not for the large number of electrons in a macroscopic sample, and the constructive interference under specific conditions, there would be little observable signal. The lack of multiple scattering simplifies x-ray analysis, in contrast to some electron-diffraction probes.

If we have a collection of N identical scatterers at various positions $\mathbf{r}_i$, then the phase factors in the electric field amplitudes (3.4) and (3.9) become important. The ratio $\mathbf{E}_2/\mathbf{E}_1$ contains the phase factor $e^{i(\mathbf{k}_2-\mathbf{k}_1)\cdot\mathbf{r}}$. For the collection,

$$\frac{d\sigma}{d\Omega} = r_0^2 \mathcal{P}(2\theta) \left| \sum_i e^{i(\mathbf{k}_2-\mathbf{k}_1)\cdot\mathbf{r}_i} \right|^2 . \tag{3.27}$$

The differential cross-section $d\sigma/d\Omega$ has units of area, as all cross sections do. The cross section, and hence the intensity, scales with N^2.

The square of the sum of the phase factors is called the *structure factor*, and is defined as

$$S(\mathbf{k}_2 - \mathbf{k}_1) = \frac{1}{N} \left| \sum_i e^{i(\mathbf{k}_2-\mathbf{k}_1)\cdot\mathbf{r}_i} \right|^2 = \frac{1}{N} \sum_i \sum_{i'} e^{i(\mathbf{k}_2-\mathbf{k}_1)\cdot(\mathbf{r}_i - \mathbf{r}'_i)} . \tag{3.28}$$

It is common to define the "momentum transfer" $\mathbf{q} = \mathbf{k}_2 - \mathbf{k}_1$, in regards to the momentum that is transferred to the scattered charge. Keep in mind that $\mathbf{q}$ has dimensions of inverse length (true momentum would require a factor of $\hbar$). For elastic scattering, the wavevector of the incident and scattered waves have an identical magnitude $k = \frac{2\pi}{\lambda}$. From the simple vector addition in figure 3.2,

$$q = 2k \sin\theta . \tag{3.29}$$

So we acquire the most common definition of the momentum transfer vector

$$q = \frac{4\pi}{\lambda} \sin\theta \; . \tag{3.30}$$

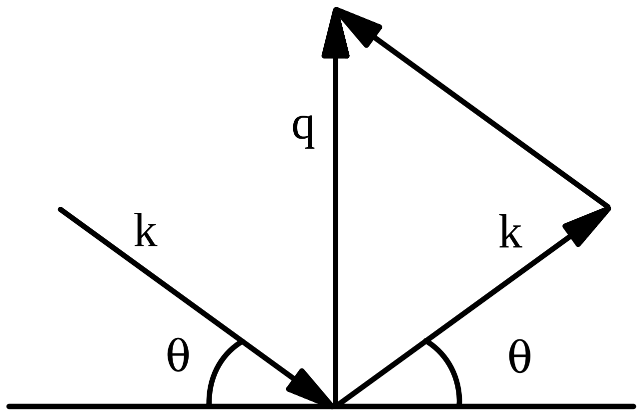

Figure 3.2: Diagram illustrating that $q = 2k\sin\theta$. For elastic scattering, the incoming wavevector $\mathbf{k}_1$ and outgoing wavevector $\mathbf{k}_2$ both have length k. The momentum transfer $\mathbf{q} = \mathbf{k}_2 - \mathbf{k}_1$. From [9].

If the scatterers form a continuous body rather than discrete point particles, we can rewrite (3.28) as an integral

$$S(\mathbf{q}) = \frac{1}{N} \int_V d^3\mathbf{r}_1 \int_V d^3\mathbf{r}_2 \; e^{-i\mathbf{q}\cdot(\mathbf{r}_1-\mathbf{r}_2)} \; \rho(\mathbf{r}_1)\rho(\mathbf{r}_2) \tag{3.31}$$

with $\rho(\mathbf{r})$ as the number density of electrons at position $\mathbf{r}$ and V as the scattering volume.

We can separate the integrals in the structure factor so that

$$S(\mathbf{q}) = \frac{1}{N} A(\mathbf{q}) \; A^*(\mathbf{q}) \tag{3.32}$$

where the "scattering amplitude" is

$$A(\mathbf{q}) = \int_V d^3\mathbf{r}\ e^{-i\mathbf{q}\cdot\mathbf{r}}\ \rho(\mathbf{r})\ . \tag{3.33}$$

If we assume that the product $\rho(\mathbf{r}_1)\rho(\mathbf{r}_2)$ is translationally invariant, then from (3.31) only the *relative* separation of $\mathbf{r}_1$ and $\mathbf{r}_2$ is important, and we can then shift both vectors by $-\mathbf{r}_2$: $\mathbf{r}_1 \leftarrow (\mathbf{r}_1 - \mathbf{r}_2)$ and $\mathbf{r}_2 \leftarrow \mathbf{0}$

$$S(\mathbf{q}) = \frac{V}{N}\int_V d^3(\mathbf{r}_1 - \mathbf{r}_2)\ e^{-i\mathbf{q}\cdot(\mathbf{r}_1-\mathbf{r}_2)}\ \rho(\mathbf{r}_1 - \mathbf{r}_2)\rho(\mathbf{0}) \tag{3.34}$$

and by defining the relative separation vector $\mathbf{r} = \mathbf{r}_1 - \mathbf{r}_2$ and using $\rho = N/V$, then

$$S(\mathbf{q}) = \frac{1}{\rho}\int_V d^3\mathbf{r}\ e^{-i\mathbf{q}\cdot\mathbf{r}}\ \langle\rho(\mathbf{r})\rho(\mathbf{0})\rangle\ . \tag{3.35}$$

The angle brackets denote a time-average. In general, the system will have many fast modes of oscillation (due to thermal motion, for example). Each x-ray scattering event is instantaneous, so in principle, a snapshot of the system could be obtained. However, any signal large enough to be measurable will have to be integrated over an extremely long time period in comparison to these modes. So what is observed is the time-average of these snapshots.

We can also define a modified structure factor with the forward scattering ($\mathbf{q} = 0$) removed.

$$\widetilde{S}(\mathbf{q}) = \frac{1}{\rho}\int_V d^3\mathbf{r}\ e^{-i\mathbf{q}\cdot\mathbf{r}}\ \langle\rho(\mathbf{r})\rho(\mathbf{0})\rangle - N\delta(\mathbf{q}) \tag{3.36}$$

For all practical cases, this will be identical to the standard structure factor, because the $\mathbf{q} = 0$ scattering cannot be experimentally isolated from the primary, unscattered beam. In the x-ray literature, the $N\delta(\mathbf{q})$ term is often neglected.

In this treatment of scattering from multiple objects, we have taken the first Born approximation. In our language of classical continuum fields, the scattered field does not interfere with itself. In the quantum description, this is equivalent to each x-ray photon scattering from, at most, one electron. The assumption of negligible "multiple scattering" is usually valid because the numerical value of the classical electron radius (2.818×10^{-5} Å) is so small. This "kinematic" approximation fails when the observed scattering becomes large. One instance of this is small-angle scattering ($\mathbf{q} \to 0$). Another is when there is a coherent superposition of fields (Bragg diffraction).

3.6.3 Correlation Functions

I will define the two-point correlation function (also known as the pair correlation function) as

$$g(\mathbf{r}_1, \mathbf{r}_2) = \frac{1}{\rho^2}\left[\langle \rho(\mathbf{r}_1)\rho(\mathbf{r}_2)\rangle - \langle \rho(\mathbf{r}_1)\rangle\langle \rho(\mathbf{r}_2)\rangle\right] \tag{3.37}$$

This characterizes the probability of finding a particle at $\mathbf{r}_2$ given one at $\mathbf{r}_1$, relative to the probability of finding a particle at $\mathbf{r}_2$ without any conditions. This expression gives the joint expectation value of the density at a spatial position $\mathbf{r}_2$ and at $\mathbf{r}_1$. If we think of these density elements as particles, then $g(\mathbf{r})$ is the probability of finding a particle at $\mathbf{r}_2$ given a particle at $\mathbf{r}_1$. The angle brackets denote time-averaging, as in the previous section. The time average is assumed to be equivalent to an average over the entire ensemble of microstates available to the system.

For an *translationally invariant* system, $\langle \rho(\mathbf{r}_1, \mathbf{r}_2)\rangle = \langle \rho(\mathbf{r}_1 - \mathbf{r}_2)\rangle$, implying $g(\mathbf{r}_1, \mathbf{r}_2) = g(\mathbf{r}_1 - \mathbf{r}_2)$. For a *homogeneous* system, the one-particle densities are equivalent: $\rho(\mathbf{r}_1) = \rho(\mathbf{r}_2) = \rho$. In general, for large enough $\mathbf{r} = \mathbf{r}_1 - \mathbf{r}_2$, we expect that the particles will be uncorrelated:

$$\lim_{r\to\infty} g(\mathbf{r}) = 0 \tag{3.38}$$

Unfortunately, there is no standard definition for the two-point correlation function. You will also find $g(\mathbf{r}_1, \mathbf{r}_2) = \langle\rho(\mathbf{r}_1)\rho(\mathbf{r}_2)\rangle$, $g(\mathbf{r}_1, \mathbf{r}_2) = \langle\rho(\mathbf{r}_1)\rho(\mathbf{r}_2)\rangle - \langle\rho(\mathbf{r}_1)\rangle\langle\rho(\mathbf{r}_2)\rangle$ in the literature. I prefer the definition (3.37) because it is normalized and the function falls to zero at large distances.

From (3.36), we see that the correlation function is just proportional to the Fourier transform of the modified structure factor. We can shift the coordinate system to place $\mathbf{r}_2$ at the origin. Then the Fourier transform of $\rho g(\mathbf{r})$ is

$$\begin{aligned}
\int_V d\mathbf{r}\; e^{-i\mathbf{q}\cdot\mathbf{r}}\rho g(\mathbf{r}) &= \frac{1}{\rho}\int_V d\mathbf{r}\; e^{-i\mathbf{q}\cdot\mathbf{r}}\left[\langle\rho(\mathbf{r})\rho(\mathbf{0})\rangle - \langle\rho(\mathbf{r})\rangle\langle\rho(\mathbf{0})\rangle\right] && (3.39)\\
&= \frac{1}{\rho}\int_V d\mathbf{r}\; e^{-i\mathbf{q}\cdot\mathbf{r}}\langle\rho(\mathbf{r})\rho(\mathbf{0})\rangle - \rho\int_V d\mathbf{r}\; e^{-i\mathbf{q}\cdot\mathbf{r}} && (3.40)\\
&= \frac{1}{\rho}\int_V d\mathbf{r}\; e^{-i\mathbf{q}\cdot\mathbf{r}}\langle\rho(\mathbf{r})\rho(\mathbf{0})\rangle - \rho V\delta(\mathbf{q}) && (3.41)\\
&= \langle\widetilde{S}(\mathbf{q})\rangle && (3.42)
\end{aligned}$$

The significance of this result is that if we could measure $S(\mathbf{q})$ for all q, we could completely determine the correlation function $g(\mathbf{r})$. In practice, unfortunately, we can only measure $\mathbf{q}$ for a limited range of angles and lengths of q. This limits our knowledge of $g(\mathbf{r})$.

Because it is a convenient abbreviation that I will use in section 3.10, let me mention one more relation.

$$\langle\rho(\mathbf{q})\rho(-\mathbf{q})\rangle = \left\langle\int d\mathbf{r}_1 e^{-i\mathbf{q}\cdot\mathbf{r}_1}\rho(\mathbf{r}_1)\int d\mathbf{r}_2 e^{+i\mathbf{q}\cdot\mathbf{r}_2}\rho(\mathbf{r}_2)\right\rangle \tag{3.43}$$

$$= \int d\mathbf{r}_1 d\mathbf{r}_2 e^{-i\mathbf{q}\cdot(\mathbf{r}_1-\mathbf{r}_2)}\langle\rho(\mathbf{r}_1)\rho(\mathbf{r}_2)\rangle \tag{3.44}$$

$$= S(\mathbf{q}) \tag{3.45}$$

3.7 Scattering from Atoms

Previously (section 3.5), we discussed the scattering from a free electron. In this section, we consider the x-ray scattering from an atom, based upon references [2, 58, 59, 60, 142, 143]. As shown in (3.15), a particle's cross section depends on its mass m as $1/m^2$. Since the proton/electron mass ratio is over 1800, the x-ray scattering from the nucleus is miniscule, and is usually neglected.

Ultimately, we would like to have a function, the *atomic form factor*, which accounts for all the subatomic structure, and tells us how the scattered amplitude is modified (compared with the case of a single free electron). Because this is a common desire, these functions are tabulated in standard references [152, 1, 2].

If we consider just the electron probability density cloud $\rho(\mathbf{r})$ surrounding the nucleus and approximate each of the Z electrons as being free, then we arrive at the standard form factor

$$f_0(q, Z) = \int d\mathbf{r}\ e^{-i\mathbf{q}\cdot\mathbf{r}}\rho(\mathbf{r}) = \int_0^\infty 4\pi r^2 dr\ \rho(r)\ \frac{\sin qr}{qr} \tag{3.46}$$

(The latter equality holds in the case that $\rho(\mathbf{r})$ is spherically symmetric.) By substitution, it is clear that $f_0 = Z$ for $q = 0$. The standard atomic form factors for the elements Pt, Cu, and Cl are plotted in figure 3.3. This f_0 term is the primary component of the atomic form factor f, because for energies far above 100 eV (and all of the data in this dissertation were taken with x-rays in the keV range), we can basically approximate most atomic electrons as being free; X-rays are far too energetic to efficiently excite intra-atomic energy transitions.

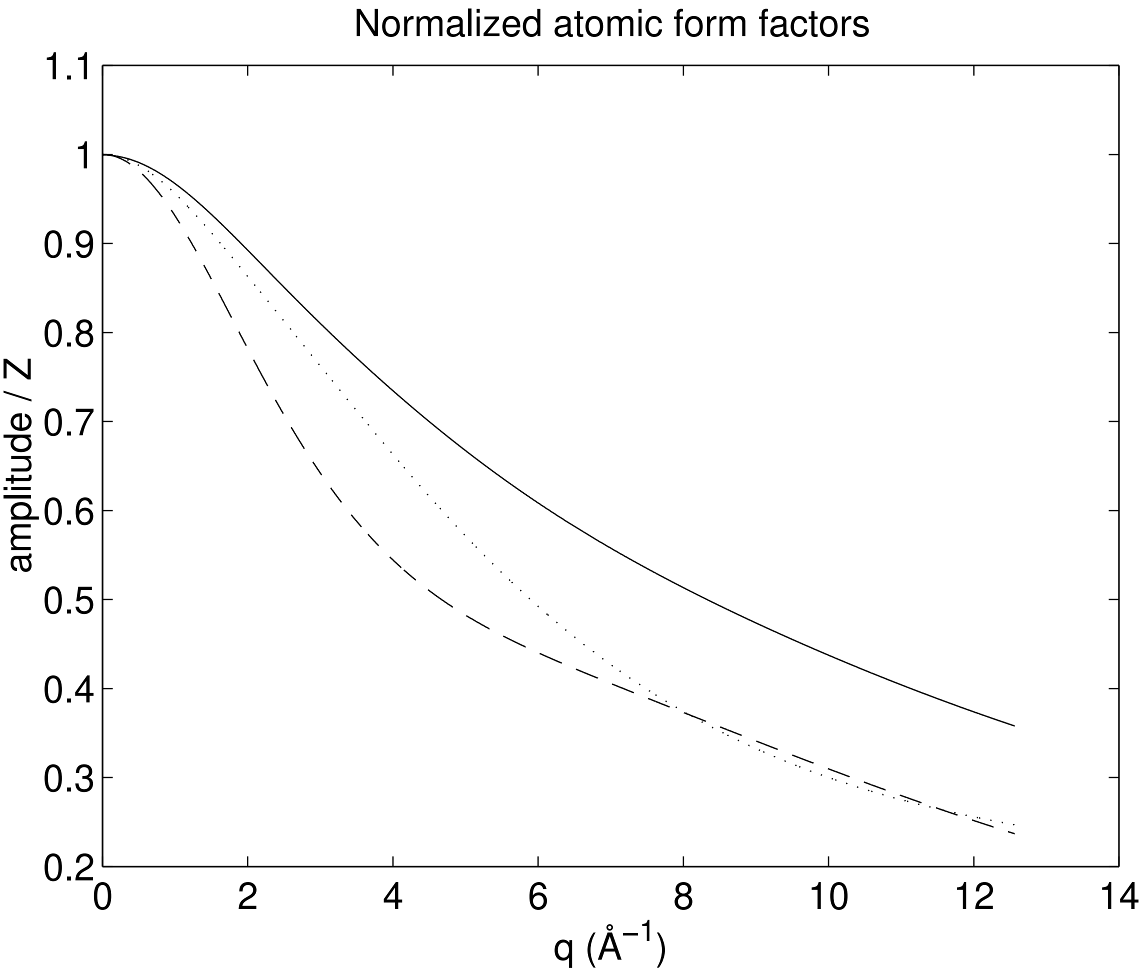

Figure 3.3: Standard atomic form factors $f_0(q)$, normalized by atomic number Z, for Pt (solid), Cu (dotted), and Cl (dashed). Note that $f_0(0) = Z$. From [151].

However, the free-electron assumption is only an approximation, and fails most noticeably near "adsorption edges". When the x-ray energy is tuned close to an absorption edge, it can eject a core-level electron from the atom. (This is related to the electron-induced ionization discussed in section 3.3).

Deviations of the measured form factor f from f_0 are known as as "anomalous dispersion". Typically, this modification to the amplitude is separated into a real term $f'(E,Z)$ and an imaginary term $f''(E,Z)$. The latter term allows for a change of phase in the scattered beam and is manifested as absorption. Physically, the anomalous dispersion arises from the resonance of the incident x-ray with differences between atomic energy levels.

Summarizing the various terms that comprise the atomic form factor $f(q,E,Z)$:

$$f(q,E,Z) = f_0(q,Z) + f'(E,Z) + f''(E,Z) + f_{NT} \tag{3.47}$$

where f_{NT} is the nuclear Thomson scattering, usually neglected. The scattering amplitude from an atom is the amplitude from a single free electron, multiplied by this *atomic form factor*, $f(q,E,Z)$. Here E is the energy of the incident x-ray photon, Z is the atomic number, and $q = \frac{4\pi}{\lambda}\sin\theta$ (equation (3.30)) is the momentum transfer (discussed in section 3.6.2).

3.7.1 Absorption

Absorption of x-rays is caused by an incident x-ray striking an atom and causing a core level electron to be ejected [61]. This is simply the photoelectric effect, which is usually presented in the context of ultraviolet photons incident upon the outer shells. Historically, this was one of the most dramatic experiments leading to the quantum paradigm. After the photoelectron is ejected, the atom is in an excited state. Just as described in section 3.3, an electron will fall into the vacated state and emit a characteristic x-ray; this process is called “fluorescence”. Because the electron falls from an atomic level and not from the vacuum, the fluorescence energy is always less than the energy of the absorbed x-ray.

Empirically, the absorption of x-rays by matter is observed to be

$$I_z = I_0 \exp(-\mu z) \tag{3.48}$$

where μ is proportional to the electronic density. At these large x-ray energies, the phase (solid, liquid, gas) of the material is unimportant, except in its effect upon the mean density. The more fundamental quantity (and the one most frequently tabulated) is the mass absorption coefficient μ/ρ_m, where ρ_m is a mass density. Since x-rays scatter from atoms, it is sufficient to add up the elemental contributions to determine a molecular compound's mass absorption coefficient, as

$$\frac{\mu}{\rho_m} = \sum_i w_i \left(\frac{\mu}{\rho_m}\right)_i \tag{3.49}$$

where w_i is the weight fraction of element i.

The absorption coefficient μ_i peaks dramatically near energies that correspond to the absorption edges. Following each edge is a branch of the absorption curve following the form [62]

$$\mu/\rho_m = k\lambda^3 Z^3 \tag{3.50}$$

where k is a constant that has a different value for each branch. An illustration is provided in figure 3.4. For this fictitious element, the edge is at $\lambda = 2$Å.

In order to minimize absorption, we used an incident x-ray energy of 8800 eV, near the bottom of the absorption branch, but sufficiently far from the Cu K

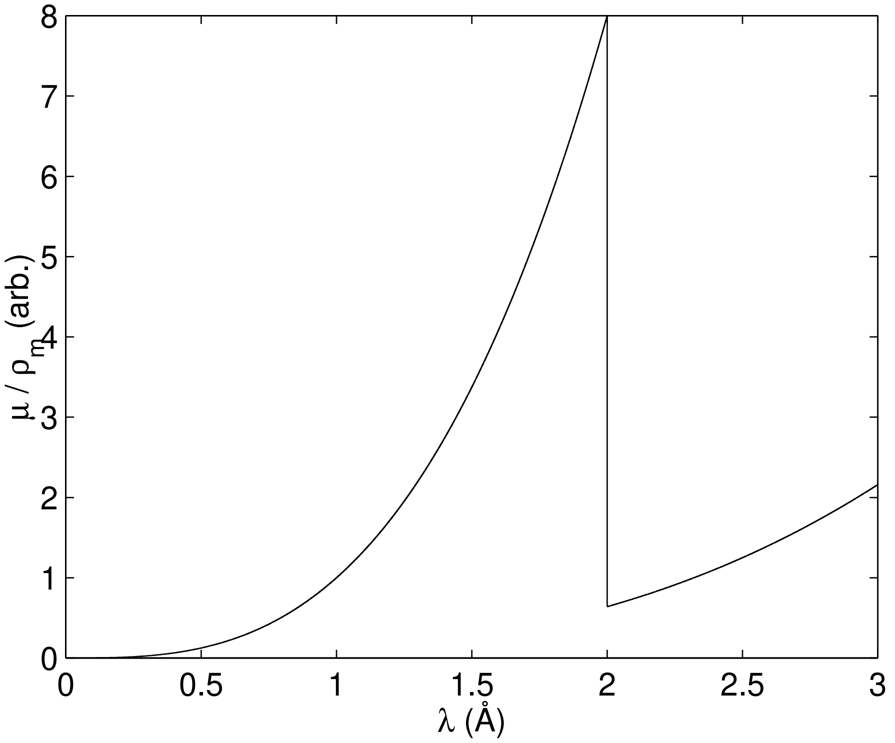

Figure 3.4: An illustration of a mass absorption coefficient vs. wavelength. This is intended only for illustration, so it corresponds to no element. The sharp drop in intensity is known as the absorption edge.

(8979 eV) edge. This choice of energy also reduced fluorescence from the Cu atoms that occurs at or above the absorption edge.

3.8 Crystals

A Bravais lattice is the set of points that can be reached from a single point by applying translation vectors. These translation vectors are called "basis vectors" and are equal to the number of dimensions of the space of the lattice. For real crystals described by Bravais lattices, there are three basis vectors. Calling these basis vectors $\mathbf{a}_x$, $\mathbf{a}_y$, $\mathbf{a}_z$, the Bravais lattice consists of the set of vectors $\{\mathbf{R}\}$,

$$\mathbf{R} = n_x\mathbf{a}_x + n_y\mathbf{a}_y + n_z\mathbf{a}_z \tag{3.51}$$

where n_a, n_b, n_c span all the integers.

Any Bravais lattice also has a reciprocal lattice [10], which is the set of plane wave vectors $\{\mathbf{q}\}$ that have the same periodicity as the Bravais lattice. That is, $e^{i\mathbf{q}\cdot\mathbf{r}} = e^{i\mathbf{q}\cdot(\mathbf{R}+\mathbf{r})}$, or

$$e^{i\mathbf{q}\cdot\mathbf{R}} = 1 \tag{3.52}$$

As the symmetric nature of (3.52) makes clear, the reciprocal lattice to the reciprocal lattice is just the original direct lattice. In other words, the (direct) Bravais lattice in real space and the reciprocal lattice are dual.

3.9 Diffraction from Crystals

3.9.1 Infinite Crystal

Consider an infinite array of point charges

$$\rho(\mathbf{r}) = \sum_{\mathbf{R}} \delta(\mathbf{r} - \mathbf{R}) \tag{3.53}$$

where R are the Bravais lattice vectors. But for simplicity, let's begin with the case of an infinite one-dimensional crystal. The lattice vectors are $\mathbf{R} = ja$, where j runs over all integers, so the scattering amplitude is

$$A(q) = \sum_j e^{-iqja} = \sum_{j=-\infty}^{\infty} \left(e^{-iqa}\right)^j = \sum_{j=1}^{\infty} \left(e^{iqa}\right)^j + \sum_{j=0}^{\infty} \left(e^{-iqa}\right)^j \ . \tag{3.54}$$

Ordinarily, we would use

$$\sum_{n=0}^{\infty} x^n = \frac{1}{1-x} \ , \tag{3.55}$$

but this fails the requirement $|x| < 1$ for convergence. However, we can multiply e^{-iqa} by a small correction factor $e^{-\mu}$ where $\mu > 0$ and take the limit $\mu \to 0^+$ after the sum is taken. Then the sums in (3.54) converge to

$$A(q) = \delta(qja - 2n\pi) = \delta(qR - 2n\pi) \tag{3.56}$$

where n is any integer. This mathematical device has a basis in physical reality. As discussed in section 3.7.1, all crystals absorb some fraction of the x-rays that diffract through them. Other processes that cause a finite scattering intensity are grouped under the term *extinction* [144].

The calculation for a three-dimensional crystal is just a trivial extension of the one-dimensional case. Take a Bravais lattice as

$$\rho(r) = \sum_{\mathbf{R}} \delta(\mathbf{r} - \mathbf{R}) = \sum_{\mathbf{R}} \delta(\mathbf{r}_x - j_x \mathbf{a}_x)\, \delta(\mathbf{r}_y - j_y \mathbf{a}_y)\, \delta(\mathbf{r}_z - j_z \mathbf{a}_z) \tag{3.57}$$

where $\{\mathbf{R}\}$ corresponds to $\{j_x, j_y, j_z\}$.

$$\begin{aligned} A(\mathbf{q}) &= \sum_{\mathbf{R}} e^{-i\mathbf{q}\cdot\mathbf{R}} && (3.58) \\ &= \sum_{\{j_x, j_y, j_z\}} e^{-iq_x j_x a_x}\, e^{-iq_y j_y a_y}\, e^{-iq_z j_z a_z} \\ &= \sum_{j_x} e^{-iq_x j_x a_x} \sum_{j_y} e^{-iq_y j_y a_y} \sum_{j_z} e^{-iq_z j_z a_z} \\ &= \delta(q_x a_x - 2H\pi)\, \delta(q_y a_y - 2K\pi)\, \delta(q_z a_z - 2L\pi) && (3.59) \end{aligned}$$

For nonzero $A(\mathbf{q})$, we thus require the Laue conditions

$$q_x a_x = 2\pi H \tag{3.60}$$

$$q_y a_y = 2\pi K \tag{3.61}$$

$$q_z a_z = 2\pi L \tag{3.62}$$

where the indices H, K, L span all of the integers. These conditions define a lattice of points in reciprocal space. These points are just the reciprocal lattice described by (3.52), as we can show with a simple example. The vector $\mathbf{q}$ is just

$$\mathbf{q} = q_x \widehat{q}_x + q_y \widehat{q}_y + q_z \widehat{q}_z \tag{3.63}$$

where the $\widehat{q}_i$ represent arbitrary unit vectors that form a basis in reciprocal space. For simplicity, take

$$\widehat{a}_i \cdot \widehat{q}_i = \delta_{ij} \ , \tag{3.64}$$

although we could make some other choice. Then

$$\mathbf{q}\cdot\mathbf{R} = n_x a_x q_x + n_y a_y q_y + n_z a_z q_z \tag{3.65}$$

$$= 2\pi H n_x + 2\pi K n_y + 2\pi L n_z \; . \tag{3.66}$$

This is equivalent to $e^{i\mathbf{q}\cdot\mathbf{R}} = 1$, the definition of the reciprocal lattice (3.52). We might choose another basis for $\widehat{q}_i$, instead of (3.64), but $\mathbf{q}\cdot\mathbf{R}$ will remain the same. So, the diffraction pattern from a Bravais lattice is its dual reciprocal-space Bravais lattice.

Take d as the projection of a given $\mathbf{R}$ along $\mathbf{q}$. This d is the distance between two planes of the lattice. From $\mathbf{q}\cdot\mathbf{R} = qd = 2n\pi$ and the definition of q (3.30), we recover Bragg's law:

$$n\lambda = 2d\sin\theta \; . \tag{3.67}$$

3.9.2 Lattices with a Basis

In this dissertation, we will be most concerned with the structure of platinum. This is a face-centered cubic crystal, which can be visualized as a cubic crystal with an extra atom at the center of each of the cubic faces. Some crystal structures are not Bravais lattices[1], for example, silicon and diamond. They can, however, be described as a face-centered cubic crystal with another face-centered cubic crystal superimposed upon it. The second lattice has a relative displacement of 1/4 along

[1] I will not discuss quasicrystals, fascinating systems wherein the diffraction pattern exhibits (at least) five-fold symmetry. This implies that the real-space structure cannot even be even remotely described by a (three-dimensional) Bravais lattice.

the cubic body diagonal. The "diamond structure" is described by vectors that run over the Bravais lattice, but also include the basis vector for this displacement.

Although the face-centered cubic structure is a Bravais lattice, it is convenient to describe it as a simple cubic lattice with a basis. The basis vectors in this case describe the atoms on the faces. For a simple cubic crystal with basis vectors $a\widehat{x}$, $a\widehat{y}$, and $a\widehat{z}$, the displacement basis vectors that generate the face-centered cubic crystal are

$$\mathbf{d}_1 = 0 \tag{3.68}$$

$$\mathbf{d}_2 = \frac{a}{2}(\widehat{x} + \widehat{y}) \tag{3.69}$$

$$\mathbf{d}_3 = \frac{a}{2}(\widehat{x} + \widehat{z}) \tag{3.70}$$

$$\mathbf{d}_4 = \frac{a}{2}(\widehat{y} + \widehat{z}) \tag{3.71}$$

For a crystalline sample, we can divide the space into unit cells that are repeated over all Bravais lattice vectors. Then we can consider the scattering from one unit cell and replicate it over the Bravais lattice. For the face-centered cubic crystal, the scattering amplitude due to one cube is

$$A(\mathbf{q}) = \sum_{i=1}^{4} e^{i\mathbf{q}\cdot\mathbf{d}} = 1 + e^{i\pi(H+K)} + e^{i\pi(H+L)} + e^{i\pi(K+L)} \tag{3.72}$$

$$= 1 + (-1)^{H+K} + (-1)^{H+K} + (-1)^{K+L} \tag{3.73}$$

$$= 4 \text{ if } H, K, L \text{ all odd or all even}$$

$$0 \text{ if } H, K, L \text{ mixed}$$

So the diffraction pattern will be identical that of a simple cubic lattice, except that intensity at H, K, L values which are all odd or all even will be enhanced, and the intensity at other H, K, L values will be extinguished.

3.10 Thermal Effects and Inelastic Scattering

This section is based upon [11, 63, 145, 146, 47]. Consider an ideal crystal as in (3.53),

$$\rho(r) = \sum_{\mathbf{R}} \delta(\mathbf{r} - \mathbf{R}) \tag{3.74}$$

The structure factor from a Bravais lattice is found by applying the definition of the structure factor (3.32) to the scattering amplitude from a Bravais lattice (3.58),

$$S(\mathbf{q}) = \sum_{\mathbf{R},\mathbf{R}'} e^{-i\mathbf{q}\cdot(\mathbf{R}-\mathbf{R}')} \tag{3.75}$$

To consider an inelastic scattering process, take the dynamical structure factor [8]

$$\begin{aligned} S(\mathbf{q},\omega) &= \frac{1}{N}\int_{-\infty}^{\infty} dt \int_V d^3\mathbf{r}_1 \int_V d^3\mathbf{r}_2 \; e^{-i\mathbf{q}\cdot(\mathbf{r}_1-\mathbf{r}_2)+i\omega t} \; \rho(\mathbf{r}_1, t=0)\rho(\mathbf{r}_2, t) \\ &= \frac{1}{N}\int_{-\infty}^{\infty} dt \; e^{i\omega t} \; \langle \rho(\mathbf{q})\rho(-\mathbf{q}, t)\rangle \; , \end{aligned} \tag{3.76}$$

and allow the atoms to oscillate about their respective mean positions such that their instantaneous positions are $\mathbf{R} + \mathbf{u}(\mathbf{R})$. Then,

$$S(\mathbf{q},\omega) = \frac{1}{N}\sum_{RR'} e^{-i\mathbf{q}\cdot(\mathbf{R}-\mathbf{R}')} \int dt \; e^{i\omega t} \langle e^{i\mathbf{q}\cdot\mathbf{u}(\mathbf{R}')} e^{-i\mathbf{q}\cdot\mathbf{u}(\mathbf{R},\mathbf{t})}\rangle \; . \tag{3.77}$$

Take the harmonic approximation, which is that $\mathbf{u}(\mathbf{R})$ has a Gaussian distribution (appendix A). Specifically, use the result (A.13) to evaluate the product in the angle brackets:

$$\langle e^{i\mathbf{q}\cdot\mathbf{u}(\mathbf{R}')} e^{-i\mathbf{q}\cdot\mathbf{u}(\mathbf{R},\mathbf{t})}\rangle = e^{-\frac{1}{2}\langle[\mathbf{q}\cdot\mathbf{u}(\mathbf{R}')]^2\rangle} e^{-\frac{1}{2}\langle[\mathbf{q}\cdot\mathbf{u}(\mathbf{R},\mathbf{t})]^2\rangle} e^{\langle[\mathbf{q}\cdot\mathbf{u}(\mathbf{R}')][\mathbf{q}\cdot\mathbf{u}(\mathbf{R},\mathbf{t})]\rangle} \; . \tag{3.78}$$

The Debye-Waller factor $W(\mathbf{q})$ is defined as

$$W(\mathbf{q}) \equiv \frac{1}{2}\langle[\mathbf{q}\cdot\mathbf{u}(\mathbf{R}')]^2\rangle = \frac{1}{2}\langle[\mathbf{q}\cdot\mathbf{u}(\mathbf{R},\mathrm{t})]^2\rangle = \frac{1}{2}\langle[\mathbf{q}\cdot\mathbf{u}(\mathbf{0})]^2\rangle\ , \tag{3.79}$$

and then the structure factor is

$$S(\mathbf{q},\omega) = e^{-2W} \int dt\ e^{i\omega t} \sum_R e^{-i\mathbf{q}\cdot\mathbf{R}} e^{\langle[\mathbf{q}\cdot\mathbf{u}(\mathbf{0})][\mathbf{q}\cdot\mathbf{u}(\mathbf{R},\mathrm{t})]\rangle}\ . \tag{3.80}$$

Expanding the exponential $e^{\langle[\mathbf{q}\cdot\mathbf{u}(\mathbf{0})][\mathbf{q}\cdot\mathbf{u}(\mathbf{R},\mathrm{t})]\rangle}$, the zeroth-order term (replacing the exponential with unity) yields

$$S(\mathbf{q},\omega) = e^{-2W} \int dt\ e^{i\omega t} \sum_R e^{-i\mathbf{q}\cdot\mathbf{R}} \tag{3.81}$$

which evaluates to

$$S(\mathbf{q},\omega) = e^{-2W}\ \delta(\omega) \sum_G \delta(\mathbf{q}-\mathbf{G}) \tag{3.82}$$

where $\{\mathbf{G}\}$ is the reciprocal lattice to $\{\mathbf{R}\}$. This is just the elastic scattering from Bragg peaks derived in previous sections. So the net effect of the small thermal motions is to lower the Bragg peak intensities by a factor of e^{-2W}. The widths, however, are unchanged.

The extra intensity goes into the other modes, which are the higher-order terms in the expansion of the exponential. The scattering from these modes is called "thermal diffuse scattering". The successive terms in the expansion consists of zero, one-phonon, two-phonon, etc. processes. While the zeroth-order term is elastic, all the others are not. The first-order thermal diffuse scattering has a discrete energy spectrum, while the second-order and higher terms are smooth functions of scattered x-ray energy [12]. The second-order thermal diffuse scattering has the same intensity as Compton scattering, and is often ignored.

It is often difficult to separate out the elastic from the inelastic terms, because of the poor relative energy resolution in x-ray detection. The incident x-ray energy is on the order of keV, while the thermal excitations are on the order of $k_B T$, 1/40 eV at room temperature. In practice, we are accepting such a broad range of energies that *all* energy transfers are selected. This is equivalent to performing an integration of (3.76) over all energy transfers ω

$$\begin{aligned} \int d\omega\ S(\mathbf{q},\omega) &= \int d\omega\ \frac{1}{N}\int_{-\infty}^{\infty} dt\ e^{i\omega t}\ \langle \rho(\mathbf{q})\rho(-\mathbf{q},t)\rangle \\ &= \frac{1}{N}\int_{-\infty}^{\infty} dt\ \delta(t)\langle \rho(\mathbf{q})\rho(-\mathbf{q},t)\rangle = \langle \rho(\mathbf{q})\rho(-\mathbf{q})\rangle \end{aligned} \tag{3.83}$$

Thus, x-ray diffraction measures the static structure factor automatically. Although sometimes called elastic scattering (because there is no energy dependence), this is a misnomer. In fact, we are integrating over all energy transfers ω, not selecting out the elastic ($\omega = 0$) term.

3.11 X-ray Scattering from Surfaces

X-ray scattering from surfaces is usually presented in either of two ways. In section 3.11.1, I present the method of truncating an infinite crystal, popularized by Robinson [111]. The following section (3.11.2) describes the more traditional approach from classical electrodynamics. The final section (3.11.3) establishes the connection between these two approaches.

3.11.1 Truncating the Infinite Crystal

This section builds upon the treatment of the infinite crystal in section 3.9, and extends it to semi-infinite and finite crystals.

Semi-Infinite Crystal

In analogy with (3.54), consider an ideal semi-infinite crystal. One face of the crystal is presumed to be truncated at $x = 0$ while the opposite "end" stretches to infinity. As before, we begin with the one-dimensional case, which illustrates the relevant behavior.

$$A(q) = \sum_{j=0}^{\infty} e^{-iqja} = \frac{1}{1 - e^{-iqa}} \tag{3.84}$$

Note that the sum over j now runs from $0 \ldots \infty$. Like the infinite crystal (3.56), this function is infinite-valued for $qa = 2n\pi$. Unlike the infinite crystal, (3.84) has non-zero values everywhere else. The structure factor has a minimum value of $1/4$:

$$S(q) = |A(q)|^2 = \frac{1}{4} \frac{1}{\sin^2 \frac{qa}{2}} \tag{3.85}$$

Finite Crystal

Now, we truncate the crystal at both ends, so that it is a one-dimensional crystal containing N scatterers.

Using the relation

$$\sum_{n=0}^{N-1} x^n = \frac{1 - x^N}{1 - x} \tag{3.86}$$

then

$$A(q) = \sum_{j=0}^{N-1} e^{-iqja} = \frac{1 - e^{-iqNa}}{1 - e^{-iqa}} \tag{3.87}$$

and

$$S(q) = \frac{\sin^2 \frac{1}{2}Nqa}{\sin^2 \frac{1}{2}qa} \tag{3.88}$$

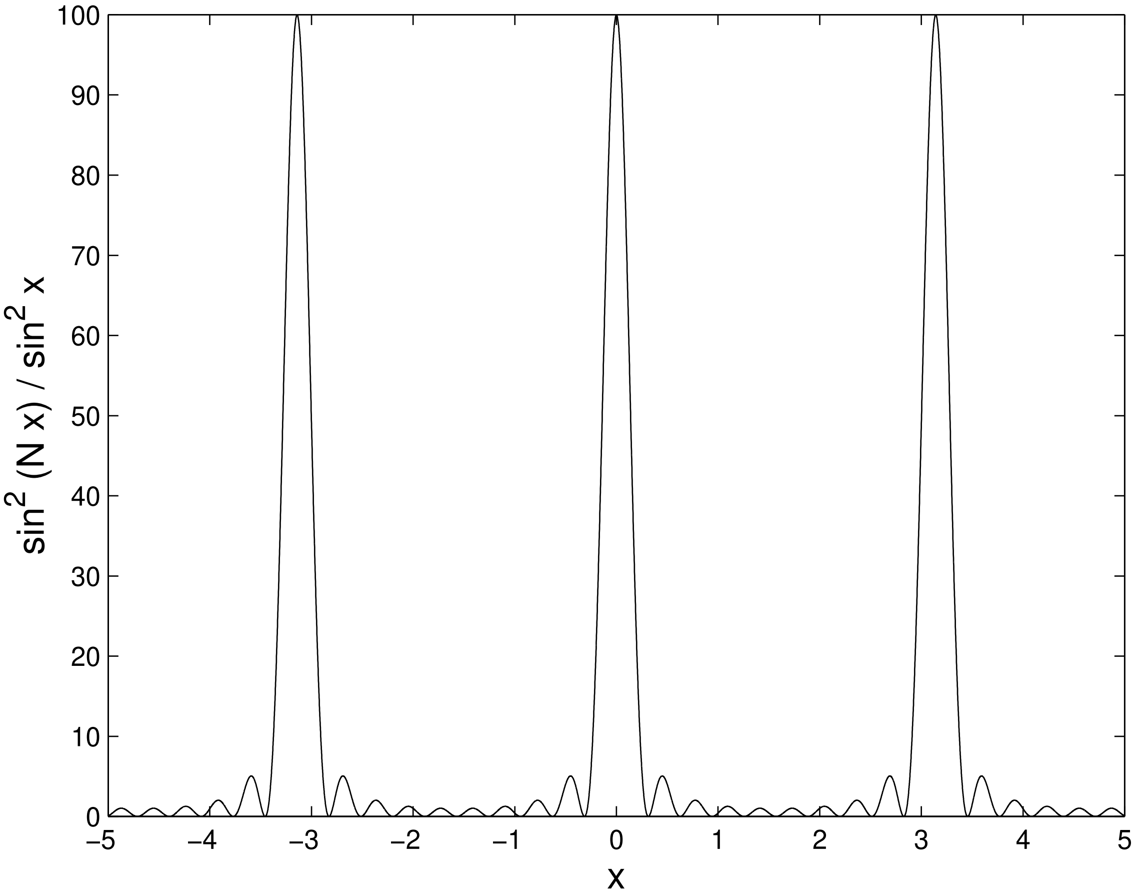

Figure 3.5: Graph of $\frac{\sin^2 Nx}{\sin^2 x}$ vs. x, for $N = 10$.

The structure factor here is just like the diffraction intensity from a diffraction grating with N slits (shown in figure 3.5). Near the Bragg diffraction peaks ($qa \rightarrow 2\pi n$), the limit $\lim_{x\rightarrow 0} \frac{\sin Nx}{\sin x} = N$. Because the crystal is finite, the structure factor maxima are now N^2, not infinite. The minimum value is zero, which is also in contrast with the semi-infinite crystal, but identical to the infinite crystal.

The extension to three dimensions is straightforward [111]. Consider a three-dimensional crystal with N_x, N_y, N_z scatterers in the x, y, z directions. The scattering amplitude is then

$$A(q) = \left(\sum_{j_x=0}^{N_x-1} e^{ij_x \mathbf{q}\cdot\mathbf{a}_x} \right) \left(\sum_{j_y=0}^{N_y-1} e^{ij_y \mathbf{q}\cdot\mathbf{a}_y} \right) \left(\sum_{j_z=0}^{N_z-1} e^{ij_z \mathbf{q}\cdot\mathbf{a}_z} \right) \tag{3.89}$$

Each factor is just a geometric series, which may be summed to yield

$$A(\mathbf{q}) = \left(\frac{e^{iN_x \mathbf{q}\cdot\mathbf{a}_x} - 1}{e^{i\mathbf{q}\cdot\mathbf{a}_x} - 1} \right) \left(\frac{e^{iN_y \mathbf{q}\cdot\mathbf{a}_y} - 1}{e^{i\mathbf{q}\cdot\mathbf{a}_y} - 1} \right) \left(\frac{e^{iN_z \mathbf{q}\cdot\mathbf{a}_z} - 1}{e^{i\mathbf{q}\cdot\mathbf{a}_z} - 1} \right) \tag{3.90}$$

The structure factor is just $S(\mathbf{q}) = A(\mathbf{q})A^*(\mathbf{q})$, so

$$S(\mathbf{q}) = \left(\frac{\sin^2 \frac{1}{2} N_x \mathbf{q}\cdot\mathbf{a}_x}{\sin^2 \frac{1}{2}\mathbf{q}\cdot\mathbf{a}_x} \right) \left(\frac{\sin^2 \frac{1}{2} N_y \mathbf{q}\cdot\mathbf{a}_y}{\sin^2 \frac{1}{2}\mathbf{q}\cdot\mathbf{a}_y} \right) \left(\frac{\sin^2 \frac{1}{2} N_z \mathbf{q}\cdot\mathbf{a}_z}{\sin^2 \frac{1}{2}\mathbf{q}\cdot\mathbf{a}_z} \right) \tag{3.91}$$

Taking the $N_x \to \infty$, $N_y \to \infty$ limit but holding N_z finite, we obtain a physically reasonable depiction of a crystal surface.

$$S(\mathbf{q}) = \delta(q_x a_x - 2H\pi)\, \delta(q_y a_y - 2K\pi) \left(\frac{\sin^2 \frac{1}{2} N_z \mathbf{q}\cdot\mathbf{a}_z}{\sin^2 \frac{1}{2}\mathbf{q}\cdot\mathbf{a}_z} \right) \tag{3.92}$$

In comparison with the infinite crystal, the two Laue conditions (3.60) on q_x and q_y are maintained, but the condition on q_z has been relaxed. Where the final Laue condition $q_z a_z = 2\pi L$ holds, a Bragg peak will exist. The difference is that there is still residual scattering at other q_z. The resultant intensity is sharp in q_x and q_y, but diffuse along q_z. These rods of scattering that arise from the truncation of the crystal lattice are thus known as "crystal truncation rods" (CTR).

As mentioned in section 3.9.1, absorption and extinction limit the x-ray scattering intensity. Because of this finite penetration depth, even a truly semi-infinite crystal will scatter like a finite crystal. A reasonable order-of-magnitude for N_z is

1000, given a penetration depth $\approx 1\mu$m [111]. Figure 3.6 plots (3.92), proportional to the intensity along a CTR.

3.11.2 Reflectivity from Smooth Surfaces

An alternative treatment is to consider x-ray scattering from a surface as an example of the more general problem of reflection and refraction at a boundary between two dielectric media. Since x-rays are just electromagnetic radiation, this should be perfectly valid. For the moment, however, we neglect the atomistic nature of the sample and assume it to be a smooth, continuous structure. The atomic periodicity can be added in later (section 3.11.3).

Fresnel Equations

Consider a smooth interface between air ($n = 1$) and a block of amorphous material ($n < 1$ for x-rays). This ties into the classical electrodynamic treatment described by Jackson [84], with $n' \to n$, $n \to 1$, and $\mu = \mu'$. Jackson uses θ_i, the angle between the incident beam and the surface normal. For consistency with the rest of the dissertation, I write results in terms of its complementary angle α between the incident beam and the surface.

Then the component of the electric field perpendicular to the plane of reflection are

$$\frac{E_t^\perp}{E_0} = \frac{2\sin\alpha}{\sin\alpha + \sqrt{n^2 - \cos^2\alpha}} \tag{3.93}$$

$$\frac{E_r^\perp}{E_0} = \frac{\sin\alpha - \sqrt{n^2 - \cos^2\alpha}}{\sin\alpha + \sqrt{n^2 - \cos^2\alpha}} \tag{3.94}$$

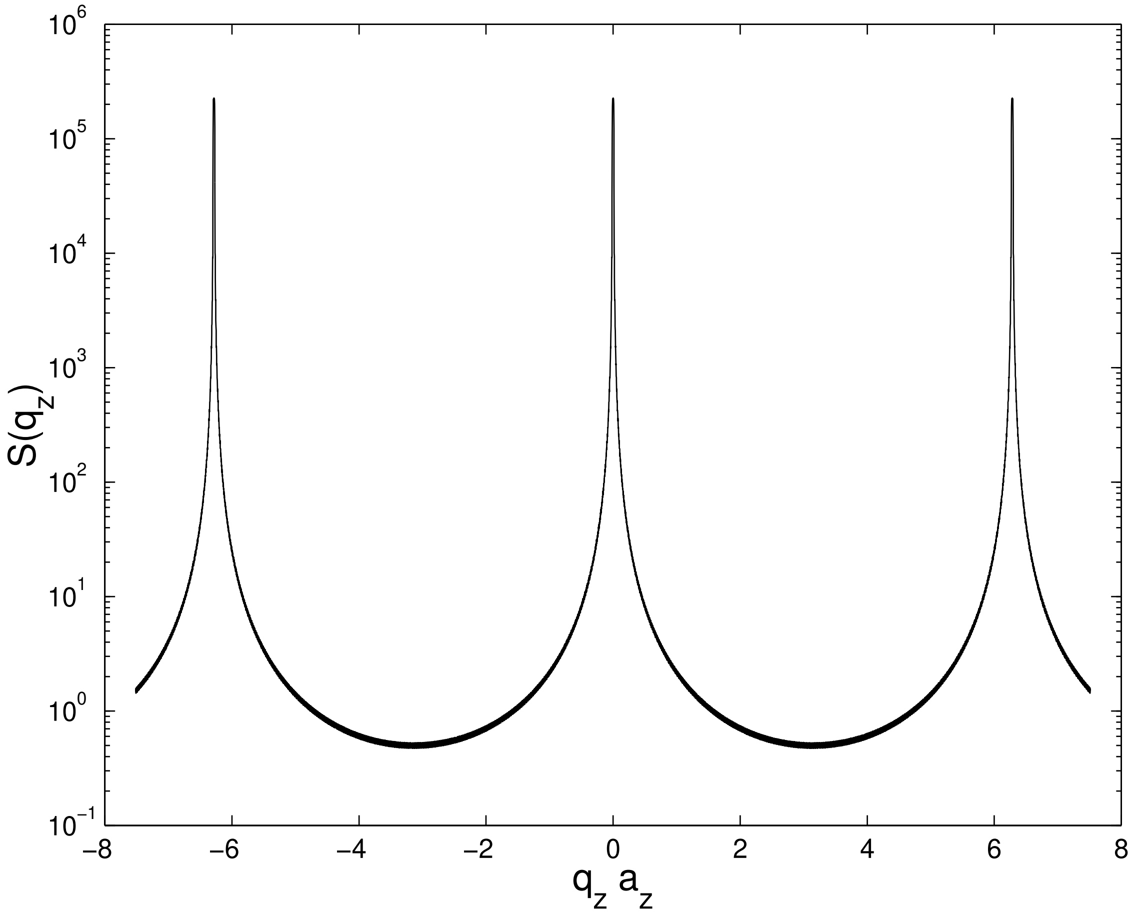

Figure 3.6: A logarithmic plot of $S(\mathbf{q})$ vs. q_z as given in (3.92) for $N_z = 1000$. This is the same function shown in figure 3.5, but with a larger N_z. Also, a finite resolution function has been convolved through the data. This eliminates the numerous minima seen in figure 3.5, and is reasonable from an experimental standpoint. The minimum value is near $1/2$, because $\langle \sin^2 x \rangle = 1/2$. Without the convolution, the minimum value is zero.

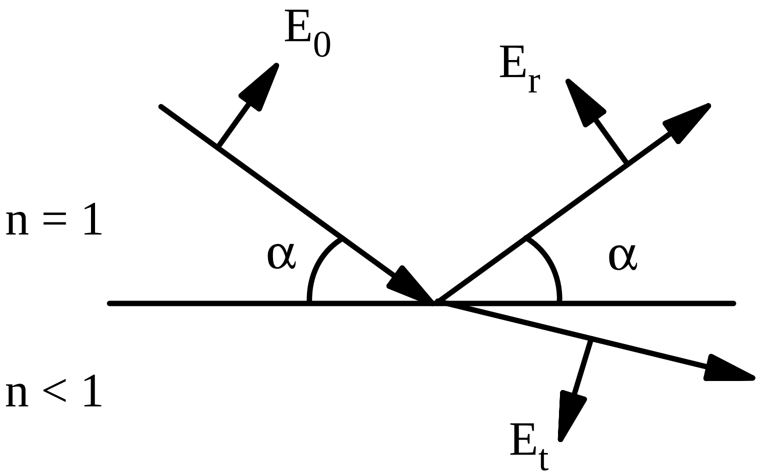

Figure 3.7: Diagram for the Fresnel equations.

and the parallel components are

$$\frac{E_t^{||}}{E_0} = \frac{2n\sin\alpha}{n^2\sin\alpha + \sqrt{n^2 - \cos^2\alpha}} \tag{3.95}$$

$$\frac{E_r^{||}}{E_0} = \frac{n^2\sin\alpha - \sqrt{n^2 - \cos^2\alpha}}{n^2\sin\alpha + \sqrt{n^2 - \cos^2\alpha}} \tag{3.96}$$

The Fresnel reflection and transmission coefficients are plotted in figure 3.8. If $n < 1$, as we will show is true for x-rays incident on most materials, then there exists a critical angle α_c such that $n = \cos\alpha_c$. For $\alpha < \alpha_c$, $\cos\alpha > n$, so the square roots become imaginary and the magnitude of E_r/E_0 is unity for both polarizations. This is termed total external reflection.

Index of Refraction

While a long derivation of the index of refraction can be found in Warren [147], a simpler and more illuminating treatment can be found in Jackson [85]. I will not repeat the entire model here, but just connect the results to our discussion.

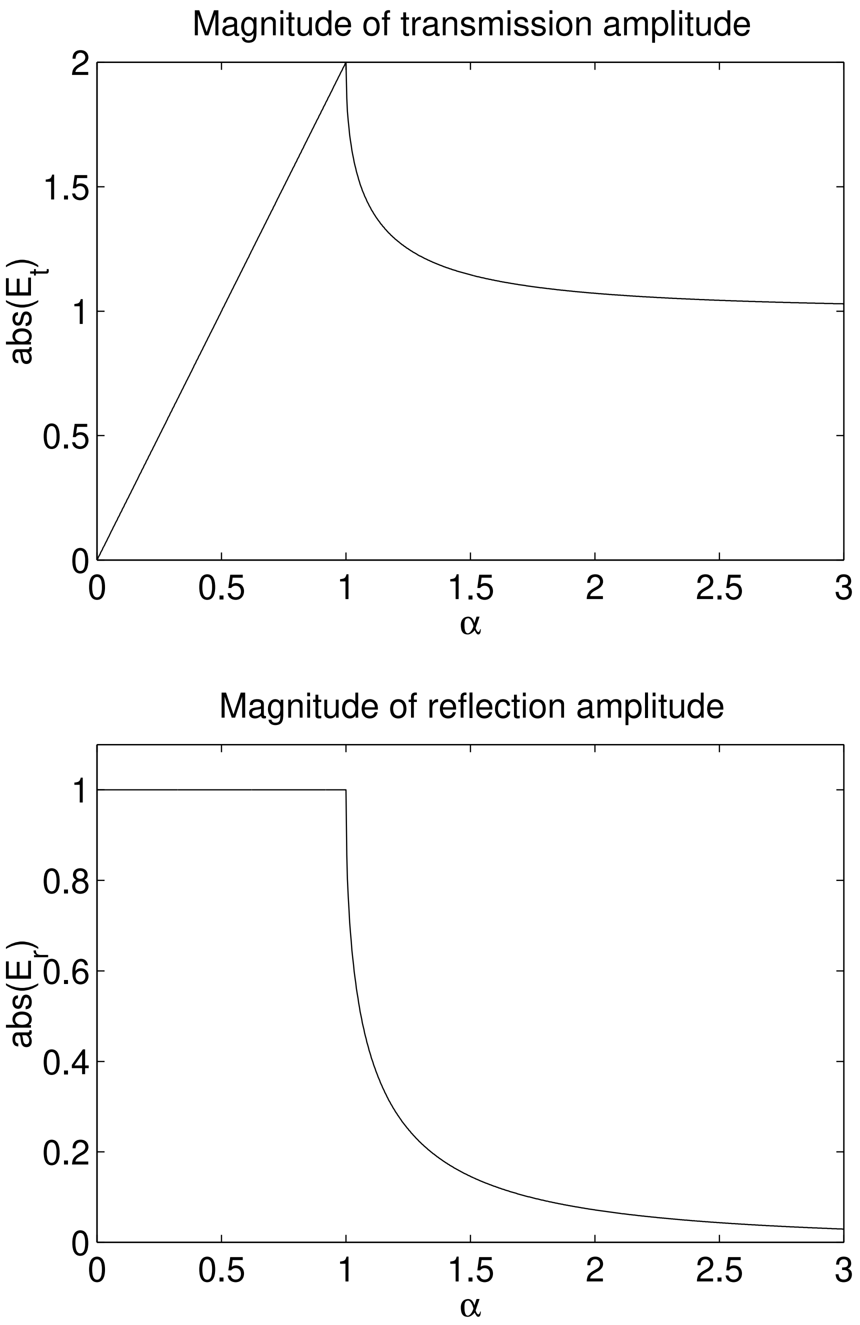

Figure 3.8: Fresnel reflection and transmission coefficients. In this example, $\alpha_c = 1°$. The transmission is sharply peaked at the critical angle, then quickly falls to unity.

For large enough photon energies ($\hbar\omega$), the dielectric constant approaches the "plasma limit" and

$$\epsilon(\omega) \approx 1 - \omega_p^2/\omega^2 \tag{3.97}$$

where the "plasma frequency" is

$$\omega_p^2 = 4\pi NZe^2/m \tag{3.98}$$

Here, N is the density of atoms per unit volume and Z is the atomic number. The index of refraction is defined as $n = \sqrt{\mu\epsilon}$ and we can assume that $\mu \approx 1$. Since the refractive index is close to unity, we can expand the exponential

$$n = \sqrt{1 - (\omega_p^2/\omega^2)} \approx 1 - \frac{1}{2}\frac{\omega_p^2}{\omega^2} = 1 - \frac{2\pi NZe^2}{m\omega^2} \,. \tag{3.99}$$

Using $\omega = 2\pi c/\lambda$, the classical electron radius $r_0 = e^2/mc^2$, and the electronic density $\rho = NZ$, we find that the index of refraction is

$$n = 1 - r_0\frac{\rho\lambda^2}{2\pi} \equiv 1 - \delta \tag{3.100}$$

Our assertion that $\delta \ll 1$ will hold true in all cases, as demonstrated for a practical example in section 3.11.2.

The critical angle is defined by $n = \cos\alpha_c$. By expanding the cosine to second order in the critical angle (which should be small), we obtain

$$\alpha_c = (2\delta)^{1/2} = \left(r_0\frac{\rho\lambda^2}{\pi}\right)^{1/2} \tag{3.101}$$

Critical Angle Calculations for Platinum

As an example, the critical angle for platinum is calculated in this section.

The atomic weight of platinum, W, is 195.078 g/mol, its atomic number $Z = 78$, and the mass density $\rho_m = 21.090$ g/cm^3. Hence, the density of electrons in platinum is

$$\rho = \frac{\rho_m Z N_A}{W} = 5.078 \times 10^{24}\mathrm{cm}^{-3} = 5.078\text{Å}^{-3} \tag{3.102}$$

where N_A is Avogadro's number (6.022×10^{23}).

For a Cu $K\alpha$ emission line, $\lambda = 1.54$ Å, so $\delta = 5.401 \times 10^{-5}$ by (3.100) and $\alpha_c = 1.04 \times 10^{-2}$ (radians) by (3.101). Note that $\delta \ll 1$ as claimed previously. This is true even for this extreme example of a high Z, high mass-density material.

3.11.3 Scattering and Reflectivity

There are some apparent disparities between the results of the CTR theory (section 3.11.1) and the classical Fresnel reflectivity (section 3.11.2). The former predicts Bragg peaks connected by crystal truncation rods. Given no adsorption and a truncated infinite crystal, these Bragg peaks are predicted to have infinite intensity. The Fresnel formulae have no Bragg peaks or truncation rods, and the intensity maximum saturates at unity below the critical angle.

The Fresnel treatment cannot predict Bragg peaks, because the scattering media is assumed to be a solid block of constant density. The CTR treatment assumes a perfect crystalline lattice. If we extend the CTR treatment to consider continuous, homogeneous media, then integrals will take the place of summations. The scattering amplitude is

$$A(\mathbf{q}) = \int d\mathbf{r}\ e^{-i\mathbf{q}\cdot\mathbf{r}}\rho(\mathbf{r})\ . \tag{3.103}$$

A semi-infinite block of material, truncated at $z = 0$, will have a density profile

$$\rho(z) = \rho_0 \Theta(z) \tag{3.104}$$

where $\Theta(z)$ is the Heaviside step function. Integrating by parts will not work, because $e^{\pm iq\infty}$ cannot be defined. However, following [37], we consider the sign function

$$S(x) \equiv \begin{cases} -1 & x < 0 \\ +1 & x > 0 \end{cases} \tag{3.105}$$

The Fourier transform of $S(x)$ can be found by considering the function $e^{-t|x|S(x)}$ and then taking the $t \to 0$ limit.

$$\int_{-\infty}^{\infty} dx\ e^{-iqx} e^{-t|x|S(x)} = -\int_{-\infty}^{0} dx\ e^{(t-iq)x} + \int_{0}^{\infty} dx\ e^{-(t+iq)x} \tag{3.106}$$

$$= -\frac{1}{t-iq} + \frac{1}{t+iq} \tag{3.107}$$

$$\longrightarrow_{t\to 0} \frac{2}{iq} \tag{3.108}$$

Since $\Theta(x) = \frac{1}{2}(S(x) + 1)$, and the Fourier transform of unity is a delta function, then Fourier transform of the step function $\Theta(x)$ is finally

$$\int dz\ e^{-iq_z z} \Theta(z) = \frac{1}{iq_z} + \frac{1}{2}\delta(q_z)\ . \tag{3.109}$$

Then the structure factor (and the intensity) will be proportional to $1/q_z^2$. The $\frac{1}{2}\delta(q_z)$ may seem unimportant. We can show that it is significant by proving a familiar result [126]. Noting that

$$\Theta(z) + \Theta(-z) = 1 \tag{3.110}$$

then

$$\begin{aligned}
\int_{-\infty}^{\infty} dz\ e^{-iq_z z} &= \int_{-\infty}^{\infty} dz\ e^{-iq_z z}\Theta(z) + \int_{-\infty}^{\infty} dz\ e^{-iq_z z}\Theta(-z) \\
&= \frac{1}{iq_z} + \frac{1}{2}\delta(q_z) + -\frac{1}{iq_z} + \frac{1}{2}\delta(q_z) \\
&= \delta(q_z) \qquad (3.111)
\end{aligned}$$

In fact, even without knowing (3.109), one can show just from (3.110) that if $F(q_z) \equiv \int_{-\infty}^{\infty} dz\ e^{-iq_z z}\Theta(z)$, then $F(q_z) + F(-q_z) = \delta(q_z)$.

The result $S(q_z) \propto 1/q_z^2$ can be obtained in two other ways. Taking the continuum limit $a \to 0$ of the semi-infinite structure factor (3.85) yields this directly. The second method is to follow [124] and consider the structure factor (3.31) again:

$$S(\mathbf{q}) = \frac{1}{N} \int_V d^3\mathbf{r}_1 \int_V d^3\mathbf{r}_2\ e^{-i\mathbf{q}\cdot(\mathbf{r}_1 - \mathbf{r}_2)}\ \langle \rho(\mathbf{r}_1)\rho(\mathbf{r}_2)\rangle \qquad (3.112)$$

Transforming these volume integrals to surface integrals,

$$S(\mathbf{q}) = \frac{1}{N}\ \frac{1}{(\mathbf{q}\cdot\hat{n})^2}\ \int_S (d\mathbf{S}_1 \cdot \hat{n})\ \int_S (d\mathbf{S}_2 \cdot \hat{n})\ e^{-i\mathbf{q}\cdot(\mathbf{r}_1 - \mathbf{r}_2)}\ \langle \rho(\mathbf{r}_1)\rho(\mathbf{r}_2)\rangle \qquad (3.113)$$

where $d\mathbf{S}_1$, $d\mathbf{S}_2$ are differential surface vectors constrained to lie along the surface. The choice of unit vector $\hat{n}$ is arbitrary. If we take $\hat{n} = \hat{z}$, then

$$S(\mathbf{q}) = \frac{1}{N}\ \frac{1}{q_z^2}\ \int_S dx_1\ dy_1\ \int_S dx_2\ dy_2\ e^{-i\mathbf{q}\cdot(\mathbf{r}_1 - \mathbf{r}_2)}\ \langle \rho(\mathbf{r}_1)\rho(\mathbf{r}_2)\rangle \qquad (3.114)$$

and S is a constant-z plane.

Throughout this chapter, I have implicitly used the "kinematic" theory, which assumes that the first Born approximation holds. Because x-rays interact very weakly with matter, the approximation is valid for most points in reciprocal space.

However, at Bragg points (where Bragg's Law is satisfied) and near the (000) reciprocal space point, the Born approximation breaks down. That is why the CTR treatment fails to predict the existence of the critical angle or the finite intensity for a semi-infinite crystal.

However, we can show the equivalence of the two approaches far from (000), in the large-α limit. Starting with (3.94), rewrite $\cos^2\alpha = 1 - \sin^2\alpha$. Since $n^2 - 1$ is very small, we can approximate the terms within the square roots by

$$\left[\sin^2\alpha + (n^2 - 1)\right]^{1/2} = \sin\alpha + \frac{n^2 - 1}{2\sin\alpha} \tag{3.115}$$

Then (3.94) becomes

$$\frac{E_r^{\perp}}{E_0} = \frac{n^2 - 1}{4\sin^2\alpha} \tag{3.116}$$

The reflectivity coefficient $R = \left|E_r^{\perp}/E_0\right|^2$ is proportional to $1/\sin^4\alpha$. Since $q_z = 2k\sin\alpha$ from (3.29), $R \propto 1/q_z^4$. The CTR intensity falls with $1/q_z^2$, however. This apparent contradiction can be resolved by comparing the definitions of the reflectivity coefficient R and the differential cross-section $d\sigma/d\Omega$. The reflectivity coefficient considers the total "reflected" energy and the total incident flux. In contrast, the differential cross section is normalized by the incident flux (proportional to $1/\sin\alpha$) scattered into a unit solid angle (also proportional to $1/\sin\alpha$). When these factors are taken into account, $d\sigma/d\Omega = R\sin^2\alpha$.

To incorporate the Fresnel coefficients into simple kinematic x-ray scattering, multiply each amplitude, both incoming and outgoing, by E_t/E_0 as in (3.95) or (3.93). Because n is so close to unity, it hardly matters which polarization is assumed. From (3.29), $q_z = 2k\sin\alpha$ and then defining $(q_z)_c = 2k\sin\alpha_c$, we can simplify (3.93) to be

$$\frac{E_t^{\perp}}{E_0} = \frac{2}{1 + \sqrt{1 - ((q_z)_c/q_z)^2}} \tag{3.117}$$

For $\alpha < \alpha_c$, in addition to total external reflection, we also have the simplification that $\frac{E_t^{\perp}}{E_0} = 2\sin\alpha/\sin\alpha_c$. So the scattering amplitude will be multiplied by $\frac{E_t^{\perp}}{E_0}(\alpha)$ and $\frac{E_t^{\perp}}{E_0}(\beta)$. These transmission factors are often neglected except near the critical angle α_c, because they factor approach unity quickly as $\alpha > \alpha_c$ increases (see figure 3.8a).

Chapter 4

Experimental Procedures and Apparatus

4.1 Introduction

In this chapter, the specific procedures and apparatus used in these experiments are documented. First, the sample preparation protocol is described. The next section details the electrochemical apparatus and procedures. The following section describes the x-ray scattering apparatus, and the timing apparatus is discussed thereafter. Finally, suggestions for future improvements are made.

4.2 Sample Preparation

4.2.1 Procurement

Samples (nominally Pt(111)) were obtained from the Materials Science Center growth facility in Bard Hall. These samples were oriented through Laue back reflection, and then cut to the desired orientation by electrical discharge. Then, they were polished with SiC paper and Al_2O_3 powder down to a grit size of 0.25μm until a mirror-like surface was obtained.

In principle, this procedure should produce crystals with well-oriented faces. To allow large terraces to form on metal crystals, it is desirable to reduce the *miscut angle* between the crystallographic axis (*e.g.*, (111)) and the surface normal. However, miscut angles as large as $2°$ were measured in our lab by a combination of laser reflection and high-resolution Bragg diffraction. These can be traced to the Materials Science Center crystal mounting apparatus, which was insufficiently rigid to ensure a miscut smaller than a few degrees.

4.2.2 Miscut Calculation

In this section, the angle $\theta = (2\theta)/2$ is the Bragg diffraction angle, while ϕ is a rotation angle about the surface normal. On a *miscut* crystal, the Bragg diffraction peak will not be coincident with the surface normal. The angle between them is defined to be γ.

The surface normal was aligned with the ϕ axis as follows. By reflecting a laser beam from the mirror-like face of the crystal, a tight spot was cast onto a far wall or ceiling. Rotating the crystal about ϕ caused the laser beam to trace out a cone, causing the spot to trace out a corresponding ellipse on the wall. By adjusting the tilt stages on the sample goniometer, the ellipse could be narrowed until the spot did not move with ϕ. Then, the surface normal was well-aligned with the ϕ axis.

Moving the ϕ angle to some fiduciary value, such as 0°, the Bragg diffraction angle θ was recorded. Then, ϕ was set to 180° and a different θ was found. These two angles differ because the diffraction peak traces out a cone, similarly to the laser beam. The projection of the miscut along this one axis is (see figure 4.1)

$$2\gamma_x = |\theta(\phi = 0°) - \theta(\phi = 180°)| \ . \tag{4.1}$$

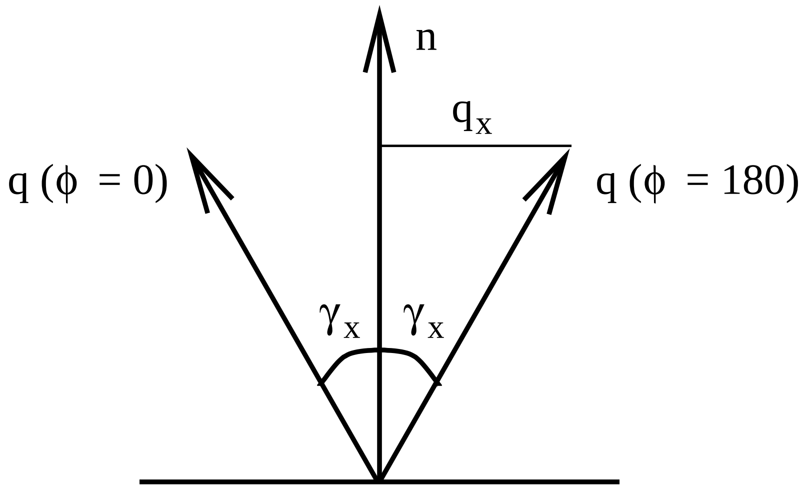

Figure 4.1: Determination of Miscut Angle

Likewise, by taking measurements at $\phi = 90°$ and $\phi = 270°$, the orthogonal projection of γ is measured,

$$2\gamma_y = |\theta(\phi = 90°) - \theta(\phi = 270°)| \ . \tag{4.2}$$

By inspection of q_x in figure 4.1, $q_x = q \sin\gamma_x$ (and $q_y = q \sin\gamma_y$), so the true miscut angle is found from

$$\sin\gamma^2 = \sin\gamma_x^2 + \sin\gamma_y^2\ . \tag{4.3}$$

4.2.3 Sample Preparation

After the miscut of each platinum crystal was measured, it was mounted onto the orienting/polishing apparatus shown in figure 4.2. The apparatus consists of a cylindrical barrel (E), with three dowels mounted on it (C). (Only two dowels are shown in the figure.) These form one half of the "kinematic mount"; the other half is a thick disk (B), into which the dowels press. Opposite the first dowel is a circular depression (G), opposite the second is a groove (H), and opposite the third is just the flat surface of the disk. One of the dowels is fixed; the other two can be raised and lowered my means of small adjustment screws running through the barrel. These permit the disk to be oriented by a few degrees in any direction with respect to the barrel axis. A long screw (D) attached to a spring and knurled knob (F) runs through the barrel axis and passes through the clearance hole (I). When tightened, the orientation is securely fixed. Finally, a mushroom-shaped tip (A) fastens to the kinematic disk (B) with three screws. The sample fits on to the end of this tip.

To prepare a sample, the tip of the apparatus was detached from the main body, and then placed on a hot plate. A crystal-bonding compound, liquid at high temperatures, was dabbed onto the tip before the platinum crystal was added. After cooling, the compound solidified to form a rigid, yet reversible, bond. The

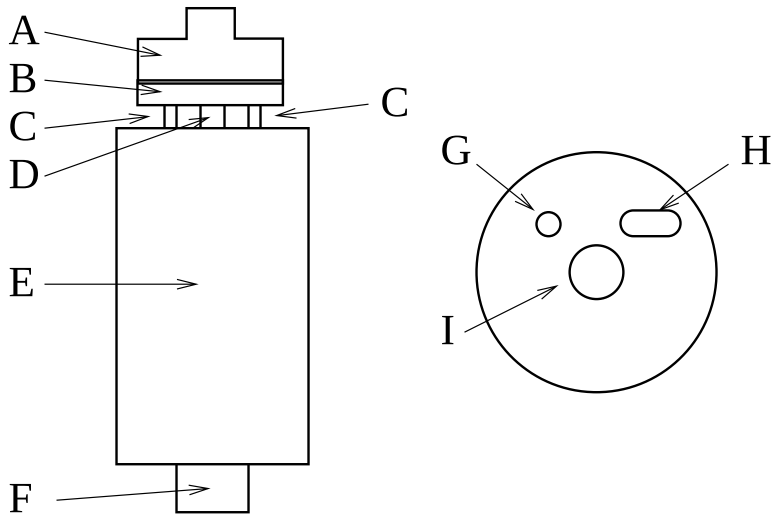

Figure 4.2: Diagram of orienting/polishing apparatus. (a) Side view. (b) Bottom view of the stage (B), showing the kinematic mount. Labels are described in the text.

tip was secured to the apparatus, and placed at the center of a rotation of a four-circle diffractometer. The orientation screws were adjusted until the (111) Bragg diffraction peak was constant in θ for any rotation ϕ about the barrel axis. When this was attained, the locking thumb screw was secured and the entire barrel was placed within the polishing sleeve. The great advantage of this apparatus is that it can orient the sample face to high precision, lock in that orientation, and then polish without loss of precision.

Polishing took place on a polishing wheel (Ecomet 4) run at the slowest speed (50 revolutions per minute). Each polishing step took 15 minutes, and the sample was thoroughly cleaned with water between steps. The polish began with sandpaper (Buehler 600 grit Carbimet paper discs #30-5112-600) and then successively finer (6μm, 3μm, 1μm, 0.25μm) diamond powder (Struers DP-Spray, P) on a nylon cloth (Buehler #40-7072) with some lubricant (Struers DP Lubricant Blue, HQ or Struers DP Lubricant Red, HQ). At the end of this process, a mirror finish was invariably obtained.

Thereafter, the tip was unscrewed from the apparatus and warmed on the hot plate to remove the sample. The sample was then immersed in hot nitric acid for at least four hours. This was done to remove any remaining contaminants, particularly polishing powder. Also, even the smallest powder size (0.25μm) is extremely large on the length scales that x-rays probe. To remove strain and small grooves in the crystal surface, it was annealed in a gas flame (available on tap in Clark Hall) for at least one hour. Finally, the sample was characterized and the miscut calculated as described above.

Figure 4.3 demonstrates the dramatic improvement that can take place after a sample is annealed. This sample was annealed for one hour with a propane torch. For comparison, both intensities have been normalized to yield a peak value of unity. Without this, the post-annealing peak would dwarf the pre-annealing peak. The true peak intensities differ by a factor of 23. The full-width at half-maximum was $0.60°$ before annealing and $0.032°$ after annealing, a factor of 19.

After several iterations of this orienting-polishing-annealing procedure, the bulk mosaic of the platinum crystal was $\approx 0.018°$ (full-width at half-maximum) and the surface normal was oriented to within $0.027°$ of the (111) direction. Empirically, we have found that both the mosaic and the miscut must be small in order to observe the incommensurate overlayer. Furthermore, a high quality substrate enhances the quality of voltammetric profiles. The development of this procedure was crucial to the success of this experiment. It has also propagated to other groups (Cooper, Ho) in Clark Hall, and has enabled them to improve surface quality and signal-to-noise ratios in their own data.

4.3 Electrochemical Apparatus and Procedures

4.3.1 Solutions

Most of the solutions were prepared by Lisa Buller, and the following paragraph is paraphrased from her dissertation [52].

All solutions were prepared using water purified by a Hydro purification train and a Millipore Milli-Q system. The ionic salts were used as received and always the

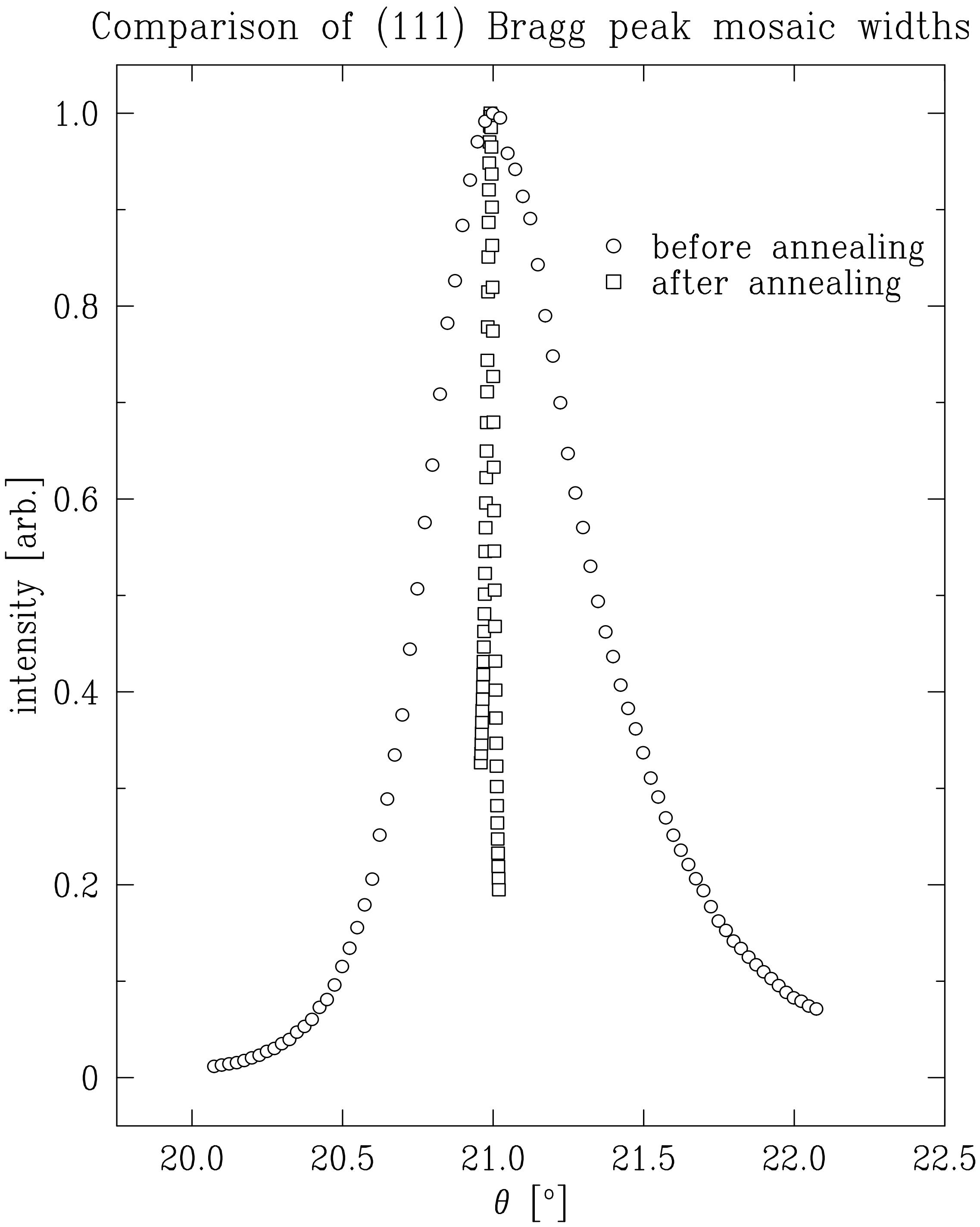

Figure 4.3: Mosaic scans, before and after annealing, normalized to unit peak height.

purest available. Perchloric acid solutions were prepared by dissolving either CuO (99.999%, Aldrich) or $CuCl_2$ (99.999%, Aldrich) in Ultrex perchloric acid. The addition of chloride anions was achieved through the addition of $CuCl_2$ or NaCl (99.999%, Aldrich). All solutions were bubbled for at least 15 minutes with pre-purified nitrogen, which was further purified by passage through oxygen-absorbing (MG Industries Oxisorb) and hydrocarbon (Fisher Scientific Activated Carbon 6-14 Mesh) traps to remove all traces of oxygen.

4.3.2 Three-electrode Electrochemical Cells

A typical well-designed electrochemical cell has three electrodes [118, 43, 44]. The guiding principle is to have all the interesting behavior occur at the *working* electrode. The other electrodes should be relatively inert and not complicate the analysis of the processes that occur at the working electrode. All potentials must be measured relative to some other reference value, which is provided by the *reference* electrode. The perfect reference electrode would be "ideally nonpolarizable". That is, its potential remains constant, regardless of the amount of current passing through it. Another purpose of the reference electrode is to ensure that an applied potential change does what we expect. Suppose we change the voltage of the potentiostat by ΔV. How do we know that this causes a ΔV at the working electrode and that part of the ΔV does not go into the reference electrode? If the reference electrode is ideally nonpolarizable, it maintains the same potential value, and the full ΔV is effected at the working electrode interface.

The *counter* (or *auxiliary*) electrode assists in this process. If the reference electrode is passing a significant amount of current, then the assumption of ideal non-polariziability is sorely tested. It is preferable to have an alternate, low-resistance, pathway through which most of the current flows. Counter electrodes are often composed of inert metals and have large surface areas to minimize their overall resistance.

The various electrodes used in our experiments are shown in figure 4.4. The large (10 mm) electrodes used for the simultaneous *in situ* x-ray and electrochemical measurements are labeled by (a). The smaller (1-2 mm) "ball" electrodes, labeled by (b), were produced by members of the Abruña group. These were of excellent quality, and produced good electrochemical signals. However, they were too small and too difficult to orient to be of use in our x-ray measurements. A Ag/AgCl reference electrode is labeled by (c). These were constructed by Lisa Buller [52].

4.3.3 Hanging Meniscus Cell

For electrochemical experiments on single crystals, a hanging-meniscus cell is ideal. A wire is spot-welded to the sides of the crystal face, as in figure 4.4(a,b). The face of the crystal is then dipped into the solution compartment (see figure 4.5), and pulled upwards so that only a meniscus connects the sample with the bulk of the solution. The reference and counter electrodes are placed in another compartment, connected by a frit (partially fused glass).

The advantage of this arrangement is that only the crystal face of interest in contact with the solution. Also, it is easy to use small (a few mm diameter) crystals, which are often better quality than large (10 mm diameter) crystals. The

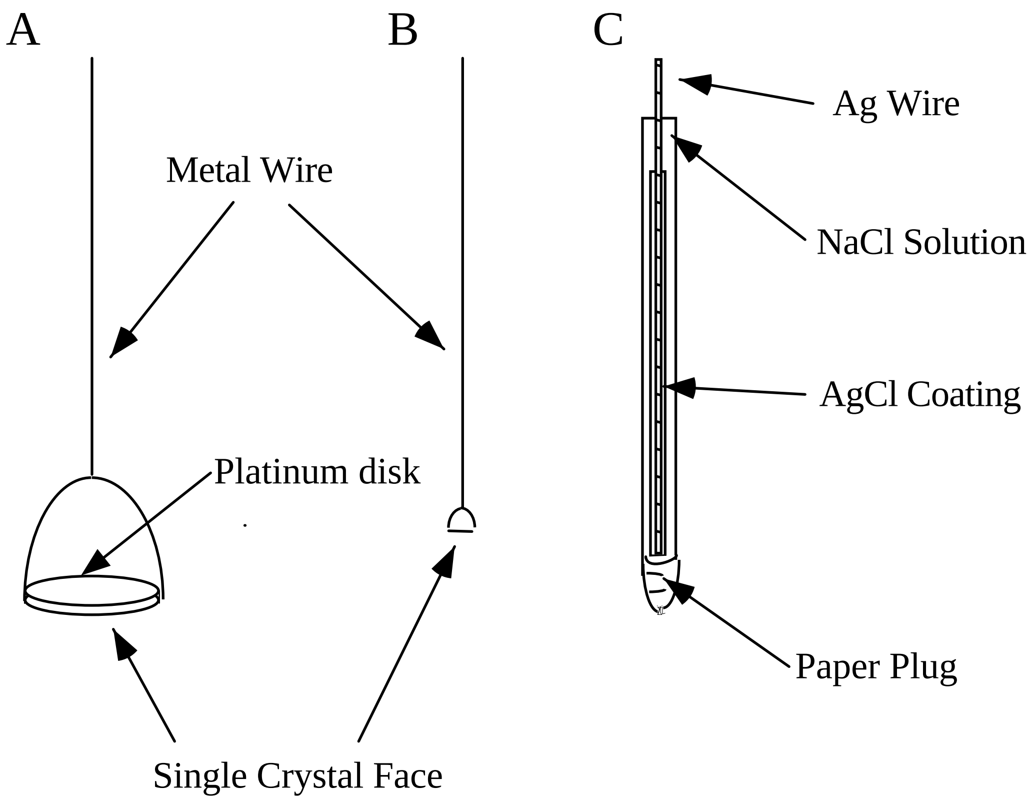

Figure 4.4: Electrodes used for the electrochemical measurements. (A) 10 mm diameter electrode. (B) 1-2 mm diameter electrode. (C) Ag/AgCl saturated-NaCl reference electrode.

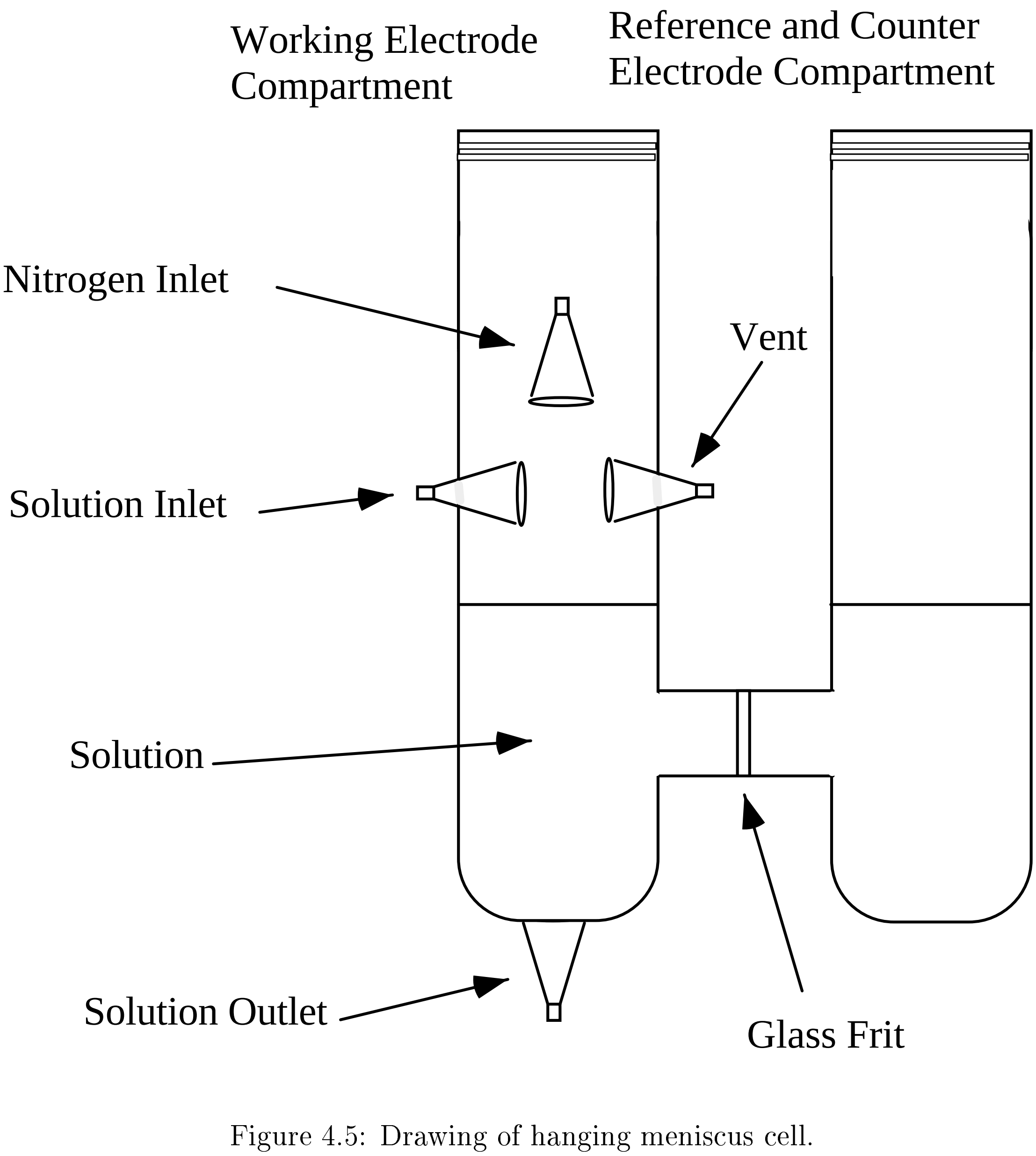

Figure 4.5: Drawing of hanging meniscus cell.

disadvantage is that the cell must remain in a fixed vertical configuration; this requirement is incompatible with most x-ray diffractometers. We used this cell only for voltammetric and current transient measurements.

4.3.4 *In Situ* X-ray cell

To perform simultaneous electrochemical and x-ray measurements, we constructed a cell similar to the one developed by Toney and coworkers [113]. This is a reflection-geometry cell, as shown in figure 4.6. The entire sample is immersed in solution, unlike the hanging-meniscus cell. The solution is contained by $6\mu m$ polypropylene film, held in place by an O-ring.

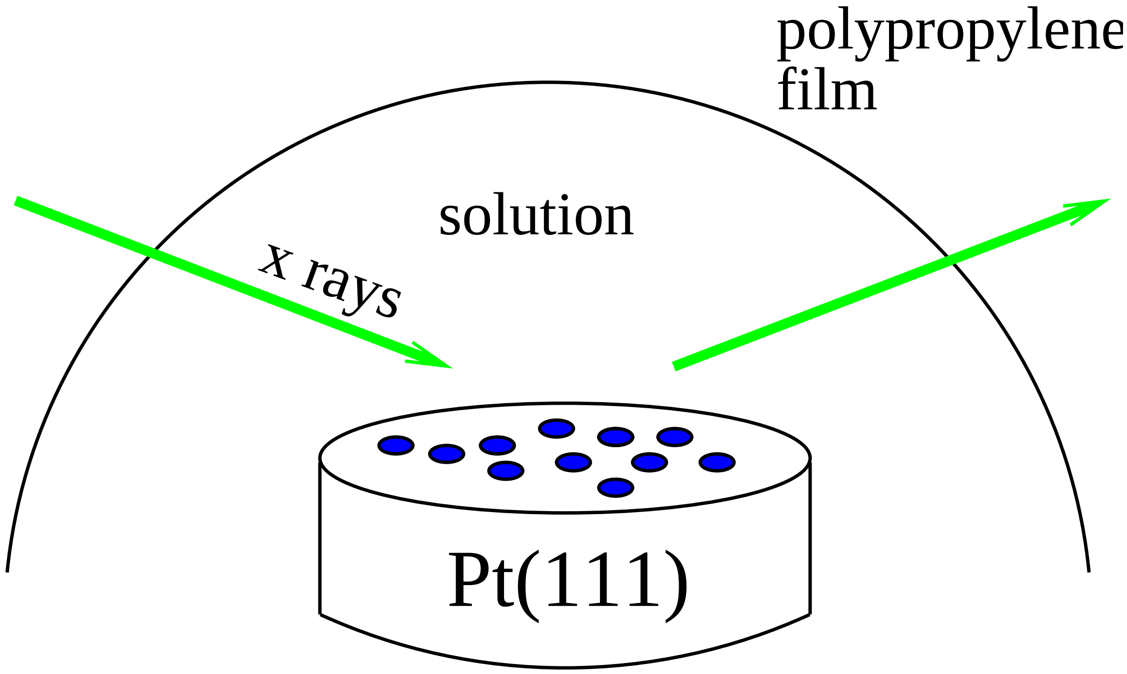

Figure 4.6: Cartoon of *in situ* electrochemical x-ray cell.

A detailed illustration of the cell is provided by figure 4.7. The majority of the cell is Teflon (Kel-F is an alternative material with greater strength). The sample is placed in the center and held in place by two non-circular Kel-F screws that squeeze the sample laterally. The sample and screws are raised with respect to a trough, where most of the solution resides. The reference electrode is inserted from the side. The counter electrode is a platinum wire that circumnavigates the trough several times.

Absorption

The x-ray reflection geometry places a limit on the *in situ* x-ray cell. The polypropylene film is extremely thin, and while contributing to the diffuse x-ray scattering background, does not We must incorporate the absorption of x-rays due to the layer of solution that is covering the sample.

Consider an adsorbing layer of thickness l and attenuation per unit length μ. From figure 4.8, the total path length of x-rays through the solution layer will be $x = l\sin\alpha + l\sin\beta$, where α is the angle of incidence, and β is the angle of reflection. For grazing incidence (small α), l is limited by the horizontal dimensions of the sample. In the specular ($\alpha = \beta$) case, we have $x = 2l\sin\alpha$.

From the relation $q_z = \frac{4\pi}{\lambda}\sin\alpha$ (3.30) and the absorption relation for the intensity $I = I_0 e^{-\mu x}$ (3.48), then

$$I = I_0 \exp\left(-\frac{l\lambda}{2\pi}\mu q_z\right) \ . \tag{4.4}$$

For aqueous solutions, the absorption coefficient can be calculated from (3.49):

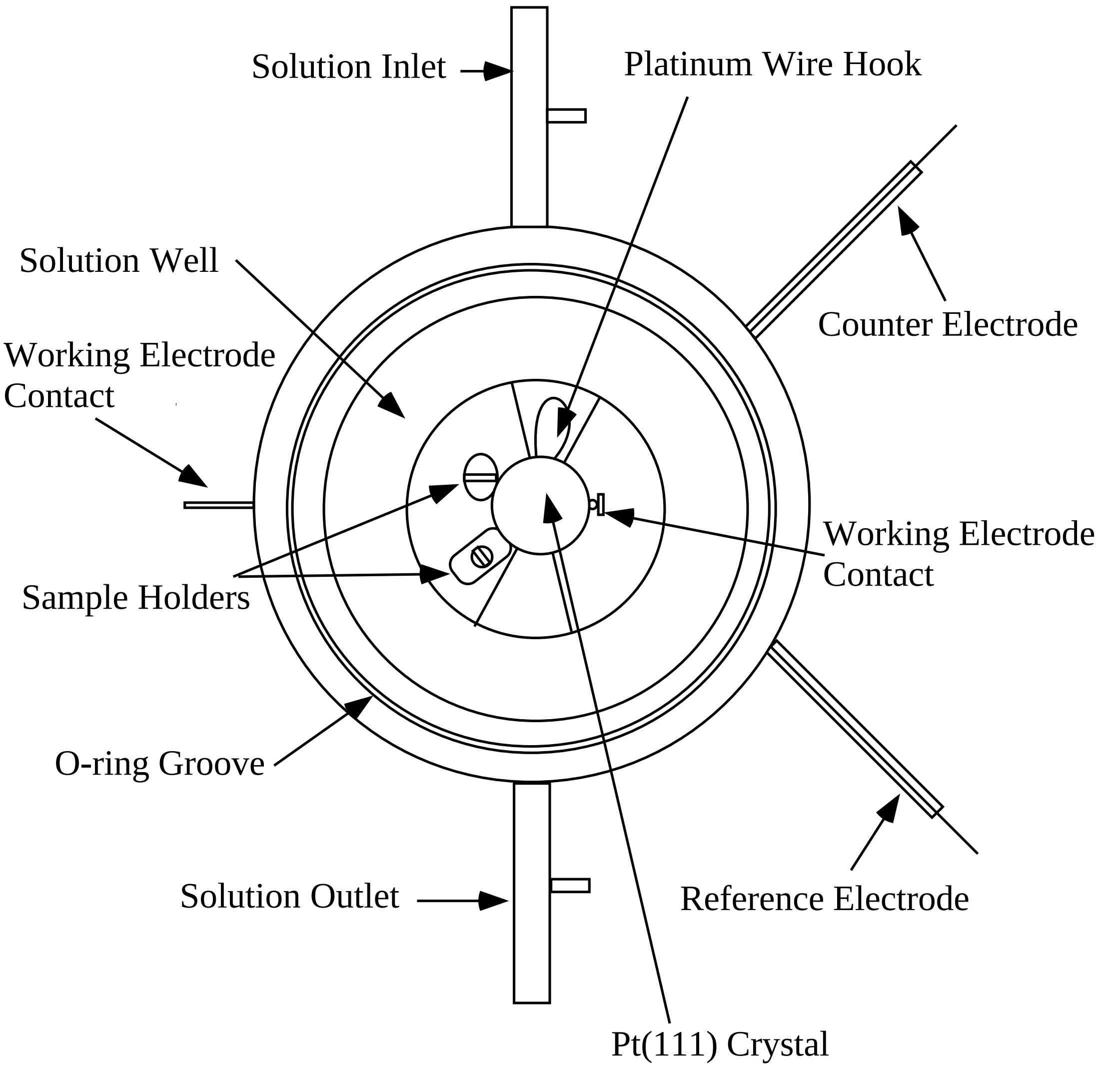

Figure 4.7: Detailed plans for the *in situ* electrochemical x-ray cell, prepared by Lisa Buller [52].

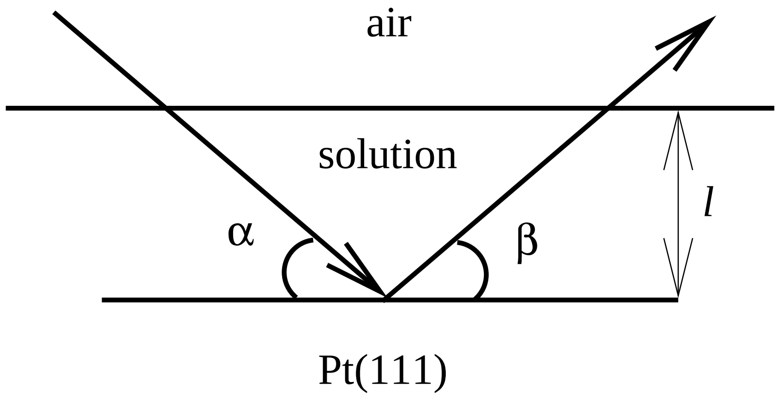

Figure 4.8: Absorption through a layer of thickness l, given incident angle α and reflected angle β.

$\mu = 9.848$ cm^{-1} for Cu Kα radiation ($\lambda = 1.542$Å) and $\mu = 1.061$ cm^{-1} for Mo Kα radiation ($\lambda = 0.711$Å). The $1/e$ absorption length is 1.0 mm for Kα and 0.942 cm for Mo Kα. Clearly, using high energy x-rays greatly reduces the problem of absorption.

For an typical $L = 1.5$, $q_z = 1.387$Å and $\lambda = 1.542$Å, even $l = 1$mm of solution causes an attenuation of 40%. It is therefore important to remove as much solution from the cell as possible, while still leaving enough to maintain good electrical contact between the face of the working electrode and the other two electrodes.

4.3.5 Potentiostat

A potentiostat is an instrument to keep the sample under potential (voltage) control and monitors the current. (A galvanostat, in contrast, keeps the sample under current control and monitors the voltage.) The simplest possible potentiostat circuit for a three-electrode configuration is shown in figure 4.9.

The operational amplifier will supply sufficient current to keep the reference electrode at a potential $-V$ with respect to ground (or the working electrode). Significant current will pass from the counter into the working electrode, but very little will pass through the reference electrode. This is in accordance with section 4.3.2.

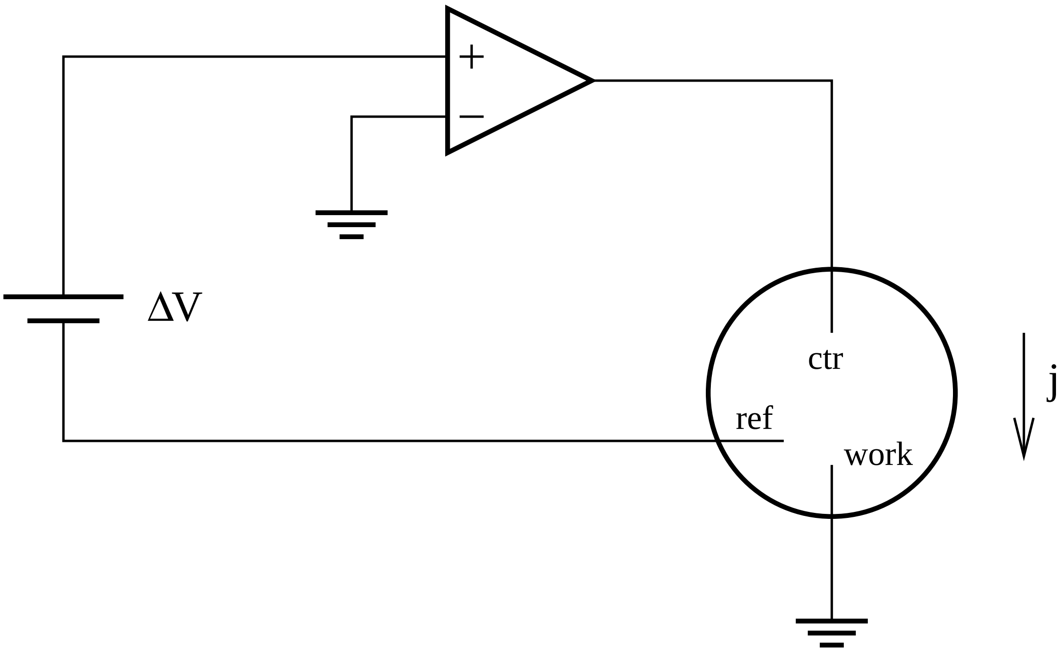

Figure 4.9: Simple potentiostat circuit for a three-electrode electrochemical cell. Adapted from [21].

The PAR 283 (Princeton Applied Research, Model 283) is a versatile instrument, which can be run as either a potentiostat or a galvanostat. It accepts commands over a GPIB (IEEE-488) interface, and has its own sophisticated, if unique, command language. During most experimental runs, we used the PAR 283 to acquire either cyclic voltammograms (described in section 5.2) or chronoamperometric transients. Cyclic voltammograms were taken of each sample while the solution layer was extended, when the solution was pulled out, and at various points during the experimental run on a given sample.

4.3.6 Safety

In a dilute (0.1 M) form, perchloric acid poses a minor health hazard. Contact with skin is mildly irritating, and should be rinsed off as soon as possible. Contact with the eye is more serious. For this reason, splash goggles should be worn at all times. In case of a large spill, sodium bicarbonate should be available for neutralization.

The platinum sample glows yellow-white during annealing. There is a significant ultraviolet spectral component, and the sample needs to be kept under continual supervision. To prevent permanent retinal damage, ultraviolet-resistant goggles must be worn during this process.

4.3.7 Sample Treatment

Before a sample is inserted into the x-ray cell, a careful protocol must be observed. UPD is extremely sensitive to chemical contaminants, especially metallic and organic ones.

- Spot-weld a clean platinum to the side of the sample, if not already present.
- Clean the top of the cell with solution; it should bead over everything. Then drain it away.

- Rinse the cooling cell with solution at least three times, draining with forced nitrogen.
- Have nitrogen flowing into the cooling cell.
- Flow solution into the cell, allowing a bubble to form on top of the cell.
- Put the hood (which should have nitrogen flowing through it) over the cell.
- Wear goggles to prevent retina burn.
- Anneal for 8 minutes the first time, 5 minutes each subsequent time.
- Cool in cooling cell for 4 minutes (under nitrogen overpressure).
- Flow solution into the cooling cell; fill to the level of the input port. Immerse the sample for at least one minute; a longer period is acceptable.
- The platinum surface will oxidize very quickly. The next step must be done *very quickly*!
- Remove the sample from the cooling cell and transfer it to the x-ray cell. To buy time, it is often helpful to squirt some solution or (deoxygenated) water on the face.
- Tighten Kel-F screw to fix sample in place.
- Cover with polypropylene film, which should be pre-rinsed. Cover with the O–ring and metal sleeve. Screw down the four jeweler screws evenly, for even pressure along the O–ring.

- The rest potential (no external potential applied) should be near 650 mV.
- With solution layer extended, run a cyclic voltammogram from 650 mV to 200 mV at 5 mV/s.
- With a syringe, pull out most of the solution and run an identical cyclic voltammogram.

The cooling cell used in the previous procedure is shown in figure 4.10. The Pt(111) sample is shown hanging from its hook. During operation, nitrogen is kept flowing through the cell. Solution is drained from the bottom outlet, and introduced from either of the upper inlets.

4.4 X-ray Apparatus

X-ray scattering is a nearly ideal probe of the ordering kinetics of the two-dimensional overlayers found in UPD systems. Unlike electrons or neutrons, X-rays can penetrate through a thin solution layer, allowing the experiments to be performed *in situ.* X-rays provide structural information on atomic length scales without perturbing the system with mechanical probes or large fields, as scanning probe microscopes may. Finally, the extremely high flux from a modern synchrotron x-ray source, such as the National Synchrotron Light Source (NSLS), permits the weak diffraction signal from a single Cu–Cl bilayer to be studied at high resolution.

In our experiments, the white beam produced by a bend magnet on the NSLS electron storage ring was focused in both transverse directions by a total external

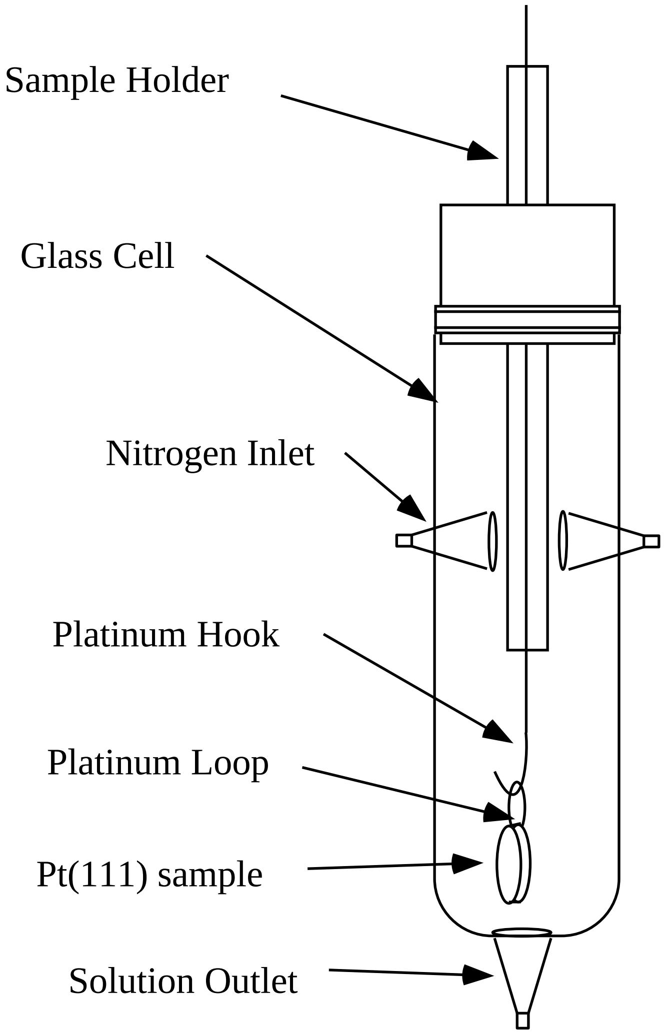

Figure 4.10: Drawing of cooling cell.

reflection mirror. A monochromator consisting of two Ge(111) crystals was configured to select 8.80 keV x-rays. The substrate was placed in a thin film geometry x-ray cell similar to those used by Toney and coworkers [113]. The cell was placed at the center of rotation of an Eulerian cradle and two pairs of XY-slits between the sample and the detector determined the resolution of the scattered x-rays. The resolution is discussed in detail in section 5.5.

In the lab, x-rays were produced by a Rigaku (Model RU200) rotating Cu anode source. The Cu Kα_1 was selected by means of either a single or triple-bounce Si(111) monochromator. Although the instrument can provide a 60 kV accelerating voltage and 200 mA filament current, the lowest power setting (20 kV, 10 mA) was usually sufficient for sample orientation.

To detect x-rays we used an integrated NaI scintillation crystal, photomultiplier, and preamplifier (Bicron 1XMP 040B-X). The resulting electrical signal was sent through a combined amplifier and pulse-height analyzer (Canberra Model 1718) for broad energy discrimination. The TTL pulses were then sent to a simple adding memory module (Kinetic Systems 3610 Hex Counter) that also received timing pulses from another module (Kinetic Systems 3655 Timing Generator).

In the lab, the signals were then acquired by a data acquisition card (DSP 6001). At the NSLS, data acquisition was handled by a CAMAC to SCSI interface module. In both places, the four-circle diffractometer (Huber) was under the control of a sophisticated software package ("spec", by Certified Scientific Software) running on an Intel 486-based computer.

4.5 Time-Resolved Measurements

Time-resolved x-ray measurements can be accomplished in several ways.

For instance, Bergmann *et al.* [32] used the timing of the electron bunches around the synchrotron ring for Mössbauer experiments. This is ideal for extremely short time ranges. Very recently, Knight *et al.* [88] have demonstrated a prototype device etched onto a silicon wafer to study protein folding. This works by mixing two jets together (for instance, folded protein and a denaturing agent) and squirting the product through a long channel. Because the flow is lamellar, the mixing occurs by diffusion. Because the fluid volumes are extremely low (nanoliters), the diffusive length scale is extremely short, and the mixing time is on the order of microseconds. By moving the device along the x-ray beam, different times after the mixing event are examined. In this way, position and time are coupled.

In contrast, our method relies upon timing electronics to separate the x-ray signal into various time bins. This "stroboscopic" method was first used by our group to study charge-density wave kinetics [127]. Although the PAR 283 claims to have a trigger, it does not operate in the standard sense of the term. Normally, when an instrument (an oscilloscope, for example) is waiting for an electronic trigger, operation ceases until the trigger is detected. Then, the other operations are begun or resumed. Instead, the PAR 283 performs a variety of operations, periodically polling the input to see if the trigger signal has arrived. Only then is the specified series of actions initiated. This can lead to an unpredictable delay between the trigger input and the initiation of commands by the PAR 283. For this reason, it was decided to have the PAR 283 be the master controller and send trigger signals to the other instruments.

The control diagram is shown in figure 4.11. The potentiostat applies a voltage to the sample and continuously reads current from it. At the beginning of a voltage cycle, it sends a trigger pulse to the waveform generator (Keithley 3940 multifunction synthesizer). This sends a series of pulses to the multichannel scaling averager (DSP 2190), which consisted of a multichannel scaling module (DSP 2090) and a signal averaging memory (DSP 4101). These bin pulses both initiated the averaging memory and incremented the current memory location (time bin). These timing modules also received x-ray intensity data, which was added to the time bin. At the end of a series of voltage cycles, the memory was dumped to the computer for display and analysis. The chronoamperometric traces (current vs. time) were digitized into 5000 time bins, and collected by the potentiostat. At the end of the voltage cycle, these were also sent to the computer.

4.6 Future Improvements

4.6.1 New Cell Design

With the advent of high-energy synchrotron sources, x-ray cell geometries with a thick solution layer have become feasible. Brossard *et al.* [49] describe a cell very similar to ours, but without the thin solution layer constraints. The cyclic voltammetry measurements they present are not high quality; presumably, this is a function of sample preparation, and not the cell itself.

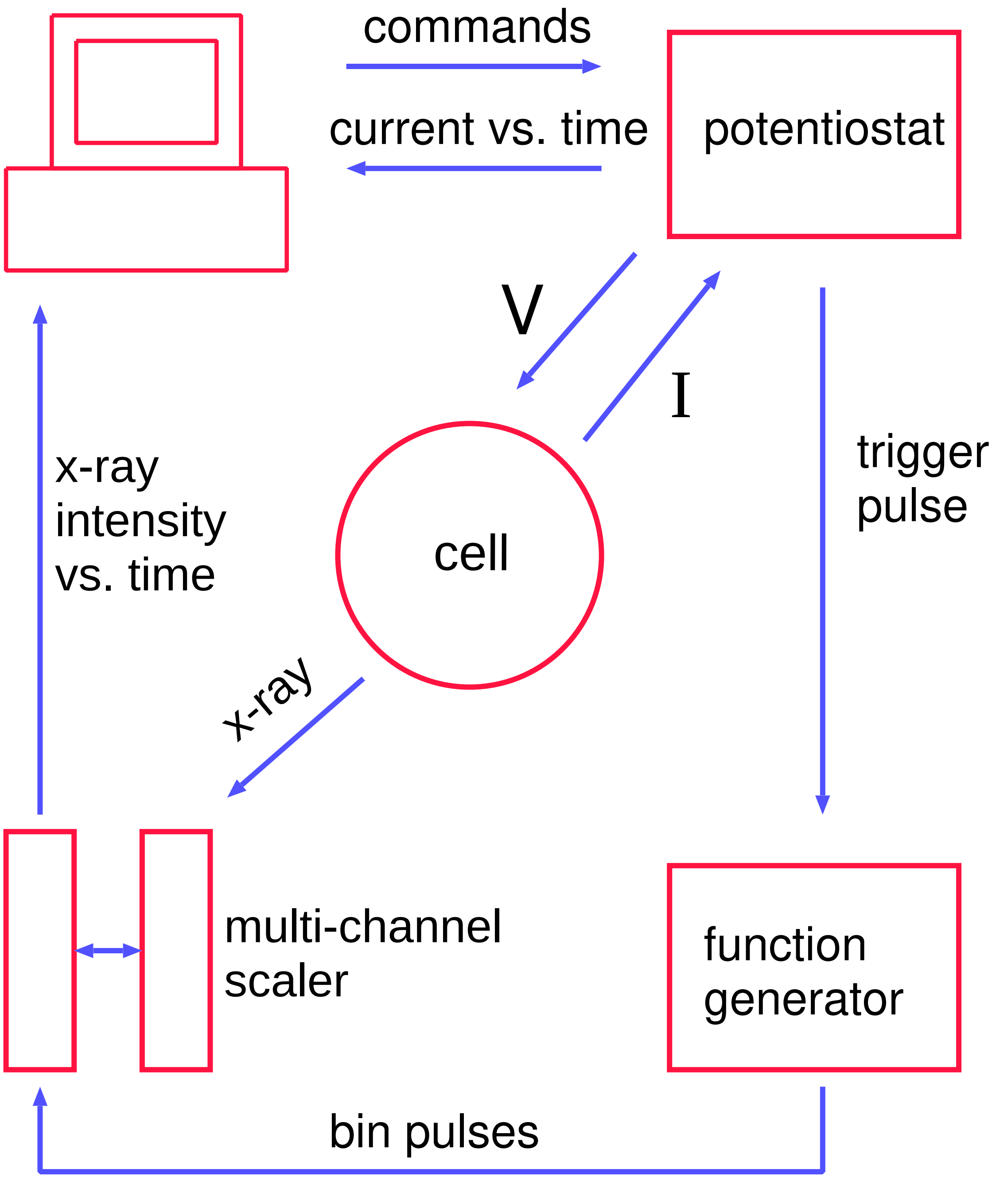

Figure 4.11: Instrumentation for timing experiments.

4.6.2 Improved Sample Quality

As discussed in section 4.2.1, these crystals were not ideal. The simplest course would be to procure samples from a reliable external source. If annealing is still necessary, a new method should be found. Heating with a torch sometimes produced cloudy spots in the center of the sample, where the flame was hottest. A more even annealing could be done in ultra-high vacuum and by attaching it to a heating stage.

4.6.3 Area (or Linear) Detectors

In our experiment, the highest resolution (section 5.5) was obtained by rotating the sample about the surface normal. In this case, an area or linear detector would not be helpful. However, there may be cases in which the resolution is sufficient to simply have an area detector mounted on the end of the detector arm. A CCD (charge-coupled device) could be run in a mode such that each line is shifted down. In this case, all of the time-resolved data could be recorded on the device, which would speed up the data acquisition time by the number of $\mathbf{q}$-points.

4.6.4 Improved Electronics

In retrospect, the PAR 283 potentiostat was difficult to program, and not as flexible as anticipated. A superior solution would be to purchase the best possible analog potentiostat (BAS is an good choice) that accepts an external line voltage. Then buy a good programmable digital-to-analog card that can be programmed easily and has sufficient time resolution.

It may also be advantageous to replace CAMAC modules with cards within the computers. At the time of these experiments, we needed to maintain compatibility with equipment at CHESS and NSLS X20A. Now, the DSP timing modules could be replaced with a multichannel scalar card (Oxford MCS, for instance). The counter/timer modules could be replaced with an integrated counter/timer card (Keithley CTM-010). These particular upgrades are already underway for the new spectrometer being set up in the Brock group laboratory.

Chapter 5

Cyclic Voltammetry and Static X-ray Measurements

5.1 Introduction

This chapter begins the presentation of our data on the underpotential deposition (UPD) of Cu onto Pt(111) in the presence of Cl. The first section presents our cyclic voltammetry on this UPD system. Subsequent sections discuss the hexagonal coordinate system and the structure of the incommensurate UPD overlayer. Finally, our static x-ray measurements of this overlayer are presented.

5.2 Cyclic Voltammetry

Cyclic voltammetry, as the name suggests, is a measurement of the current while the voltage is being swept (usually linearly with time). The cyclic adjective refers to the fact that the voltage is swept in both directions. As a function of time, the applied voltage traces out a triangular wave (figure 5.1a).

Cyclic voltammetry is a commonly used technique in electrochemistry, with many different applications. The next section illustrates a simple example: the cyclic voltammogram from an adsorption / reduction reaction, where the adsorption follows a Langmuir isotherm. In our experiments, this technique provided information on the equilibrium phase diagram.

5.2.1 Cyclic Voltammetry for an Ideal System

This section follows the theory presented in section 2.8. It may be helpful to review that section before continuing.

As suggested by Bard and Faulkner [31], consider the reduction of species O at the electrode to form species R.

$$\mathrm{O} + ne^- \rightarrow \mathrm{R}\ . \tag{5.1}$$

We begin at a sufficiently positive potential such that all of the adsorbates are in the oxidized state (O). At $t = 0$, we sweep the potential negatively and monitor the current generated at the electrode. We want an expression for the current density $j(t)$ in terms of the voltage $\Delta V(t)$ and the (constant) sweep rate v. For reduction, we must sweep in the negative direction, so $d(\Delta V)/dt = -v$.

The current density comes from the reaction (5.1), so

$$j(t) = -ne\frac{d\Gamma_O}{dt} = nev\frac{d\Gamma_O}{d(\Delta V)}\ . \tag{5.2}$$

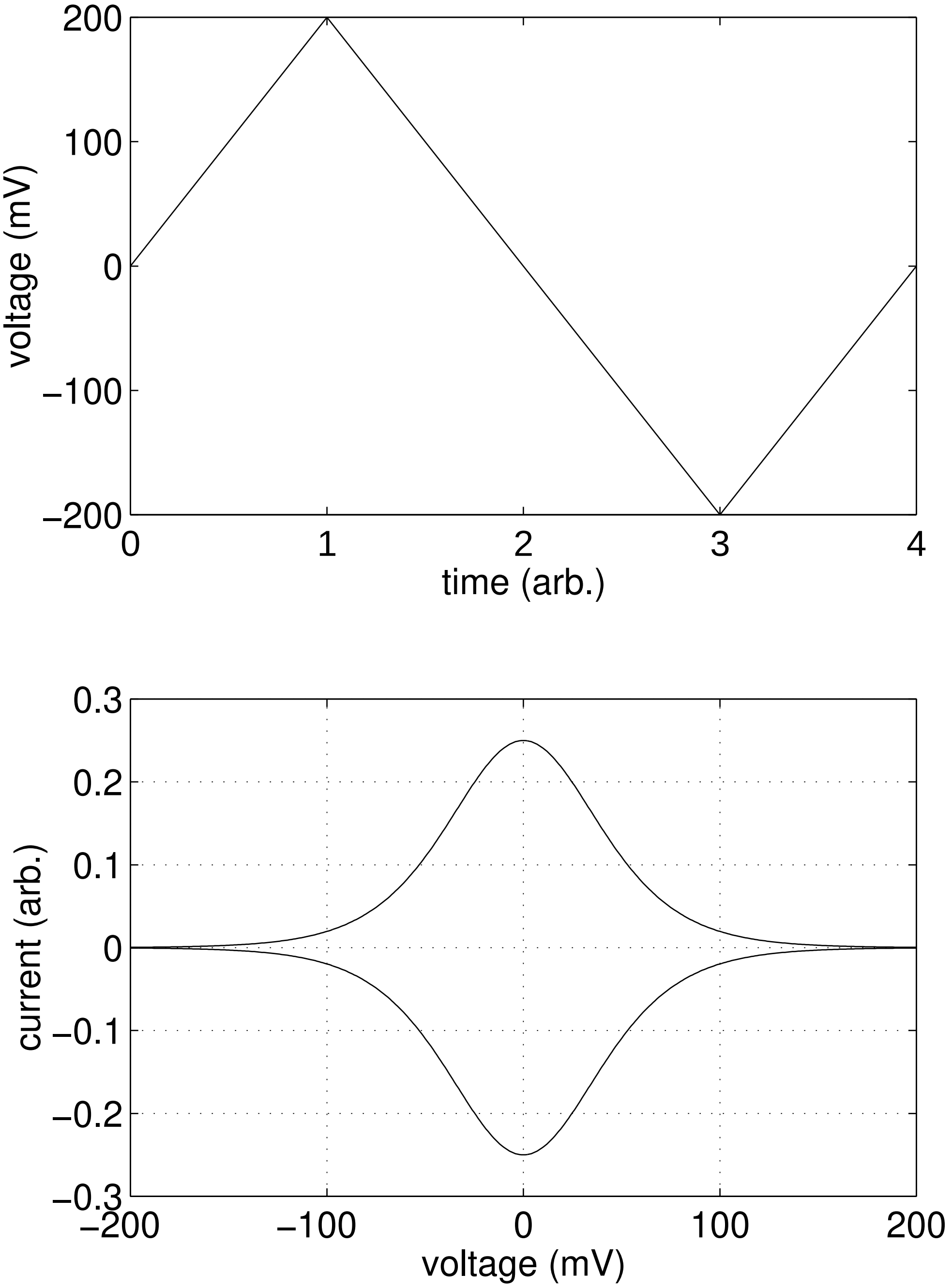

Figure 5.1: (a) Applied voltage waveform. (b) Current response for an ideal system.

To find an expression for $\Gamma_O(t)$, assume the reaction is completely reversible, so that the Nernst equation (2.41) applies:

$$\Delta V = \Delta V_0' - \frac{kT}{ne} \sum_i \nu_i \ln c_i \ . \tag{5.3}$$

In practice, this assumption means that the v must be very small in comparison with the reaction rate. Rewriting (5.3) to find the ratio of concentrations at the electrode surface,

$$\frac{c_O(z=0,t)}{c_R(z=0,t)} = \exp\left[\frac{ne}{kT}(\Delta V - \Delta V_0')\right] \ . \tag{5.4}$$

Assume there are no adsorbate–adsorbate interactions, except for the O $\rightarrow$ R reaction and the competitive filling of adsorption sites. If there were only one species on the electrode, then we would use the Langmuir isotherm (2.56)

$$\theta = \Gamma/\Gamma_{\text{sat}} = \frac{c\exp\left(-\frac{\Delta G}{kT}\right)}{1 + c\exp\left(-\frac{\Delta G}{kT}\right)} \ . \tag{5.5}$$

When there are two species, O and R, competing for adsorption, then this becomes

$$\theta_O = \Gamma_O/\Gamma_{O,\text{sat}} = \frac{c_O\exp\left(-\frac{\Delta G_O}{kT}\right)}{1 + c_O\exp\left(-\frac{\Delta G_O}{kT}\right) + c_R\exp\left(-\frac{\Delta G_R}{kT}\right)} \ . \tag{5.6}$$

So the ratio of surface excesses is

$$\frac{\Gamma_O}{\Gamma_R} = \frac{c_O\Gamma_{O,\text{sat}}\exp\left(-\frac{\Delta G_O}{kT}\right)}{c_R\Gamma_{R,\text{sat}}\exp\left(-\frac{\Delta G_R}{kT}\right)} = \frac{b_O c_O}{b_R c_R} \tag{5.7}$$

where the abbreviations b_O and b_R are introduced for simplicity. Combining (5.4) with (5.7) the ratio x is

$$x \equiv \frac{\Gamma_O}{\Gamma_R} = \frac{b_O}{b_R}\exp\left[\frac{ne}{kT}(\Delta V - \Delta V_0')\right] \ . \tag{5.8}$$

Since we assumed that $\Gamma_R(t=0)=0$, then $\Gamma_O(t)+\Gamma_R(t)=\Gamma_O(t=0)$ for all t. Then

$$\Gamma_O = \Gamma_O(t=0)\frac{x}{1+x} \tag{5.9}$$

and now taking the derivative

$$\frac{\partial \Gamma_O}{\partial(\Delta V)} = \Gamma_O(t=0)\frac{\partial x}{\partial(\Delta V)}\frac{x}{(1+x)^2}\ . \tag{5.10}$$

Substituting (5.10) into (5.2) and replacing x,

$$j = \frac{n^2e^2}{kT}v\Gamma(t=0)\frac{\frac{b_O}{b_R}\exp\left[\frac{ne}{kT}(\Delta V-\Delta V_0')\right]}{\left\{1+\frac{b_O}{b_R}\exp\left[\frac{ne}{kT}(\Delta V-\Delta V_0')\right]\right\}^2}\ . \tag{5.11}$$

Finally, we want to find the full-width at half-maximum. Start with the simplified function

$$y(x) = \frac{e^x}{(1+e^x)^2}\ . \tag{5.12}$$

We want to find x such that $y(x)=y(0)/2=1/8$. Substituting $z=e^x$ and solving the resulting quadratic equation $z^2-6z+1=0$ yields $z=3\pm\sqrt{8}$, or $x\approx\pm1.7627$ (which is symmetric about $x=0$, as expected). Thus the full width at half-maximum of (5.11) is approximately $3.5255\times kT/(ne)$, or about $90.6/n$ mV at 25°C.

5.2.2 Cyclic Voltammetry for Cu/Cl/Pt(111) UPD

The voltammetric profile is shown in figure 5.2. These data were collected in our x-ray scattering cell at 5 mV/s with 0.1 M $HClO_4$ as a supporting electrolyte, 1 mM Cu^{2+} and 10 mM Cl^-. The current response exhibits two sharp and well-defined voltammetric deposition peaks centered at about +0.47 and +0.32 V (vs. a Ag/AgCl reference electrode). Upon reversing the potential sweep, the current response then exhibits two sharp stripping peaks corresponding to the reverse reactions.

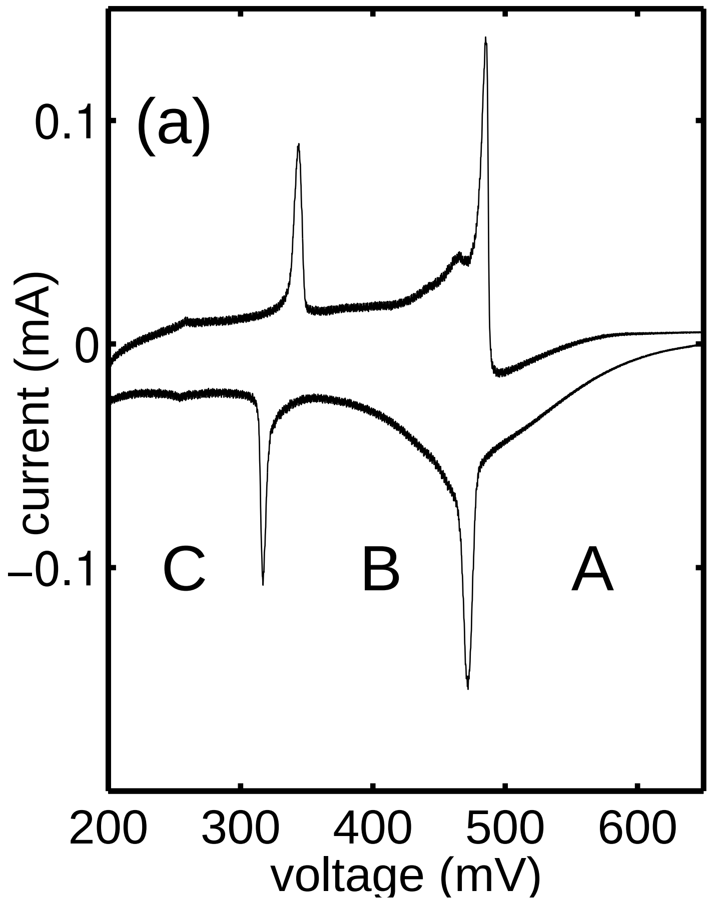

Figure 5.2: A cyclic voltammogram taken in the x-ray scattering cell at a sweep rate of 5 mV/s with 1 mM Cu^{2+} and 10 mM Cl^{-}, and 0.1 M $HClO_4$ as a supporting electrolyte.

A schematic of the deposition process is depicted in figure 5.3. The labels A, B, C in this figure also correspond to the potential regions in figure 5.2. At the rest potential (region A), chloride anions are adsorbed on the platinum surface in a non-ordered fashion [158, 108]. As the potential is swept negatively, copper is electrodeposited onto the platinum surface at a well-defined potential [90, 149, 94]. The electrodeposited copper and chloride ions together form an ordered Cu–Cl bilayer structure *incommensurate* [131] with the platinum surface (region B). If the potential is then moved further in the negative direction, there is further copper deposition, creating a full, *commensurate* copper monolayer (region C) [94, 90, 156, 157, 95, 72]. The copper monolayer is, in turn, believed to be covered by a disordered layer of chloride anions. On the reverse (positive-going) sweep the reverse processes take place; that is, some copper desorbs, forming the CuCl lattice structure (region B) and at more positive potentials the copper is completely stripped from the surface, leaving the disordered chloride anions adsorbed on the surface and returning the system to region A. The sharp voltammetric features seen in Figure 5.2 are the electrochemical signature of a clean and well-ordered surface.

In our experiments, we used cyclic voltammetry for three purposes. Most importantly, it served as a qualitative "fingerprint" of the UPD process itself. The cyclic voltammograms are extremely sensitive to contamination of the solution, poor quality of the single-crystal electrode surface, and dissolved oxygen in solution. Empirically, we found that obtaining a good cyclic voltammogram was a *necessary*, but not *sufficient*, condition to finding a well-ordered UPD layer with x-ray scattering.

Secondly, the width of the peaks tells us an important fact about this UPD process. As derived in section 5.2.1 and plotted in figure 5.1b, the full-width at half-maximum of the current peak should be close to $90.6/n$ mV at room temperature. The fact that our peaks are significantly smaller than this value implies that there

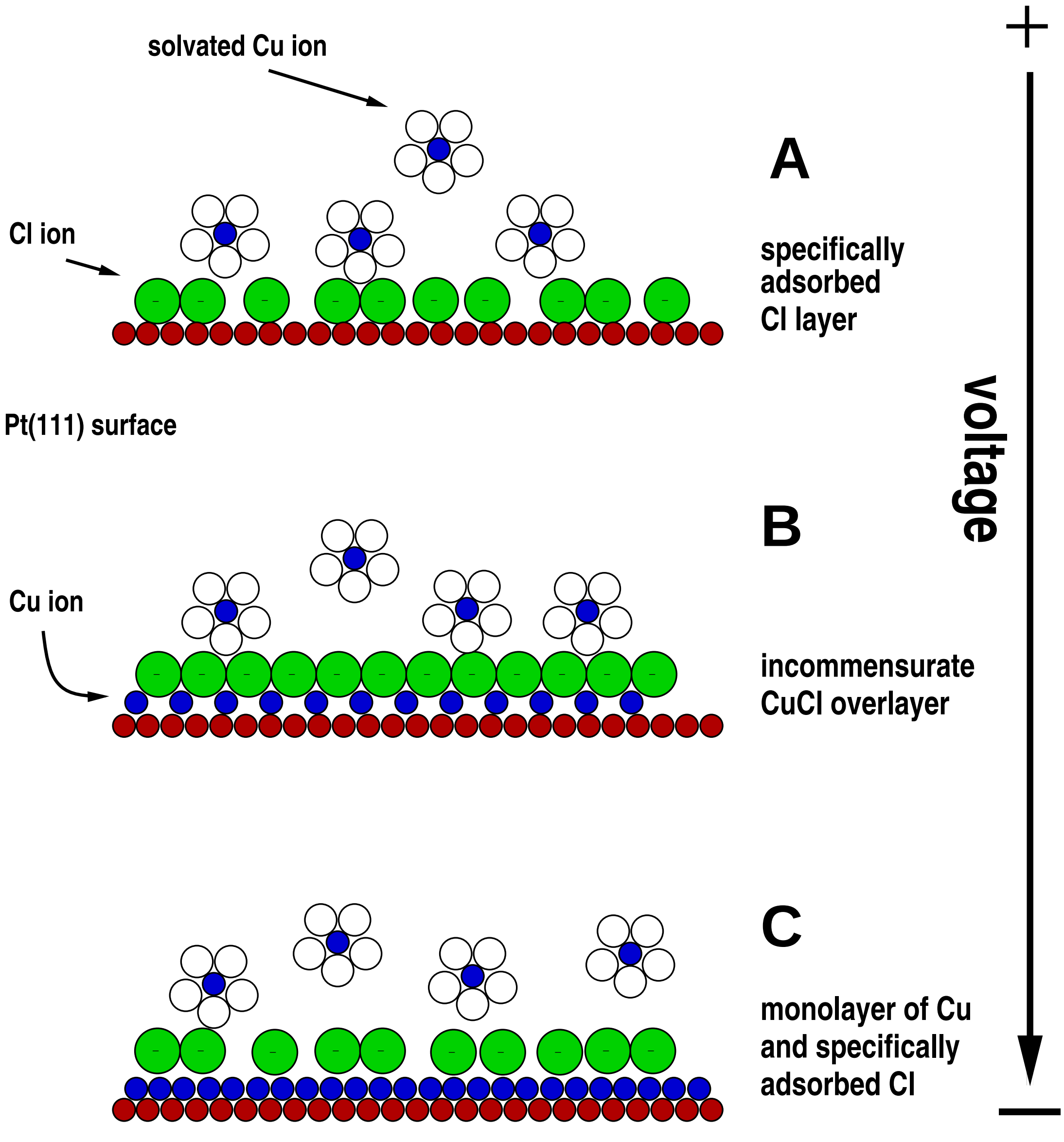

Figure 5.3: Cartoon of phases in the UPD of Cu on Pt(111) in the presence of Cl.

is significant interaction among the adsorbed ions in the UPD layer. In particular, once some ions are adsorbed/desorbed, this tends to enhance the probability that other ions will follow.

Thirdly, unlike figure 5.1b, the peak positions for the negative voltage sweep are displaced from their partners on the positive voltage sweep. This hysteresis, which is present even for very slow sweep rates (1 mV/s), is an indication that the system is kinetically limited. The reason for this, which had been unclear, is explained by our time-resolved data in chapter 6 in terms of a nucleation and growth model.

5.3 Hexagonal Coordinates

The remainder of this chapter concerns x-ray scattering from the platinum surface and the incommensurate CuCl overlayer. For cubic crystals, the basis vectors are usually defined to be mutually perpendicular and of equal length (like the x, y, and z Cartesian axes). When dealing with the (111) surface of a face-centered cubic lattice, however, it is convenient to redefine the basis vectors. The c axis is defined to be along the (111) surface normal. Because of the ABCABC... stacking, the reciprocal space (111) is mapped onto (003). The **a** and **b** real-space basis vectors, which lie in the plane of the surface, are shown in figure 5.4a. Because these basis vectors subtend 120°, these are often called "hexagonal surface units" [75]. The circles in the figure represent platinum atoms on the (111) surface. These real-space lattice sites are indexed in figure 5.5.

From the convention (3.64) that $\widehat{a}_i \cdot \widehat{q}_i = \delta_{ij}$, $\mathbf{b}^*$ is orthogonal to **a** and **c**, and

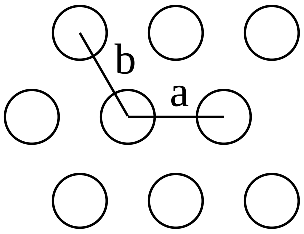

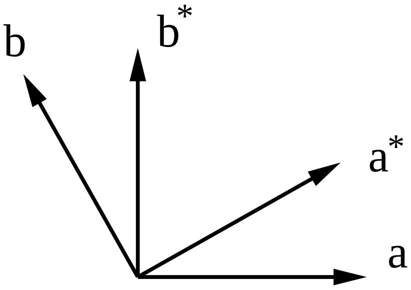

Figure 5.4: (a) The Pt(111) surface with surface lattice vectors $\mathbf{a}$, $\mathbf{b}$, which are perpendicular to $\mathbf{c} = (111)$. (b) Reciprocal lattice vectors corresponding to the unit cell chosen in (a); $\mathbf{a}^*$ and $\mathbf{b}^*$ subtend $60°$ and are perpendicular to $\mathbf{c}^*$.

$\mathbf{a}^*$ is orthogonal to $\mathbf{b}$ and $\mathbf{c}$. So $\mathbf{a}^*$ and $\mathbf{b}^*$ must point in the directions indicated in figure 5.4b. These vectors subtend $60°$ and generate a triangular lattice. The reciprocal-space lattice sites are indexed in figure 5.6. Although this figure appears superficially identical to figure 5.5, the indexing is different due to the different angles subtended by the basis vectors. From this point on, Bragg peaks are indexed using these hexagonal units.

The conversion from cubic to hexagonal units is easily accomplished. Writing both $\mathbf{q}$-vectors as column vectors, then the matrix product $\mathbf{q}_{\text{cubic}} = \mathbf{J}_{\mathbf{h}\to\mathbf{c}}\mathbf{q}_{\text{hexagonal}}$ and $\mathbf{q}_{\text{hexagonal}} = \mathbf{J}_{\mathbf{c}\to\mathbf{h}}\mathbf{q}_{\text{hexagonal}}$. These transformation matrices are

$$\mathbf{J}_{\mathbf{h}\to\mathbf{c}} = \frac{1}{3}\begin{pmatrix} -4 & -2 & 1 \\ 2 & -2 & 1 \\ 2 & 4 & 1 \end{pmatrix} \tag{5.13}$$

and

$$\mathbf{J_{c\rightarrow h}} = \frac{1}{2}\begin{pmatrix} -1 & 1 & 0 \\ 0 & -1 & 1 \\ 2 & 2 & 2 \end{pmatrix} \tag{5.14}$$

where, of course, $\mathbf{J_{h\rightarrow c}J_{c\rightarrow h}} = \mathbf{1}$. These matrices can be generated from any two non-collinear vector transformations, such as $(111) \rightarrow (003)$ and $(\bar{1}11) \rightarrow (101)$.

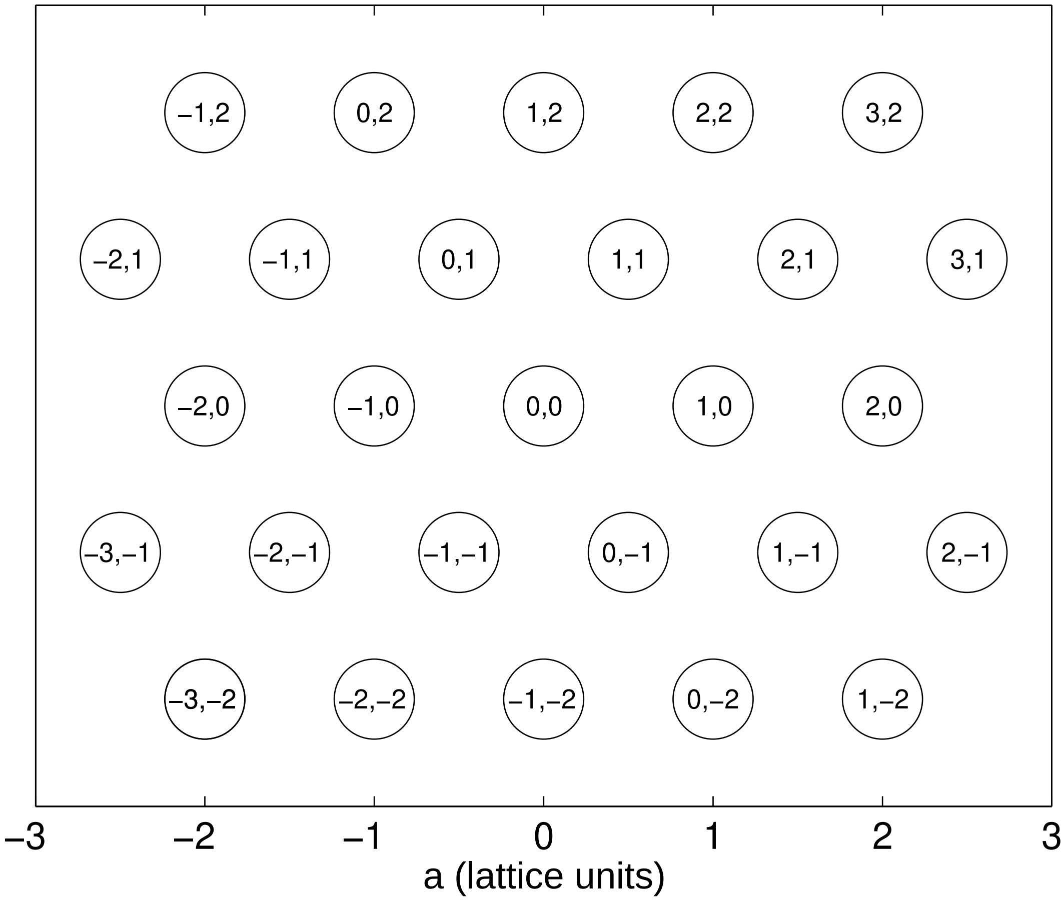

Figure 5.5: Indexing of surface units in real space.

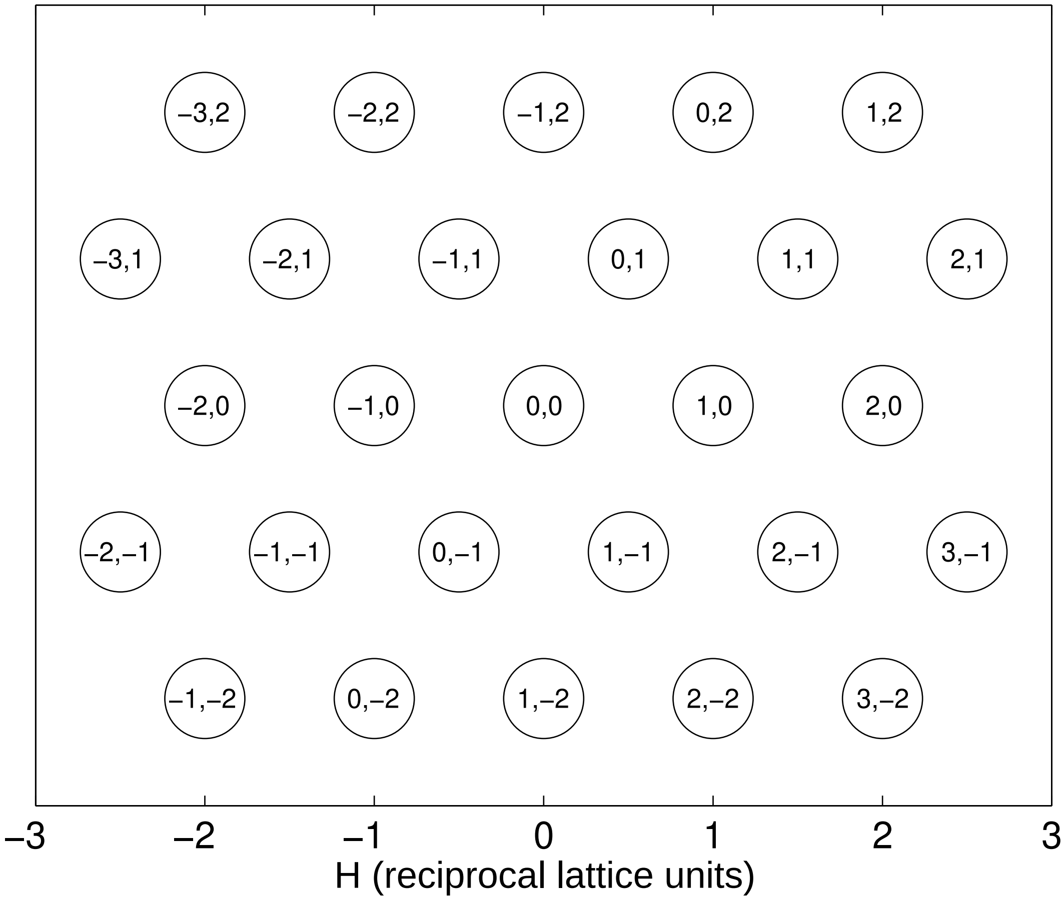

Figure 5.6: Indexing of surface units in reciprocal space.

5.4 Discussion of Incommensurate Structure

Tidswell and coworkers [131] have characterized the incommensurate bilayer that is present for intermediate potentials. They found a triangular array of x-ray scattering rods, sharp in H and K but diffuse in L. The in-plane spacing was approximately 0.765 that of the truncation rods from the underlying platinum crystal. This corresponds to an in-plane bilayer lattice spacing 30% greater than Pt(111). Based upon their measurements of the positions and intensities of these scattering rods, they propose the model shown in figure 5.7. The Cu and Cl form a bilayer wherein the Cu atoms (small gray circles) are close to the Pt surface (large gray circles), and the Cl atoms (large empty circles) rest above the Cu, coordinated in the three-fold hollow sites of the hexagonal Cu lattice. If the Cl atoms are partially ionized toward Cl^- (making them larger), it is reasonable to assume that they are in close proximity to one another and determine the incommensurate lattice spacing. Tidswell *et al.* claim that the spacing is near to that of close-packed spheres with the Cl^- ionic radius.

It is surprising that the bilayer structure fails to follow the commensurate lattice spacing, yet preserves the orientation of the underlying Pt lattice. However, this scenario has been predicted by Novaco and McTague [103]. They hypothesize static-distortion waves (analogous to charge-density waves) in cases where the adlayer is weakly adsorbed to the substrate. Minimizing the energy leads to a preferred orientation of the adlayer with respect to the substrate. The relative orientation angle need not be zero. Shaw, Fain, and Chinn [122] experimentally observed Ar mono-

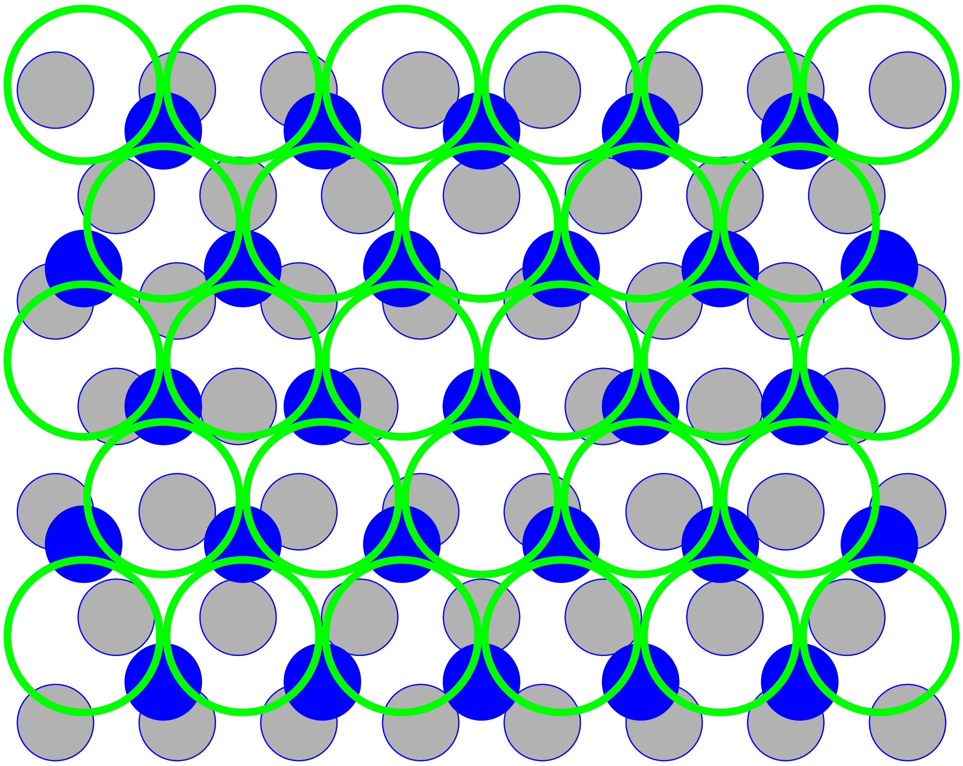

Figure 5.7: Real-space map of the incommensurate overlayer, looking down on the Pt (111) surface (gray). The Cu atoms (black) lie above the Pt substrate and are incommensurate with it. The Cl ions (hollow) lie in three-fold hollow sites above the Cu layer.

layers adsorbed onto graphite substrates at a range of low temperatures (32 – 52 K). Their LEED (low-energy electron diffraction) measurements demonstrated the relative orientation angle was inversely related to the Ar monolayer lattice spacing. Their previous measurements with other adsorbed noble gases find cases where the relative orientation is zero, as in our case. A complete review on this subject can be found in the Pokrovsky and Talapov [110]. Ben Ocko and coworkers [104] have studied a commensurate-incommensurate phase transition in Br UPD on Au(100). Their results are compared with theoretical predictions by Pokrovsky and Talapov [109].

Our interest is primarily in the kinetics of this system, rather than performing more detailed crystallography on the static phases. Therefore, it is necessary to find a useful parameter to monitor the emergence of order during formation of the bilayer. We chose the (0.765 0 L) rod, because it is the lowest index peak. Our choice of $L = 1.5$ depends upon two factors: the minimization of background scattering from solution and polypropylene film, and the L-dependent scattering from the bilayer itself. Absorption effects (section 4.3.4) are most prominent for low L, as is the diffuse background scattering. The bilayer scattering oscillates with L, as can be seen from examining the structure factor.

As mentioned above, the scattering is diffuse along the q_z axis. This is a consequence of the nearly two-dimensional nature of the adsorbed layer. However, the spacing between the Cu and Cl layers causes an interference effect that is manifested in the oscillating intensity along q_z. A single two-dimensional layer of hexagonally arranged atoms has a six-fold rotation axis about the surface normal. Add a second commensurate layer with the same number of atoms, by putting a chloride atom at position $R + a$ for every copper lattice position R. Assuming that these chlorides are attracted to the copper layer, they will probably sit in the three-fold hollow sites between copper atoms. At this point, the symmetry is broken and the bilayer is only three-fold symmetric.

To derive the structure factor, we need to find the coordinates of the three-fold hollow site. Consider the location of the three-fold hollow site between (0,0), (1,0), and (1,1). Referring to figure 5.8, and recalling that the center of an equilateral triangle is 1/3 of the distance from a side to the opposite vertex, the position is

$$\frac{1}{2}(1\ 0) + \frac{1}{6}(1\ 2) = \left(\frac{2}{3}\ \frac{1}{3}\right) \tag{5.15}$$

Now we turn our attention to the phase factors that influence the structure factor of the bilayer. We can consider the two-dimensional CuCl bilayer as though it were in isolation. The underlying Pt lattice has no fixed periodicity with respect to it, and so will not change any of the structure factors except at the specular condition $H = K = 0$. As shown in section 3.9.2, the structure factor due to the addition of another atom is

$$S(\mathbf{q}) = \left|\sum_{j=1}^{n} e^{i\mathbf{q}\cdot\mathbf{a}_j}\right|^2 . \tag{5.16}$$

The Cl atom sits at the three-fold hollow site, and using $q = 2\pi/a(H,\ K)$ from (5.15), the structure factor at $L = 0$ is

$$S(H, K, L = 0) = \left|1 + \exp\frac{2\pi i}{3}(2H + K)\right|^2 = \begin{cases} 4 & 2H + K = 3n \quad n \text{ any integer} \\ 1 & \text{otherwise} \end{cases} . \tag{5.17}$$

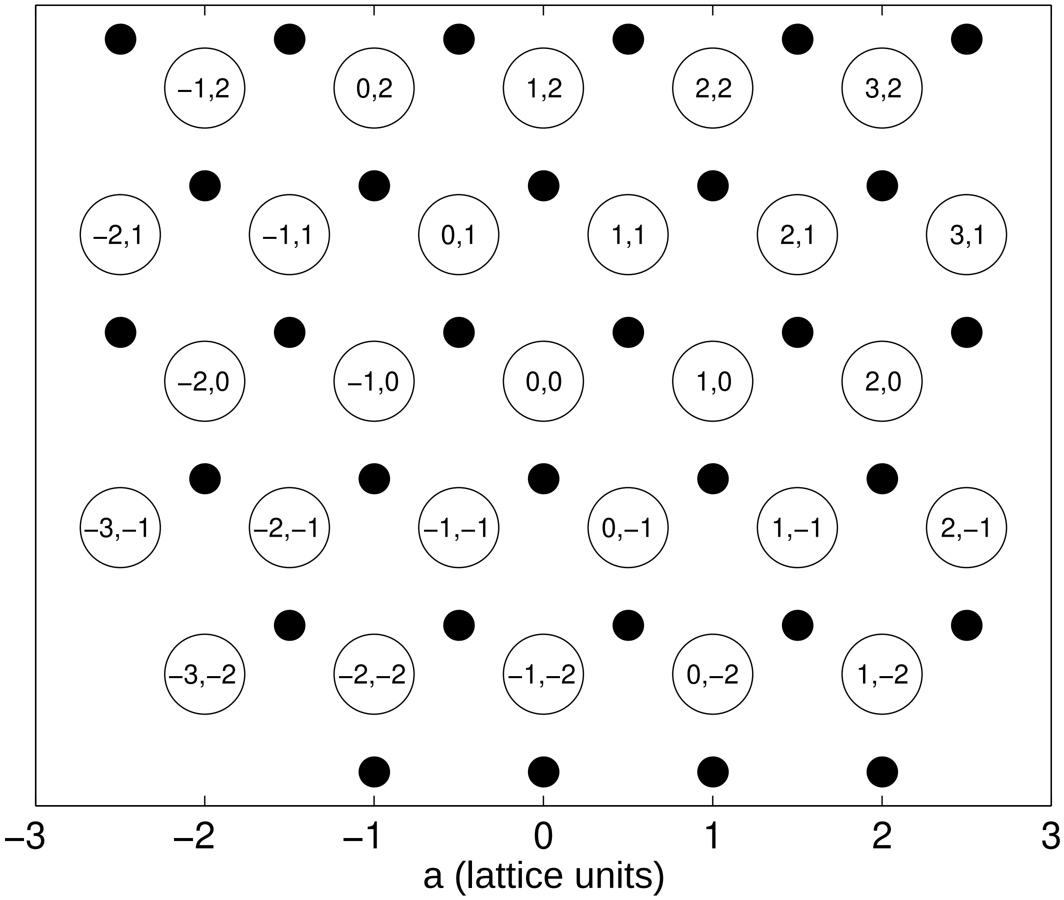

Figure 5.8: Real space image of bilayer. The open circles represent the positions of the copper atoms, and the closed circles represent the positions of the chloride atoms. In reality, the chloride atoms occupy considerably more space than the copper atoms, as shown in figure 5.7.

This leads to a hexagonal lattice expanded by a factor of $\sqrt{3}$, and rotated by $30°$, as shown in figure 5.9.

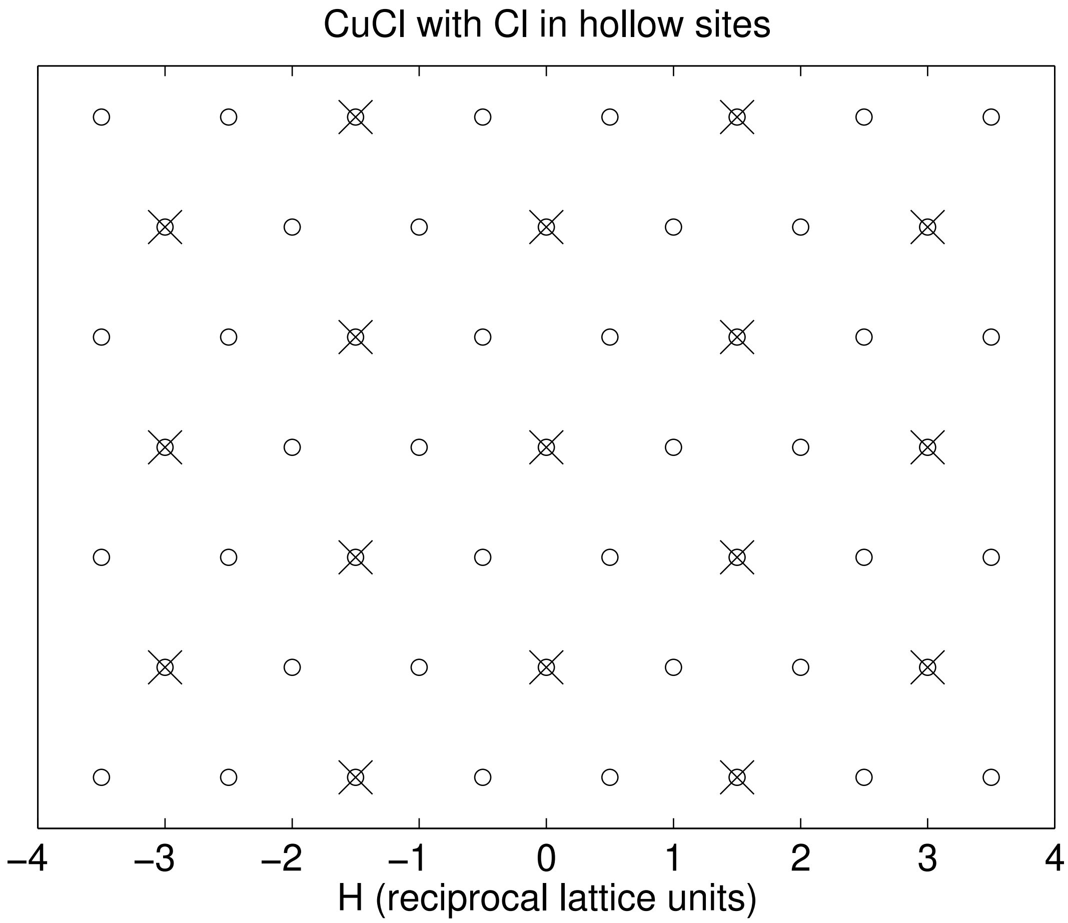

Figure 5.9: Reciprocal space map of monolayer (circles) and bilayer (crosses). The monolayer points correspond to figure 5.6. The bilayer points incorporate the $L = 0$ structure factor from (5.17).

Now consider the $L > 0$ scattering. Due to the three-fold symmetry, the points (0 0), (1 0), and (0 1) illustrate all of the possible cases. (The (1 1) is equivalent to the (0 0).) These structure factors are plotted in figure 5.10. As expected, they follow a simple sinusoidal form, but the initial phase at $L = 0$ is determined by (5.17).

The careful reader will note that I have neglected the atomic form factors of Cu and Cl (that depend upon the ionization state, which is not known), and the "Debye-Waller" factors due to disorder within the Cu–Cl bilayer. However, in my opinion, there is a larger uncertainty that makes these considerations moot. The illustration in figure 5.9 is only one of two possibilities. The six-fold symmetry was broken by the assumption that the chloride atoms fall into the upward-pointing triangles of figure 5.5. We can equally well imagine that the chloride atoms fall into the downward-pointing triangles. This is equivalent to just a 60° rotation and changes the structure factors accordingly.

The three-fold hollow site immediately above (along the y-axis) from the origin in figure 5.9 is $\frac{1}{3}(1\ 2)$. (This is not shown in the figure, because we previously took the other choice.) The resulting structure factor is

$$S(H,K,L=0) = \left|1 + \exp\frac{2\pi i}{3}(H+2K)\right|^2 = \begin{cases} 4 & H+2K=3n \quad n \text{ any integer} \\ 1 & \text{otherwise} \end{cases} . \tag{5.18}$$

We see that the roles of H and K are reversed from (5.17).

Even more likely is that there will be some combination of these two possibilities. As the incommensurate bilayer forms, different domains nucleate and grow on the surface (see chapter 6). There will be domains with both possible orientations. These domains are likely to be incoherent; that is, there will be no definite phase

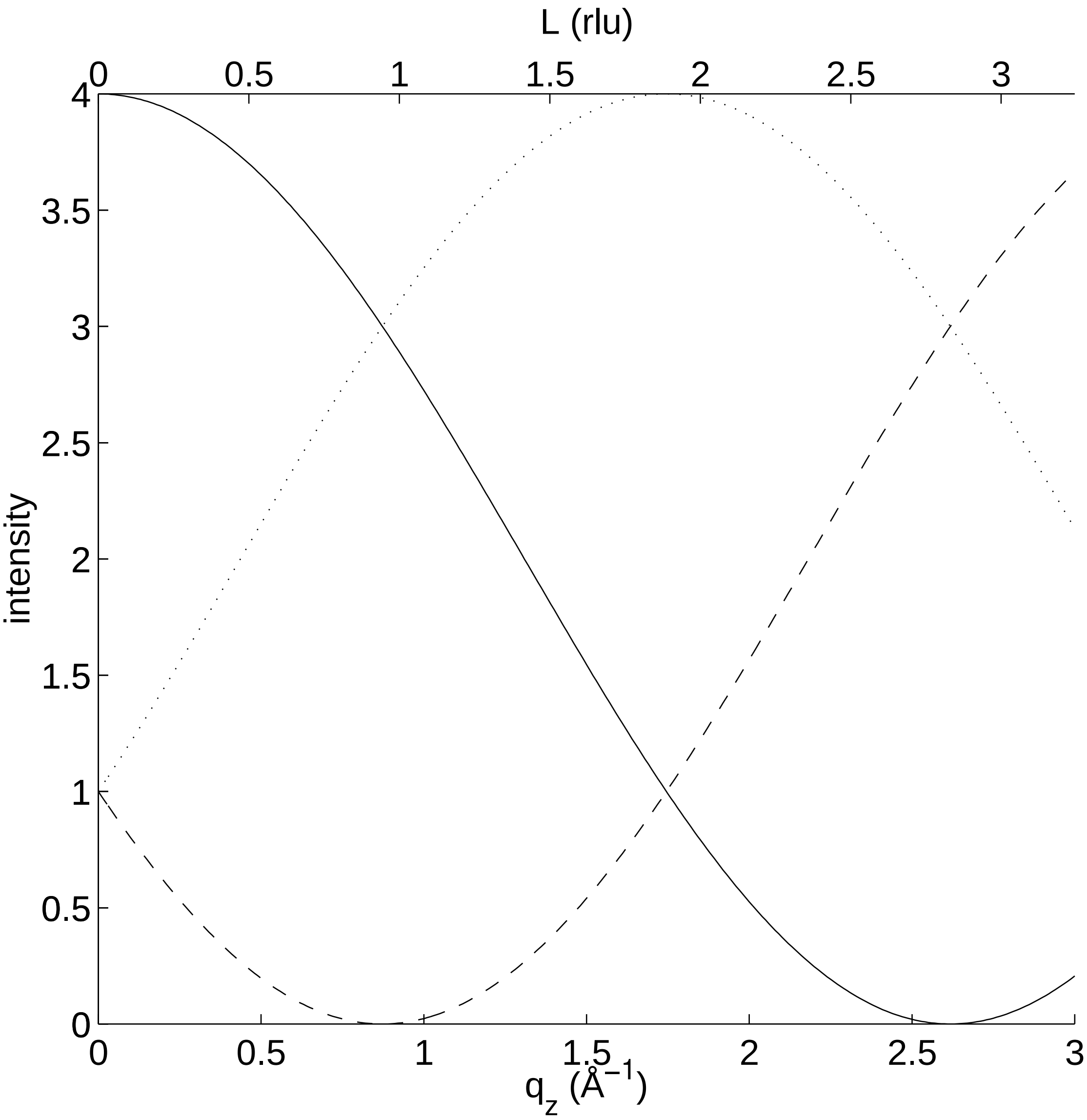

Figure 5.10: Structure factors for various the (0 0) (solid), (0 1) (dotted), and (1 0) (dashed) rods as a function of q_z.

relationship between them. The overall intensity will be the sum of the intensities from all the domains. This intensity is shown in figure 5.11, which assumes an equal coverage for the two domain types. As can expected from the sum of two sinusoidal functions, the period of the oscillation is changed. The (0 1) and (1 0) structure factors are identical, since we are taking equal numbers from the two domain type, so H and K are identical. Of course, due to the stochastic nature of the nucleation–growth process, the distribution may be skewed toward one orientation over the other, instead of the $1:1$ ratio depicted here.

5.5 Static X-ray Data

Because of the conflicting reports of the CuCl overlayer structure at intermediate voltages, our first task was to make some static x-ray measurements. We have observed the overlayer structure numerous times during several experimental runs. Despite many attempts, we have never found scattering at the $(0.25m\ 0.25n\ L)$ rods that can be attributed to the incommensurate overlayer, where m and n are integers up to 6. On the other hand, we have found scattering at the $(0.765\ 0\ L)$ and $(0\ 0.765\ L)$ rods that was voltage-dependent. This indicates that the measurements of Tidswell *et al.* [131] are correct, while the LEED measurements of Kolb [102] cannot be confirmed. Assuming that the $(0.75\ 0\ L)$ seen in the LEED corresponds to the $(0.765\ 0\ L)$ peak, then the additional peaks may be the result of multiple electron scattering. Alternatively, the *ex situ* experiment may change the ordering of the CuCl overlayer. This would not be surprising, as the vacuum and solution

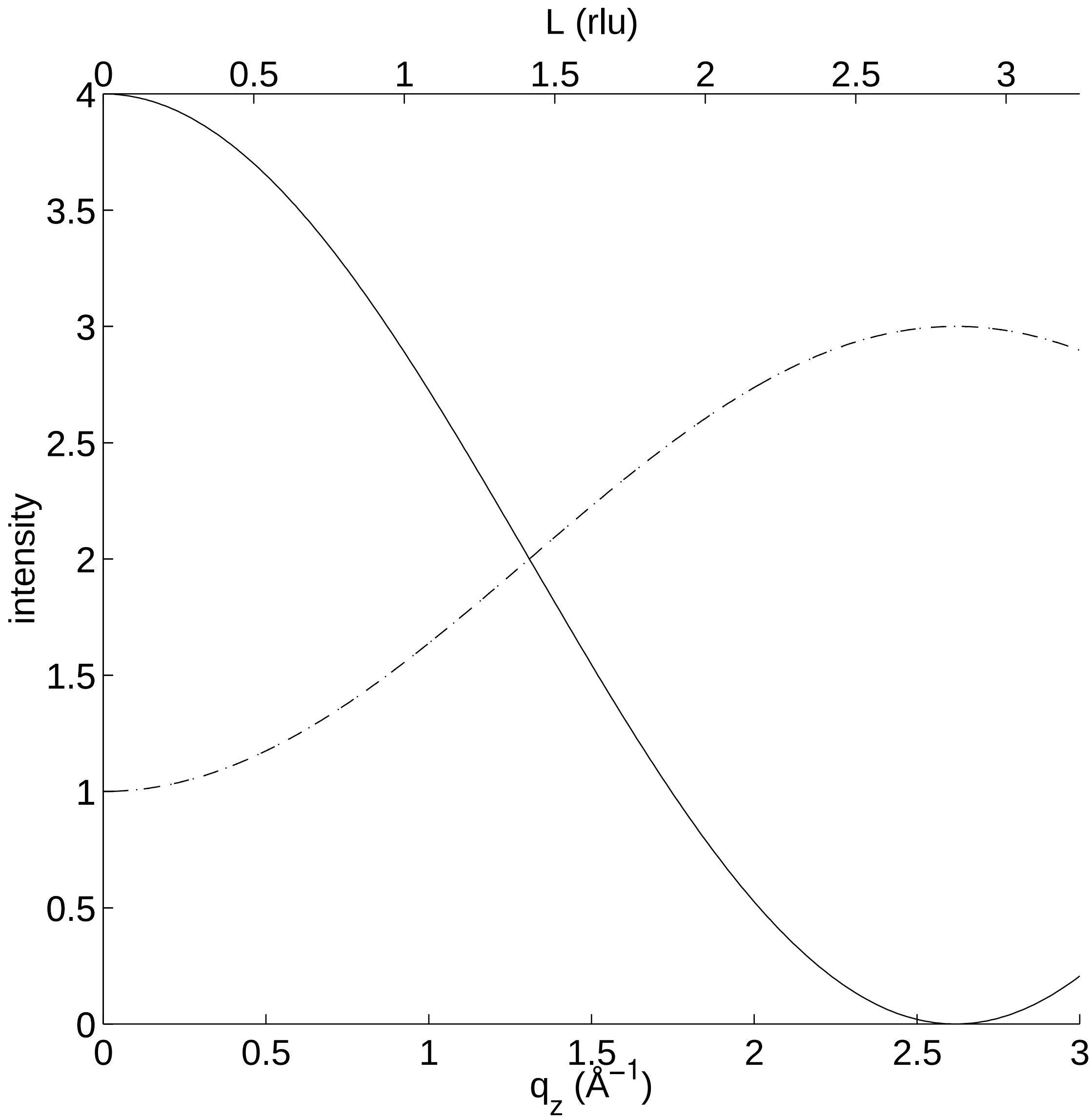

Figure 5.11: Structure factors for various the (0 0) (solid), (0 1) (dotted), and (1 0) (dashed) rods as a function of q_z. The (0 1) and (1 0) coincide.

environments are very different.

Figure 5.12 shows the (0.765 0 1.5) overlayer Bragg peak at two different values of the applied potential. These data clearly demonstrate the presence of the incommensurate overlayer at 350 mV and its absence at 250 mV. The potential-independent background is due to scattering from the solution layer and the polypropylene film that contains it. By integrating for several seconds per $\mathbf{q}$-point, the signal can be easily resolved above this background. In the time-resolved measurements (chapter 6), where the x-ray signal is split into many time bins, this poses a considerable experimental challenge.

The shape of the diffraction peak is well-fit by a Lorentzian line shape (the solid line in figure 5.12), and the half-width at half-maximum Δ corresponds to a correlation length $\xi = 1/\Delta \approx 280$Å. A Lorentzian is appropriate for systems with only short range positional order. The inset indicates the location of the Bragg rods of the two-dimensional incommensurate overlayer (hollow) and the crystal truncation rods (section 3.11.1) of the Pt substrate (filled). The arrow represents the transverse scan shown in the main figure. The transverse direction is denoted by $\mathbf{q}_\perp$ and is orthogonal to (0.765 0) and at constant L.

The corresponding x-ray scans through the overlayer Bragg peak, but along the radial direction, are shown in figure 5.13. The radial direction is denoted by $\mathbf{q}_{||}$ and holds K and L constant. In this case, the peak is broader than scans through the $\mathbf{q}_\perp$ direction. At first glance, this appears to indicate that the correlation function is strongly asymmetric, with $\xi_\perp > \xi_{||}$. This would be a surprising result. However, as the next paragraphs will show, this can be accounted for by the asymmetry of

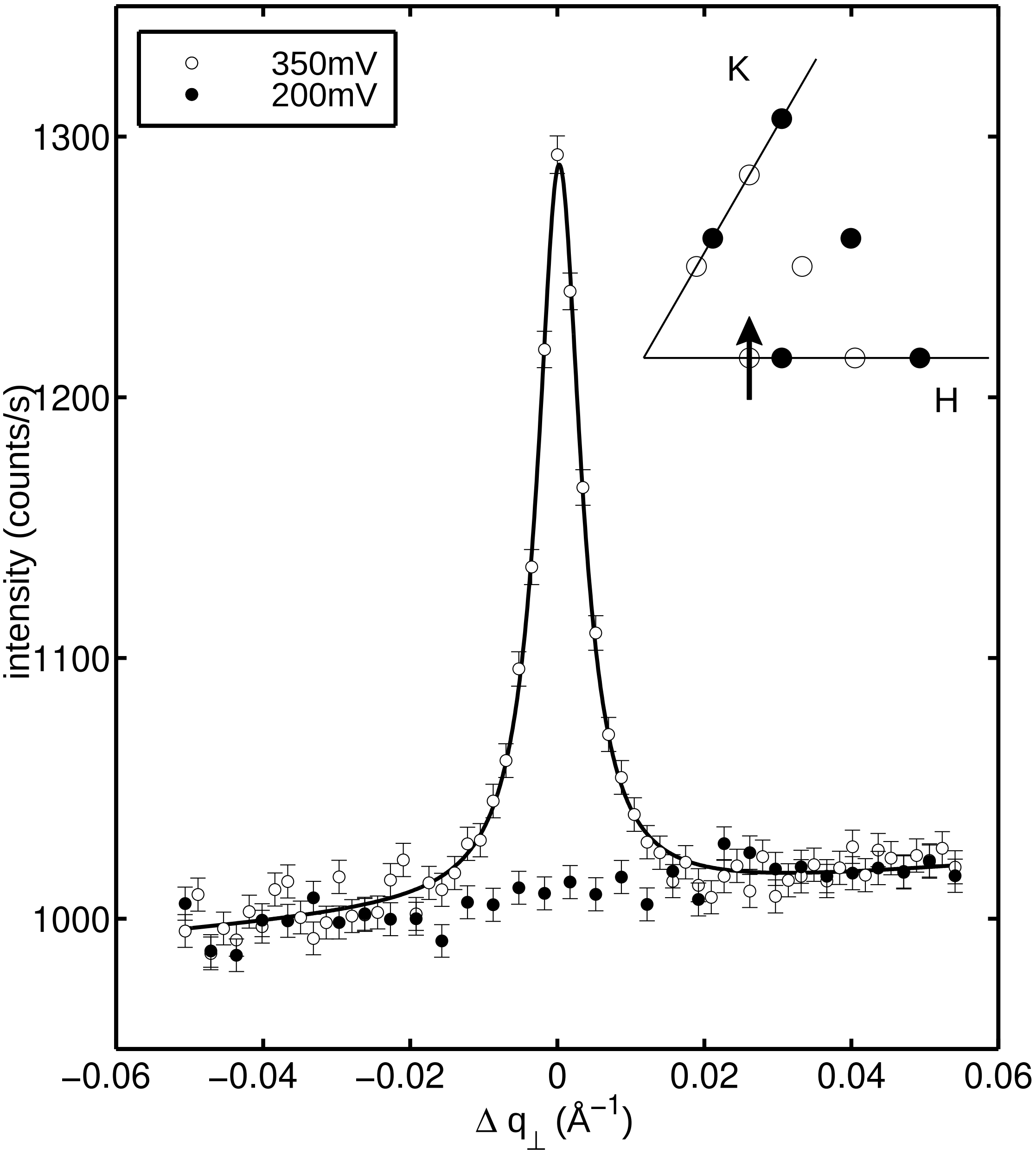

Figure 5.12: Scattered intensity at $\mathbf{q} = (0.765\ 0\ 1.5) + \mathbf{q}_\perp$ at 350 mV (hollow) and 200 mV (filled) vs. Ag/AgCl. The solid line is the best fit to a Lorentzian line shape.

the resolution function.

The asymmetry of the resolution is due to the differing longitudinal and transverse resolutions. Figure 5.14 depicts the elements of the scattering geometry that determine the resolution. A variation in $\theta = \frac{1}{2}(2\theta)$, the scattering angle between $\mathbf{k}_f$ and $\mathbf{k}_i$, causes $\mathbf{q}$ to trace out the major axis of the resolution ellipse. A variation in the magnitudes k_i and k_f, due to a variation in the θ_{beam} striking the monochromator, causes $\mathbf{q}$ to trace out the minor axis of the resolution ellipse. As shown in the figure, the longitudinal $\mathbf{q}$ and transverse $\mathbf{q}_\perp$ directions are not exactly coincident with the major and minor axes of the resolution ellipse, but are rotated by θ with respect to it. A careful consideration of the resolution function is required for extremely high-resolution experiments [45]. For this relatively low-resolution experiment, the relative rotation is neglected.

As already used, "perpendicular" ($\mathbf{q}_\perp$) and "parallel" ($\mathbf{q}_{||}$) refer to vectors in the $\mathbf{a}^*$, $\mathbf{b}^*$ plane (constant L). The term "longitudinal" refers a direction along the scattering vector $\mathbf{q}$, while "transverse" is the direction orthogonal to this, but still in the scattering plane. At this point in reciprocal space, the $\mathbf{q}_\perp$ direction corresponds to the transverse direction. The $\mathbf{q}_{||}$ direction corresponds closely to the longitudinal direction, but is slightly different because of the constraint that L remain constant in $\mathbf{q}_{||}$.

The longitudinal resolution is found by differentiating the definition of q (3.30),

$$\delta q = \frac{4\pi}{\lambda} \cos\theta \; \delta\theta \; . \tag{5.19}$$

In order to maximize the empirical signal to noise ratio, we used longitudinal (cor-

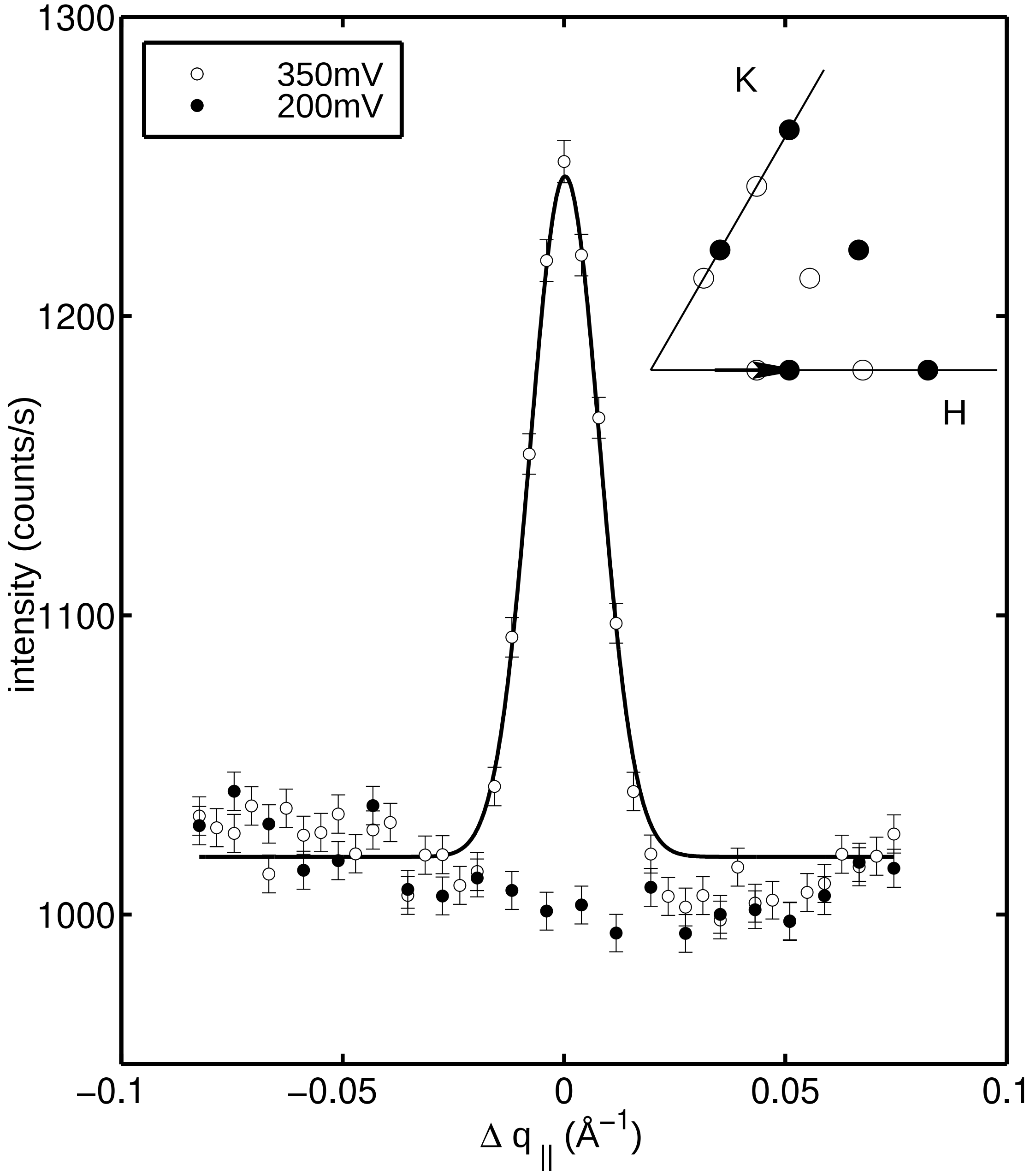

Figure 5.13: Scattered intensity at $\mathbf{q} = (0.765\ 0\ 1.5) + \mathbf{q}_{\|}$ at 350 mV (hollow) and 200 mV (solid) vs. Ag/AgCl. The solid line is the best fit to a Lorentzian line shape.

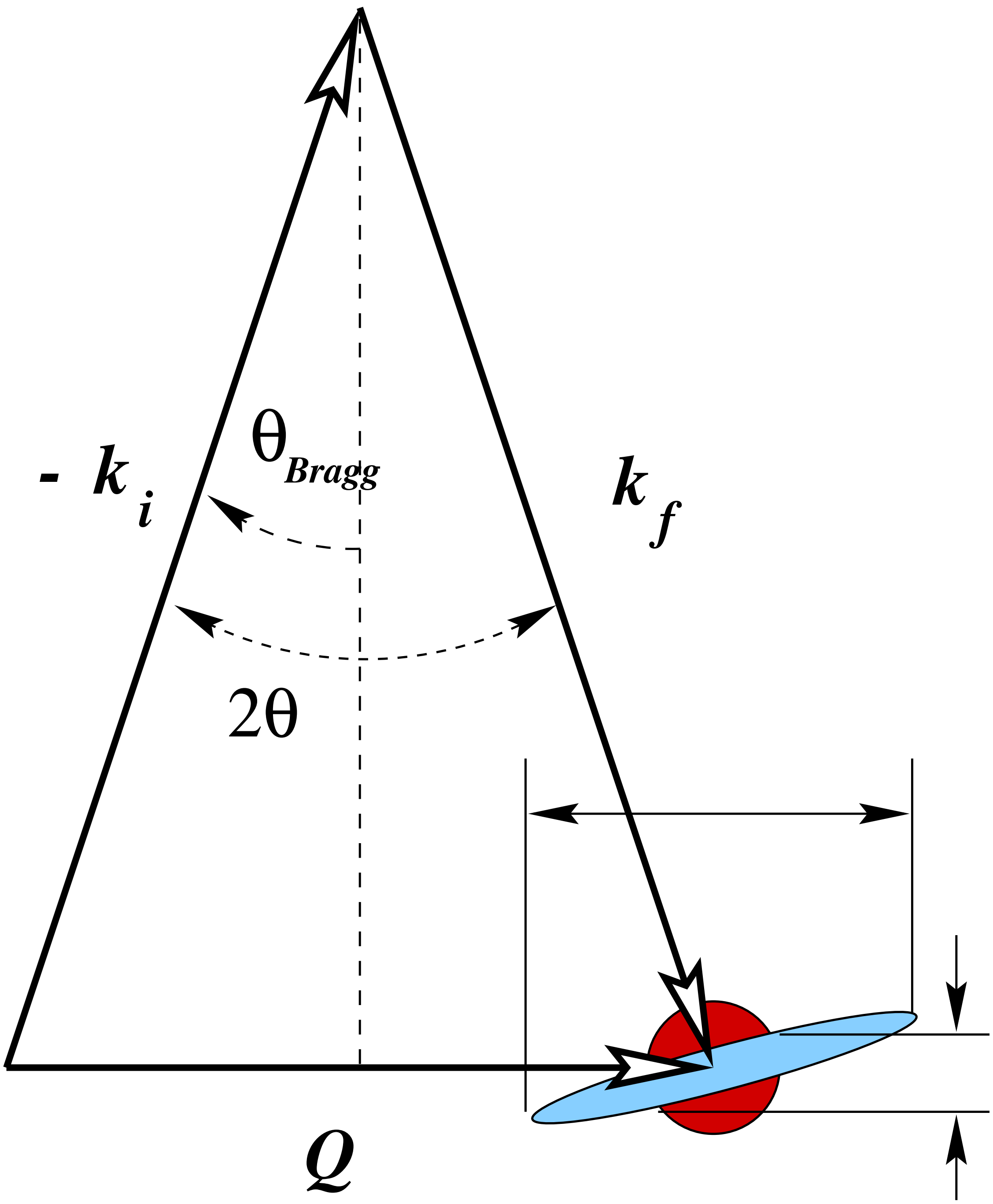

Figure 5.14: Cartoon of resolution function. (Created by Joel Brock.)

responding to 2θ) slits 2.0 mm wide . This produced a resolution of $\Delta(2\theta) = 0.20°$ (full-width at half-maximum). The transverse resolution is found to be

$$\delta q_{\perp} = q\,\theta_{\mathrm{beam}} \tag{5.20}$$

where $\Delta(2\theta_{\mathrm{beam}}) = 0.012°$ (full-width at half-maximum) is determined by the opening angle of the synchrotron (3.1).

To confirm these calculations, we also measured x-ray intensities through the (1 0 L) crystal truncation rod (CTR) at the same $L = 1.5$ and $\mathbf{q}_{\perp}$, $\mathbf{q}_{||}$ directions as in figures 5.12 and 5.13. X-ray scans through the CTR and the overlayer rod are shown in figures 5.15 and 5.16. The top panel of each figure illustrates the intensity data, normalized to the beam monitor. The scattering from the overlayer is barely observable in comparison with the CTR scattering. This is not surprising, because the CTR intensity falls as $\sim 1/(q_z - q_0)^2$, where q_0 is the Bragg peak position, and $L = 1$ for this rod. The bottom panels illustrate the same data, but normalized to unity so that the widths may be compared. The overlayer rod is broader than the CTR in each figure.

The calculated resolutions and measured peak widths are summarized in table 5.1. Each quoted value is a full-width at half-maximum. The first and third columns are calculated longitudinal (5.19) and transverse (5.20) resolutions for the CTR and overlayer rod. The second and fourth columns are measured widths of peaks in the shown in the previous figures for the ϕ, $\Delta q_{\perp}$ and H, $\Delta q_{||}$ directions.

It may seem surprising that the measured width δq_H for the CTR is less than the calculated resolution δq. However, this is just an indication that H is not collinear

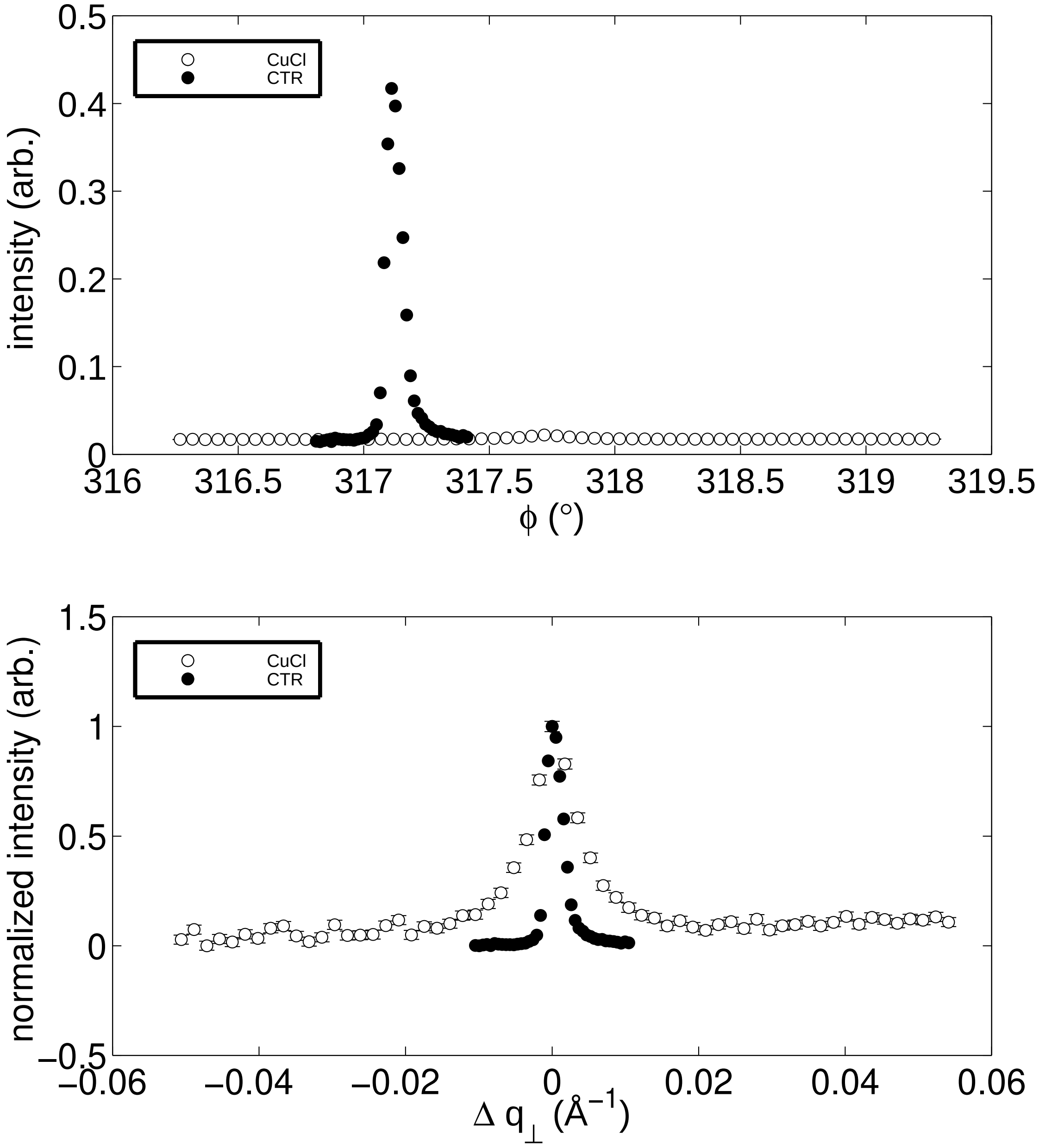

Figure 5.15: Comparison of the (1 0) crystal truncation rod (filled) and the (0.765 0) overlayer Bragg scattering rod (hollow) at $L = 1.5$. Both are measured in the $\mathbf{q}_\perp$ direction and at 350 mV. The overlayer peak is barely visible near $\phi = 317.6$.

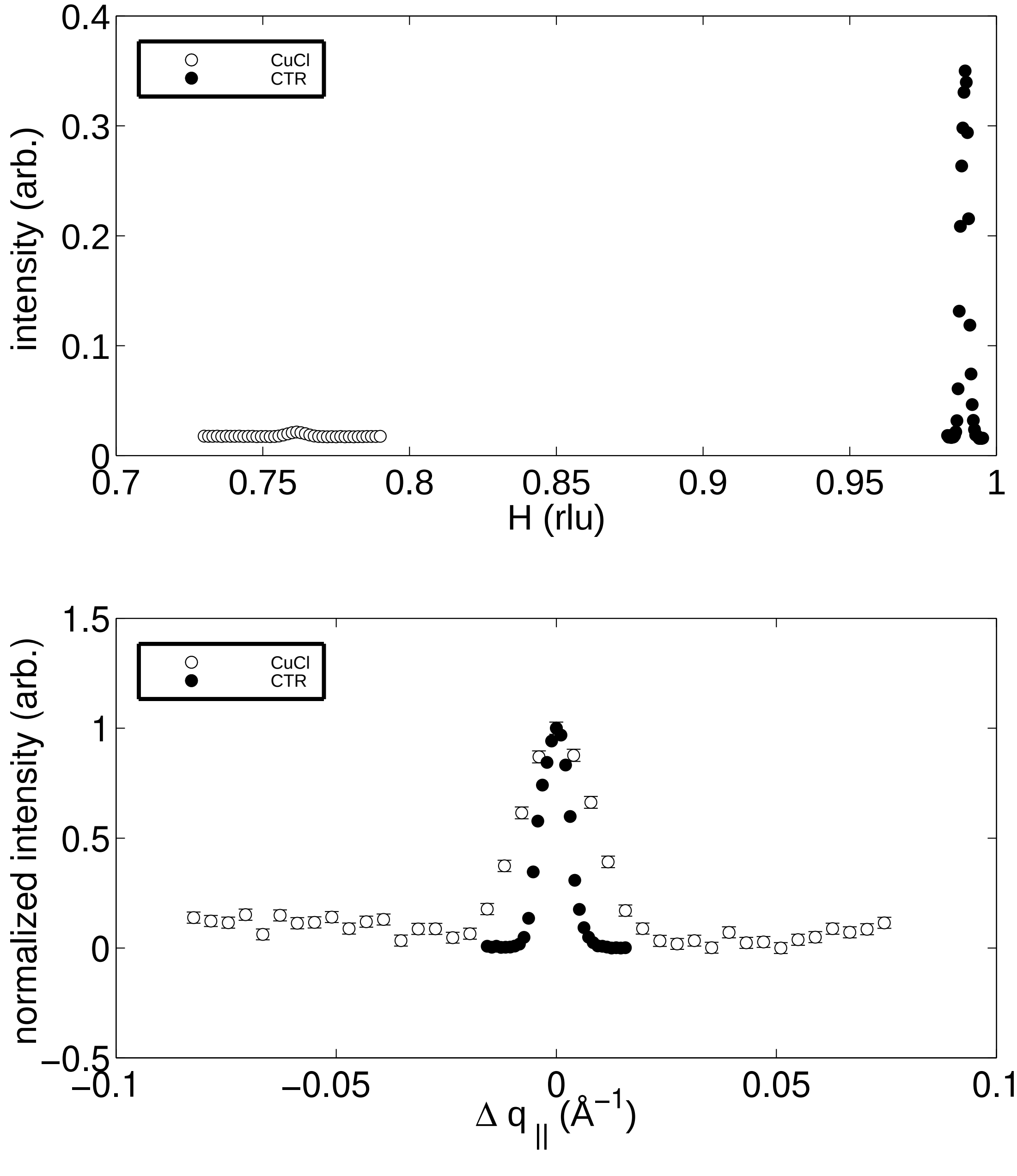

Figure 5.16: Comparison of the (1 0) crystal truncation rod (filled) and the (0.765 0) overlayer Bragg scattering rod (hollow) at $L = 1.5$. Both are measured in the $\mathbf{q}_{\|}$ direction and at 350 mV.

Table 5.1: Summary of measured peak widths (δq_H, δq_ϕ) and calculated resolutions (δq, $\delta q_\perp$). All values are full-width at half-maxima.

peak	δq (Å^{-1})	δq_H (Å^{-1})	$\delta q_\perp$ (Å^{-1})	δq_ϕ (Å^{-1})
Pt(111) CTR	14.7×10^{-3}	7.1×10^{-3}	0.31×10^{-3}	2.5×10^{-3}
CuCl overlayer	15.0×10^{-3}	18×10^{-3}	0.25×10^{-3}	7.1×10^{-3}

with the longitudinal direction. Referring to figure 5.14, a cut through the resolution ellipse along a direction other than the major axis (the longitudinal direction) will always produce a more narrow profile.

As indicated, the resolution function is extremely asymmetric, with $\delta q \gg \delta q_\perp$. By comparing δq_H and δq, the overlayer rod is seen to be resolution-limited when measured along $\mathbf{q}_{\|}$. However, the overlayer rod is found to be very well-resolved along $\mathbf{q}_\perp$ by comparing δq_ϕ and $\delta q_\perp$. From this consideration, widths from scans of the overlayer along $\mathbf{q}_\perp$ (figure 5.12) can be considered intrinsic to the CuCl overlayer itself, and a correlation length of $\xi \approx 280$Å can be quoted without resort to deconvolution.

The width of a CTR is related to the terrace size, but in a complicated way. For a self-affine surface (where there is no intrinsic length scale parallel to the surface), then the CTR width at the anti-Bragg position (midway between two Bragg peaks) is inversely proportional to the mean terrace size. When there is a characteristic surface length scale, the CTR width is in general a function of that length scale as well. In this case, the relationship to terrace size is specific to the correlation function which generates that length scale. As expected, the overlayer rods in our experiment are always significantly broader than the CTRs. This suggests that the terrace size is not the primary limitation on the mean island size. Without a separate and very careful surface crystallography experiment, however, this cannot be definitively proven.

Chapter 6

Kinetic Measurements

6.1 Introduction

In this chapter, simultaneous electrochemical and x-ray scattering measurements of the ordering kinetics of the Cu–Cl bilayer during the transition from the commensurate copper overlayer to the incommensurate bilayer are reported. First, the time-resolved data are presented. Then, a simple theory for the nucleation of the incommensurate phase is described. The subsequent section presents data to support this model. Next, the entire q–t data set is presented, followed by a theory to describe it. The data is analyzed in the context of this theory, and excellent agreement is found. The final sections concern alternate models and further theoretical explanations.

6.2 Time-Resolved Data

To observe the ordering kinetics during stripping, we employed a simple signal averaging technique. An example of the square-wave potential cycle that we applied is shown in figure 6.1a. At $t = 0$, the potential begins at 200 mV. The voltage is stepped to 350 mV at $t = 10$ seconds. At $t = 30$ seconds, the voltage is stepped back to 200 mV. This cycle repeats with a period of 40 seconds. Throughout this cycle, we simultaneously monitor both the current (figure 6.1b) and the intensity of the scattered x-rays at $\mathbf{q}_\perp$ corresponding to the peak of figure 5.12. As expected, the incommensurate scattering peak is present only for values of the potential within the incommensurate phase. Note that the rise in the intensity of the scattered x-rays in figure 6.1c is much slower than the corresponding current transient in figure 6.1b. In contrast, the scattered intensity falls on a time scale similar to that of the current transient.

The current transients describe the charge transfer at the electrode interface. These are due to two contributing processes: the capacitive charging of the double-layer, and the Faradaic charge transfer due to desorption/adsorption of ions.

Some previous chronoamperometric studies of closely related systems [79, 80] exhibit distinct features in the current response that have been interpreted as evidence of nucleation. These characteristic features are not present in our data. We suspect that the geometry of the thin solution layer x-ray cell may be responsible for this difference. The capacitive effect is greater for our larger samples. This strong signal tends to mask other early features in the current response. Also, in our apparatus,

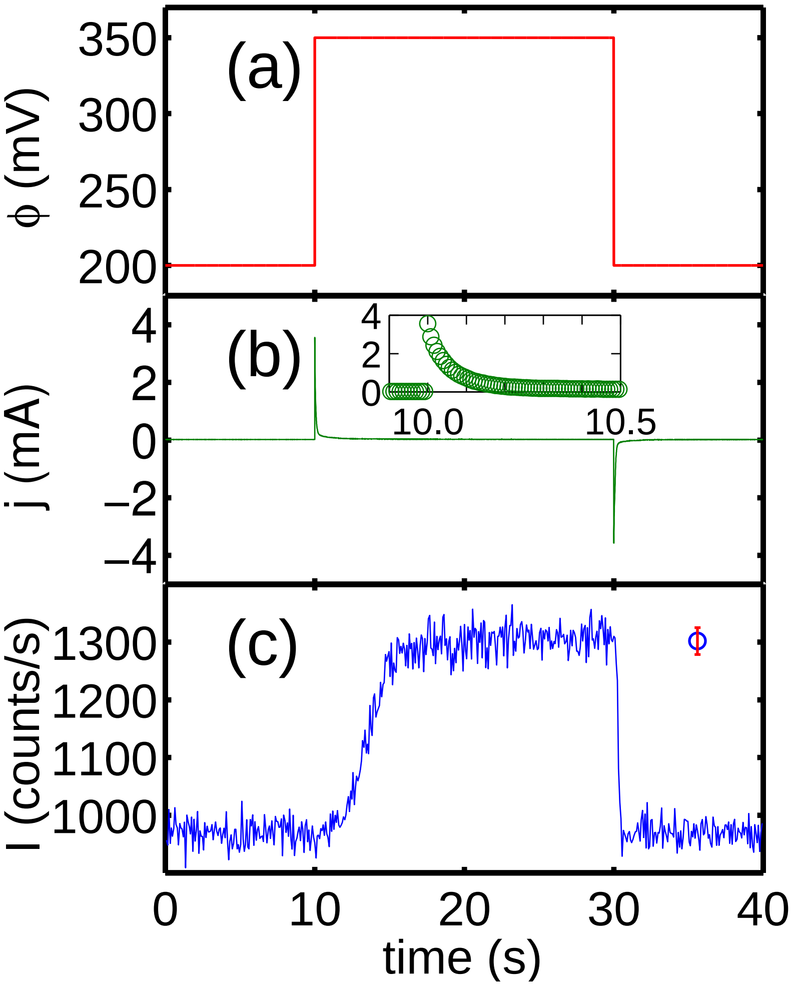

Figure 6.1: (a) Applied potential steps. (b) Current transients. (c) Time dependence of the integrated intensity of the (0.765 0 1.5) overlayer diffraction peak.

as compared with hanging meniscus cells used in the other experiments, diffusion is comparatively insignificant. First, diffusion from the "bulk" solution is not a consideration for us, because the solution layer is so thin. Second, any diffusion that does take place will occur in one dimension, rather than three. Above the planar electrode face, the solution layer forms a very short cylinder. The ions are in close proximity to the surface and conditions are probably relatively uniform across the face, so diffusion is primarily along the surface normal.

After numerous attempts, we can definitely say that there are no features in the current response at the same time as the x-ray response. So the measured current response is ascribed to desorption/deposition into a disordered state (accompanied by charge transfer) which then gives rise to the nucleation and growth of the equilibrium ordered phase. The rise in x-ray intensity corresponds to an increased population in the incommensurate ordered phase. The desorption process can be separated from the ordering process due to the widely disparate time scales involved. Based on these data, we hypothesize a scenario wherein the abrupt positive voltage step causes a expulsion of some of the adsorbed copper ions. The remaining disordered ions gradually reorganize into a two-dimensional crystalline state with a larger lattice constant, incommensurate with the platinum substrate.

6.3 Stochastically Nucleated Islands

Consider the nucleation of (ordered) islands from a disordered phase, as depicted in figure 6.2. As usual, we define the Gibbs free energy of an island to be proportional

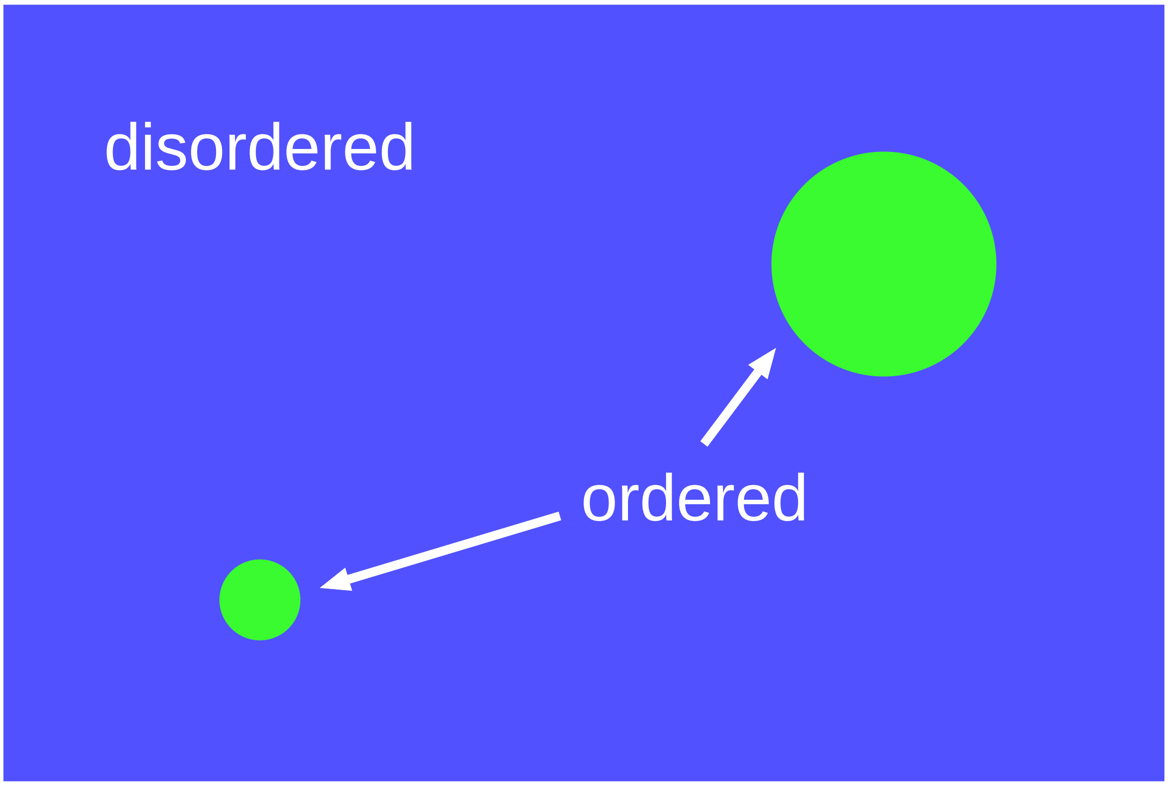

Figure 6.2: Cartoon of a nucleation process.

to the (electro)chemical potential and to the number of particles that comprise the island. An island in contact with another phase will give rise to an excess free energy term proportional to the surface area of contact. So the existence of an island with N particles will lead to an excess of free energy

$$\Delta G(N) = N(\tilde{\mu}_{\text{ordered}} - \tilde{\mu}_{\text{disordered}}) + \gamma S \tag{6.1}$$

where μ_{ordered} and $\mu_{\text{disordered}}$ refer to the electrochemical potentials of the respective phases. The surface free energy generated by the boundary between phases is taken as the product of a constant coefficient γ and the surface area. Defining the overpotential as

$$\eta = \Delta V - \Delta V_0' \tag{6.2}$$

then the Gibbs free energy is

$$\Delta G(N) = -Nze\eta + \gamma S \ . \tag{6.3}$$

This linear dependence of $G(N)$ upon η can arise from least three different scenarios. Analogously to the example described by Schmickler [117], the desorption may be accompanied by a shift in the electric potential. For instance, if the ordering process involves the desorption of ions, then those ions would lose contact with the electrode surface and no longer be at the applied potential ΔV. Another possibility involves a change in the ionization state such that the ionic charge changes by ze. The lack of any observed charge transfer across the electrode interface at times corresponding to the ordering process (see section 6.3) argues against these scenarios. In the third scenario, the ordering process is driven by the change in adsorbate density after deposition. This is discussed in detail in section 6.11.

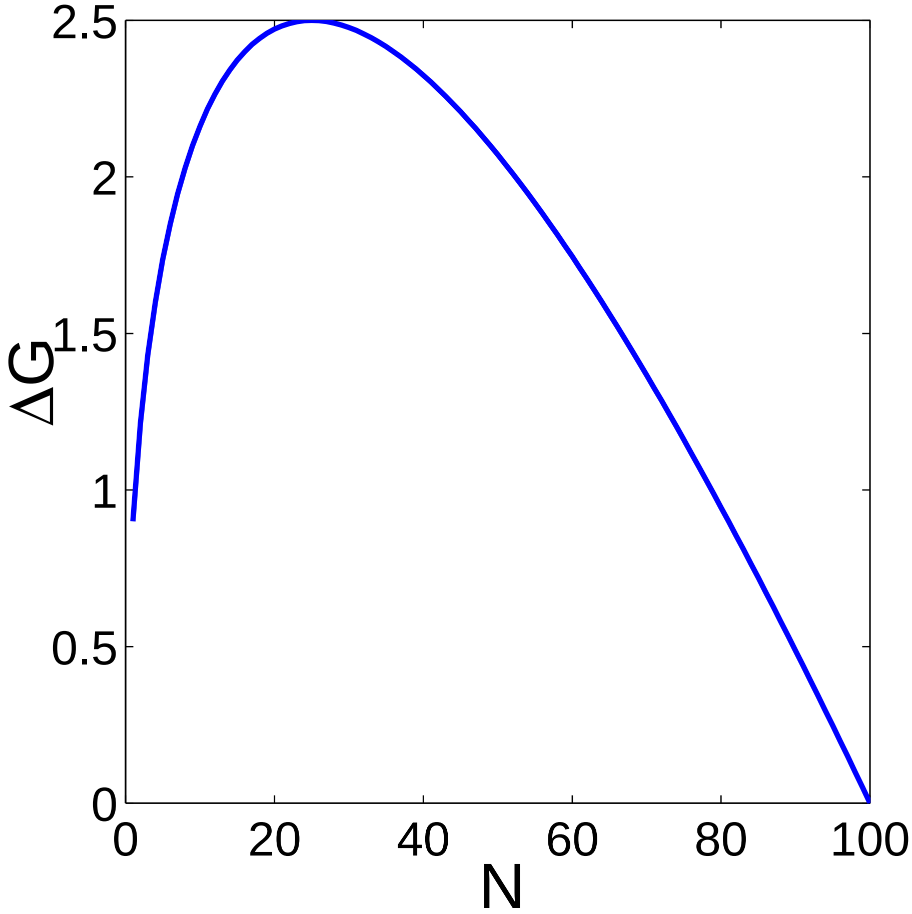

Figure 6.3: Example of Gibbs free energy ΔG as a function of particle number N.

For an arbitrary (perhaps fractal) island of dimensionality d, then

$$S = aN^{(d-1)/d} \,. \tag{6.4}$$

The loss in ΔG from the η-dependent first term competes with the gain in ΔG from the surface free energy. The loss scales with the interior volume of the island (as N), and dominates for large N. The gain scales more weakly as the surface area and dominates for small N. The consequence of this are functional forms for ΔG exemplified in figure 6.3. There will be a critical N_{crit} such that islands with $N < N_{\mathrm{crit}}$ will shrink to vanishing and islands with $N > N_{\mathrm{crit}}$ will grow arbitrarily large. This critical island number can be determined by setting $\partial G/\partial N = 0$,

$$N_{\mathrm{crit}} = \left(\frac{d}{d-1} \frac{ze\eta}{\gamma a} \right)^{-d} \tag{6.5}$$

and the energy barrier that must be overcome to nucleate an island of this size is

$$\Delta G_{\mathrm{crit}} = \Delta G(N_{\mathrm{crit}}) = \frac{(d-1)^{d-1}}{d^d} \frac{(\gamma a)^d}{(ze\eta)^{d-1}} \tag{6.6}$$

For later discussion, the most important result of this derivation is that $\Delta G_{\mathrm{crit}} \propto \eta^{1-d}$, which is just the d-dimensional generalization of an expression found in [117].

Assume that there is some stochastic attempt frequency k_{att} to make islands, only some of which are able to surmount the energy barrier. Also assume a Boltzmann distribution of energies in the attempt profile. Then the rate of islands successfully nucleated is

$$k_N = k_{\mathrm{att}} \exp(-\Delta G_{\mathrm{crit}}/kT) \tag{6.7}$$

and a characteristic time is

$$\tau \propto \frac{1}{k_N} = \frac{1}{k_{\mathrm{att}}} \exp\left(\frac{\Delta G_{\mathrm{crit}}}{kT} \right) \sim \exp(\eta^{1-d}) \tag{6.8}$$

6.4 Instantaneous vs. Progressive Nucleation

Let $N(t)$ be the number of nuclei at time t. Following Schmickler, we assume "first-order kinetics" as follows:

$$N(t) = N_\infty[1 - \exp(-k_N t)] \tag{6.9}$$

This defines k_N, the nucleation rate. There is no strong reason to believe that the nucleation rate follows some sort of first-order restoring force as $dN/dt = k(N_\infty - N)$, upon which (6.9) depends. But this form allows an interpolation between two limiting cases, often described in the literature. "Instantaneous" nucleation refers to situations where the all possible nuclei have formed before the time of observation of the system. This corresponds to $k_N t \gg 1$ in equation (6.9) and yields $N(t) = N_\infty$. "Progressive nucleation" refers to the opposite limiting case, where the nucleation process is at its early phase throughout the time of observation. This corresponds to $k_N t \ll 1$ in equation (6.9) and yields a linearized $N(t) = N_\infty k_N t$.

Of course, these are only limiting cases. Although many experiments in the literature attempt to distinguish between instantaneous and progressive nucleation, we expect in general to find systems that exhibit both types of behavior, depending upon the rate of nucleation k_N (which may be controllable) and the time scale of measurement.

In figure 6.4, these two cases are compared pictorially. For each column, the time axis runs downwards. In the instantaneous case (left side), all of the nucleation occurs before the first slide. As time advances, each island grows larger, but no new ones are nucleated. In the progressive case (right side), some islands have already nucleated before the first slide. However, islands continue to be nucleated even as their older siblings grow larger.

6.5 Characteristic Nucleation Time

Thus, we expect that as we quench deeper and deeper into the incommensurate phase, the transition will occur ever more rapidly. To test this hypothesis, we performed a series of voltage step measurements in which the applied potential was stepped from 200 mV (within the commensurate phase) to varying potentials within the incommensurate phase. As in the previous measurement, we measured the scattered intensity at the incommensurate overlayer peak position as a function of time. This corresponds to a series of experiments similar to the one shown in figure 6.1, but varying the value of the more positive voltage. This is shown in figure 6.5.

We characterized the resulting transition time by fitting the x-ray intensity profiles (which resemble figure 6.1c) to a trapezoidal functional form, as shown in figure 6.6. While this model describes the data quite well, we ascribe no profound significance to it. Rather, we use it simply to define a characteristic time, τ, which should be inversely proportional to k_N. The inset to figure 6.7 plots the resulting τ values. The characteristic time scale describing the ordering of the bilayer ranges varies from 50 seconds for shallow quenches to 0.7 seconds for deep ones. Figure 6.7 illustrates the exponential dependence of τ on $1/\eta$. This fits Eq. (6.6) with $d = 2$, over the entire phase region. The linear slope demonstrates that the growing islands

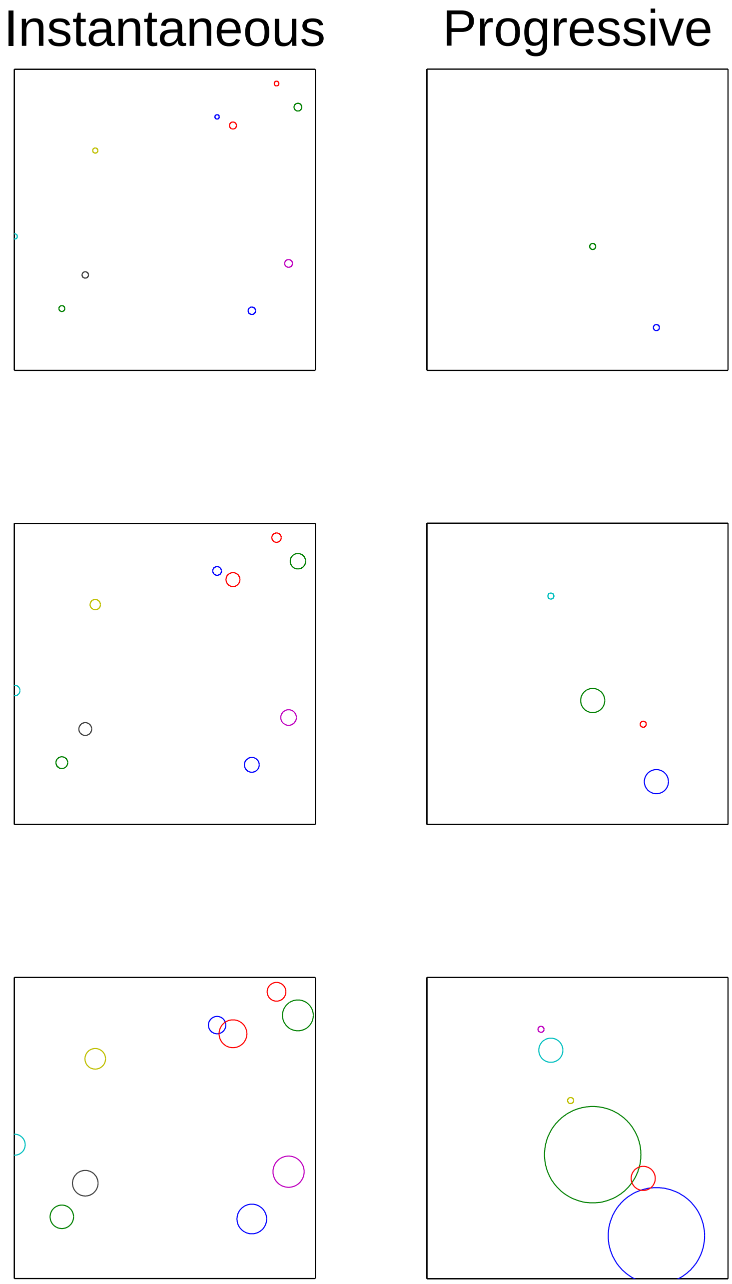

Figure 6.4: Cartoon contrasting progressive and instantaneous nucleation.

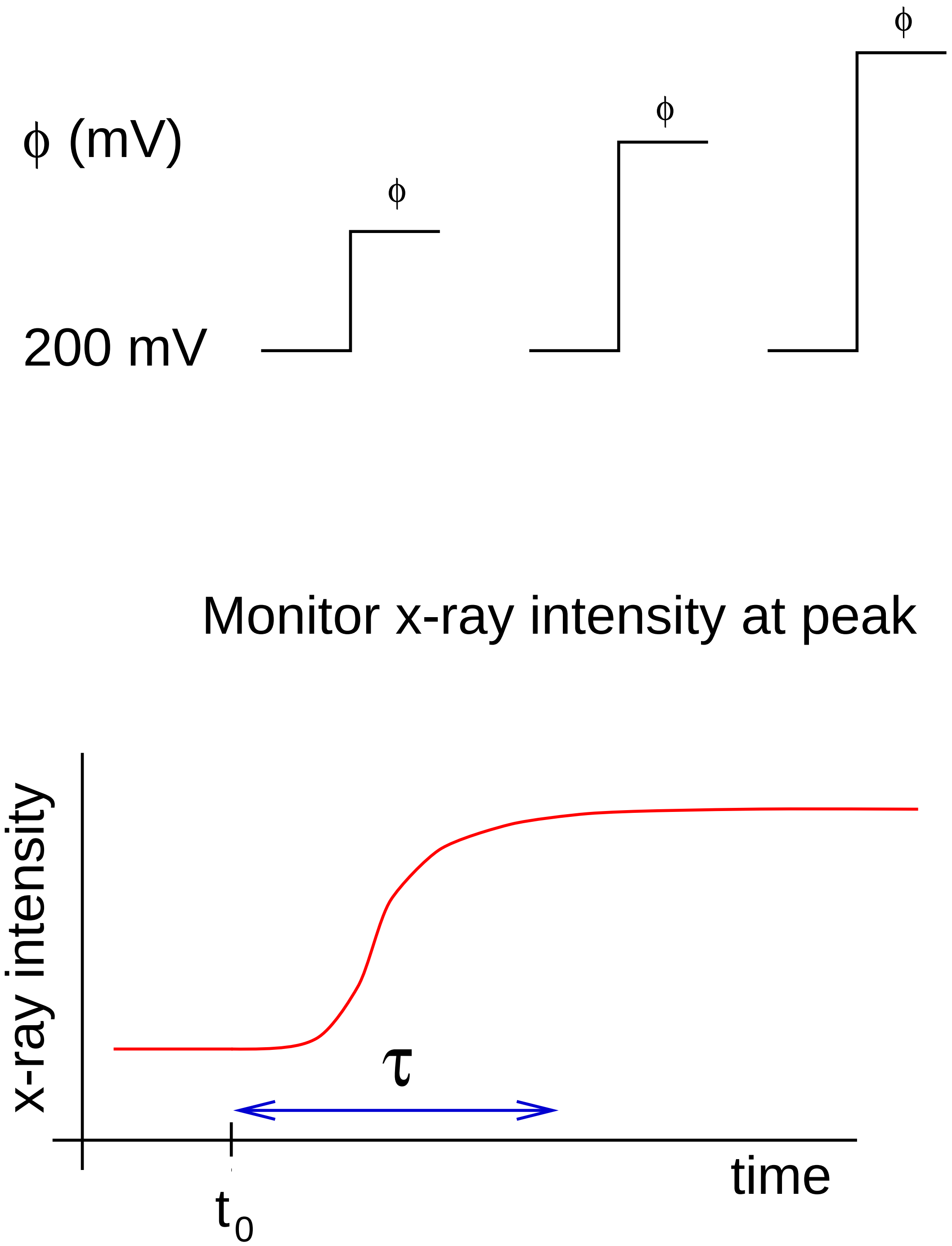

Figure 6.5: Diagram of voltage-quench experiments.

are intrinsically two-dimensional (rather than three-dimensional mounds or pits on the surface) and that these islands are compact rather than fractal. The broad range of τ also implies that our two-dimensional cell geometry has not inhibited the nucleation processes, but is only limited by the accessible range of voltage values. Furthermore, in all cases, τ is longer than the current transient indicating that capacitive charging effects are not dominating our results.

6.6 q–t Data

Now we turn our attention to the development of order in the incommensurate structure formed after desorption. In order to understand the kinetics of this ordering process, we need to access the full $\mathbf{q}$–t dependent x-ray scattering. We repeat the time-resolved measurement of figure 6.1 for a series of $\mathbf{q}$-points linearly spaced along the same $\mathbf{q}_\perp$ direction as shown in figure 5.12. An example of such a measurement is shown in figure 6.8. The first thing to note is that the peak remains centered at a constant value of $\mathbf{q}$, ruling out the possibility that the overlayer simply shifts its periodicity in response to the change in potential.

From the discussion in section 5.5, the correlation length is obtained from the width of the diffraction peak and is believed to be determined by the finite size of growing islands of Cu–Cl. The diffraction peak narrows with time, indicating that these islands are growing. The total coverage is proportional to the integrated intensity.

Ideally, we would collect a $\mathbf{q}$–t data set for each ϕ voltage transition. However,

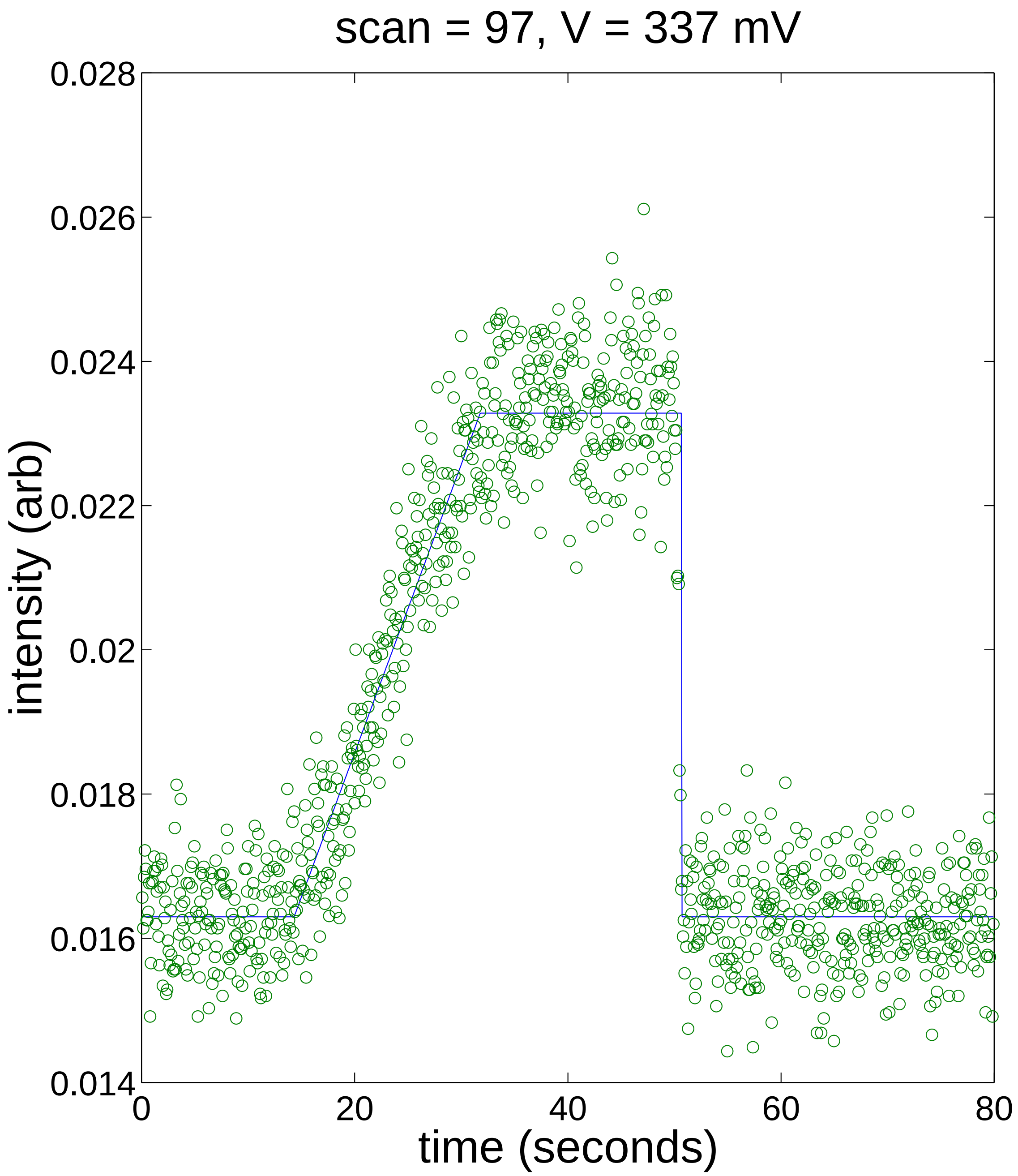

Figure 6.6: Typical trapezoidal fit

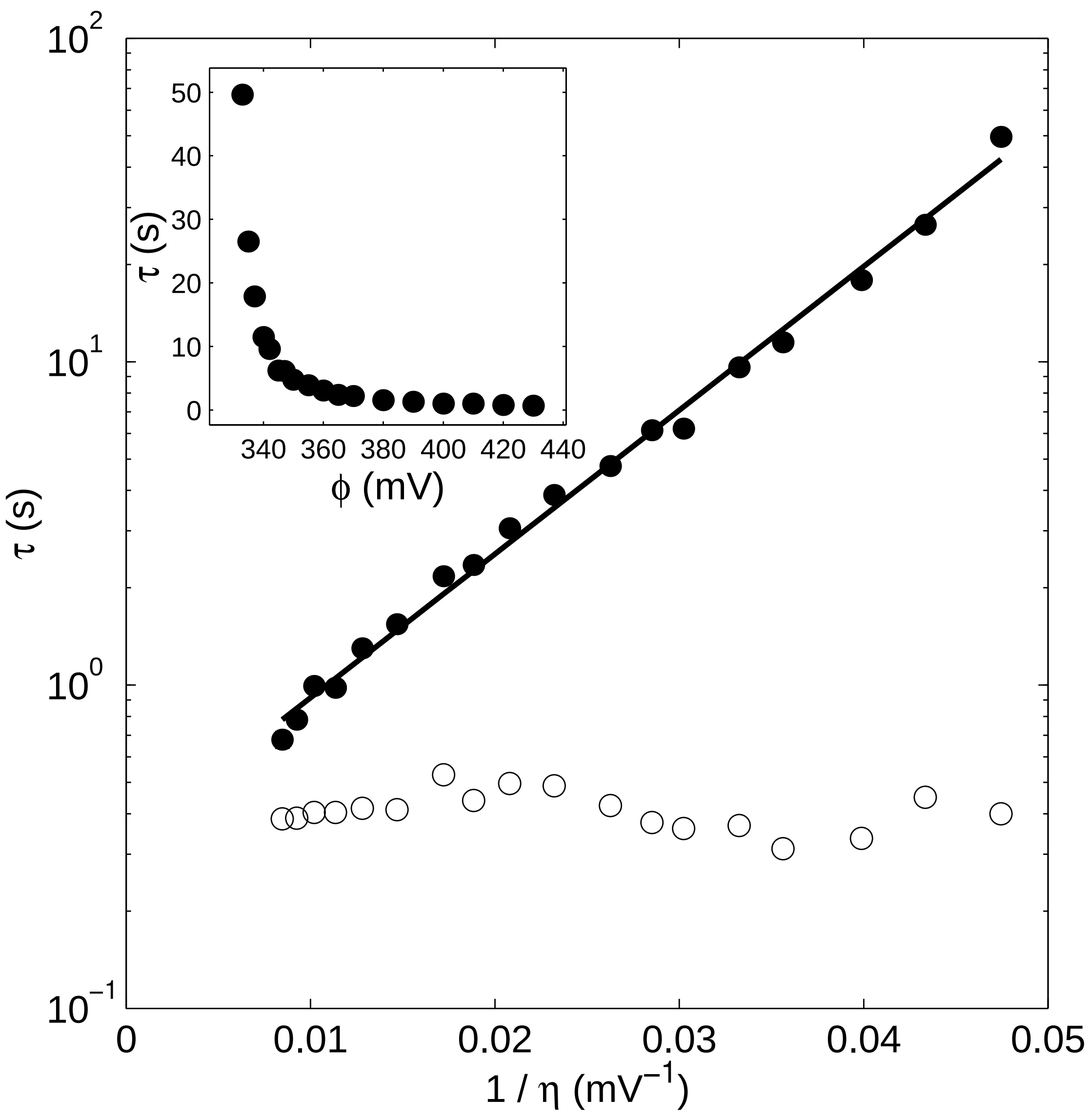

Figure 6.7: Characteristic rise time τ vs. applied voltage. Solid points represent x-ray transition times, while hollow points represent the time scale for the desorption current transient to fall to 5% of its peak value. The straight line is a fit to the nucleation model (6.8) with $d = 2$. Inset: τ on linear scale.

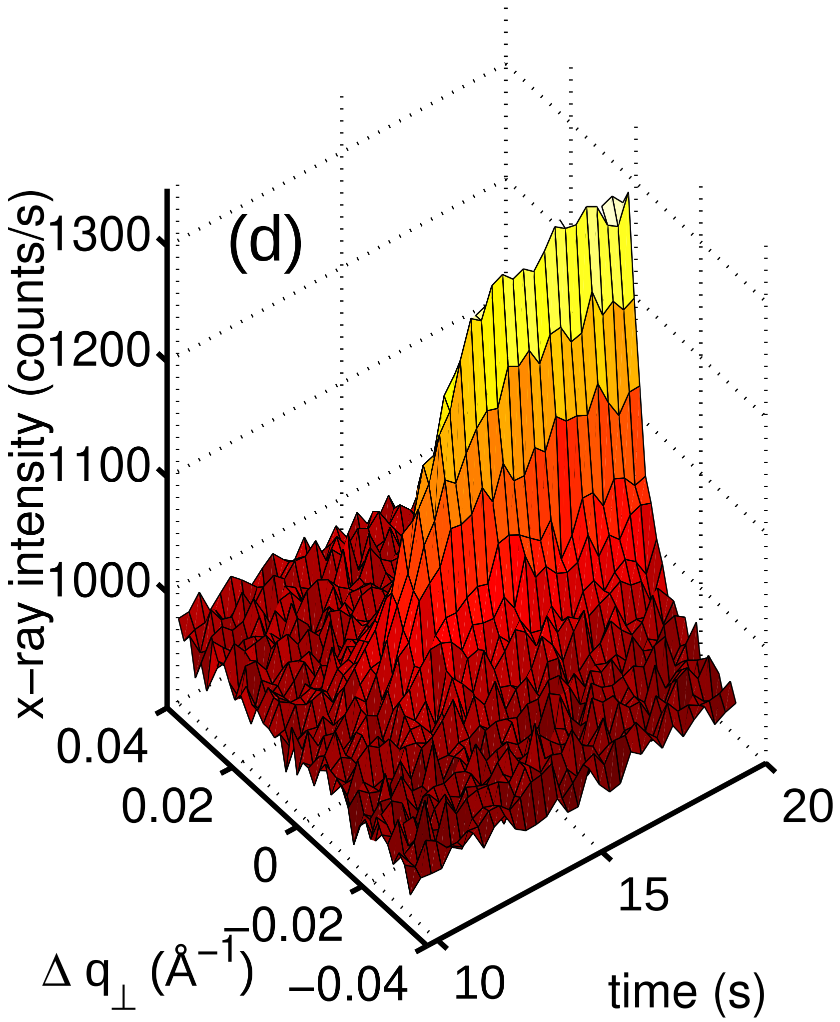

Figure 6.8: Scattered intensity as a function of time t and transverse scattering vector, $\mathbf{q}_\perp$, with a false gray-scale indicating intensity. Time bins have been merged for clarity.

the single data set shown in figure 6.8 consumed 29 hours of synchrotron beam time. With our constraints, it was not feasible to consider collecting many data sets during that beam time allocation.

Because x-ray intensities obey Poisson counting statistics, for a measured signal intensity N, the standard deviation is $\sqrt{N}$. As seen in figure 6.8, the maximum signal in 1300 counts/second, while the background is 1000 counts/second. Because of this high background, we must count for long periods of time to resolve the signal.

6.7 Growth of Two-Dimensional Islands

Up to now, we have discussed the number of islands, but not the total volume comprising this phase. As shown in section 6.5, the islands are intrinsically two-dimensional. This is not intuitively pleasing, since the bilayer itself is two-dimensional. Anticipating this result, in this section we will limit ourselves to the case of two-dimensional islands.

Assume that each island grows by the incorporation of atoms into its boundary, and that this is the rate-limiting step for island growth. Then, for an island of N atoms and radius r, $dN/dt = k_g 2\pi r$. This defines k_g, the rate constant for individual island growth, which has units of [length $\times$ time]$^{-1}$. The area of the island is simply $A = N/\rho$. Since (for a circular island) we have $A = \pi r^2$, we have two expressions for dA/dt:

$$\frac{dA}{dt} = 2\pi(k_g/\rho)r = 2\pi r\frac{dr}{dt} \tag{6.10}$$

which implies that $r(t) = (k_g/\rho)t$ and the area is

$$A(t) = \pi(k_g/\rho)^2 t^2 \tag{6.11}$$

Note that we are assuming that N_{crit} is much smaller than the mean island size. Otherwise A should have a nonzero value at $t = 0$.

6.8 Avrami Theorem

Following Avrami [14, 15, 16] consider a brief example of an area A with N circular islands, each of area a. The extended coverage is $\theta_{\text{ext}} = Na/A$. Of course, if the circles are placed randomly, then they will overlap somewhat and the true coverage θ will be less than the extended coverage θ_{ext}. While the true coverage is bounded by the limits $\theta = 0$ (no coverage) and $\theta = 1$ (complete coverage), the extended coverage can be infinite.

The probability that a particular point on the surface is **not** covered by a particular circle $(1 - a/A)$. So the probability that it is not covered by any of N circles is $(1-a/A)^N = (1-(Na/A)/N)^N$. Assume that $a \ll A$. Then in the limit $N \to \infty$ and using $\lim_{N\to\infty}(1-x/N)^N = e^{-x}$, this probability becomes $\exp(-Na/A) = \exp(-\theta)$. Finally, the probability that a point is covered (which is just the "coverage" θ) is

$$\theta = 1 - \exp(-\theta_{\text{ext}}) \tag{6.12}$$

Using this assumption, we can find the total surface coverage from the "extended" coverage (that is, the coverage if there were no overlap of islands.) As $\theta_{\text{ext}} \to \infty$, $\theta \to 1$.

6.9 Extended Coverage

In this section, I combine results from sections 6.7 and 6.8 to derive some simple expressions for the extended coverage.

In general,

$$\theta_{\text{ext}} = \sum_{i}^{N(t)} A(t - t'_i) \tag{6.13}$$

where i is an index running over all the nuclei, and each island i is nucleated and starts growing at t'_i. We can also change the sum from i to t' and write this as

$$\theta_{\text{ext}} = \int_0^t dt' X(t') A(t - t') \tag{6.14}$$

where the multiplicity $X(t')$ is simply $dN(t')/dt'$. For our special cases, this is $2N_\infty \delta(t')$ (instantaneous) and $N_\infty k_N$ (progressive). [1]

In the instantaneous limit, we have N_∞ nuclei that have all nucleated at $t = 0$, so the extended coverage is

$$\theta_{\text{ext}}^{\text{instantaneous}} = \pi N_\infty \left(\frac{k_g}{\rho}\right)^2 t^2 \tag{6.15}$$

In the progressive limit, we have a constant $dN(t')/dt'$ that we can substitute into (6.14) to obtain

$$\theta_{\text{ext}}^{\text{progressive}} = \frac{\pi}{3} N_\infty k_N \left(\frac{k_g}{\rho}\right)^2 t^3 \ . \tag{6.16}$$

From the previous form of $N(t)$ (6.9) we can compute the exact extended coverage

$$\theta_{\text{ext}} = \pi N_\infty k_N (k_g/\rho)^2 \int_0^t dt' e^{-k_N t'} (t - t')^2 \ . \tag{6.17}$$

[1] The factor of two for the instantaneous case is required by the definition of the δ-function, which runs from $-\infty$ to ∞.

Solving the integral, this becomes

$$\theta_{\text{ext}} = \pi N_\infty \left(\frac{k_g}{k_N \rho}\right)^2 \left[k_N^2 t^2 - 2k_N t + 2 - 2e^{-k_N t}\right] \ . \tag{6.18}$$

In the two limits, this correctly reduces to the progressive and instantaneous cases.

From the coverage alone, it is not possible to determine all of these parameters individually. At best, in the intermediate cases, we can find the variables k_N and the ratio $\alpha \equiv N_\infty (k_g/\rho)^2$. In the progressive case, we cannot even determine these two variables independently, but only their product. It is important to note that $\theta_{\text{ext}}^{\text{instantaneous}}$ is insensitive to k_N, and so fits to (6.18) will also be insensitive to k_N when that limit is approached. This is reasonable, as all the nuclei have already formed before the time scale of observation.

6.10 Analysis of q–t Data

To begin the analysis of the data in figure 6.8, we fit each time slice to a Lorentzian line shape. A Lorentzian is the lowest order approximation to the structure factor for any system with only short range positional order. Some representative time slices and fits are shown by the thin lines in figure 6.9. From these fits, we extract the half-width at half-maximum (Δ) and integrated intensity vs. time. These are shown as circles in figure 6.10b. As expected for growing islands, Δ decreases with time. At the same time, the integrated intensity (proportional to the coverage) grows monotonically.

We can continue our analysis by incorporating the simple nucleation and growth model considered previously. Instead of fitting each time-slice independently, we

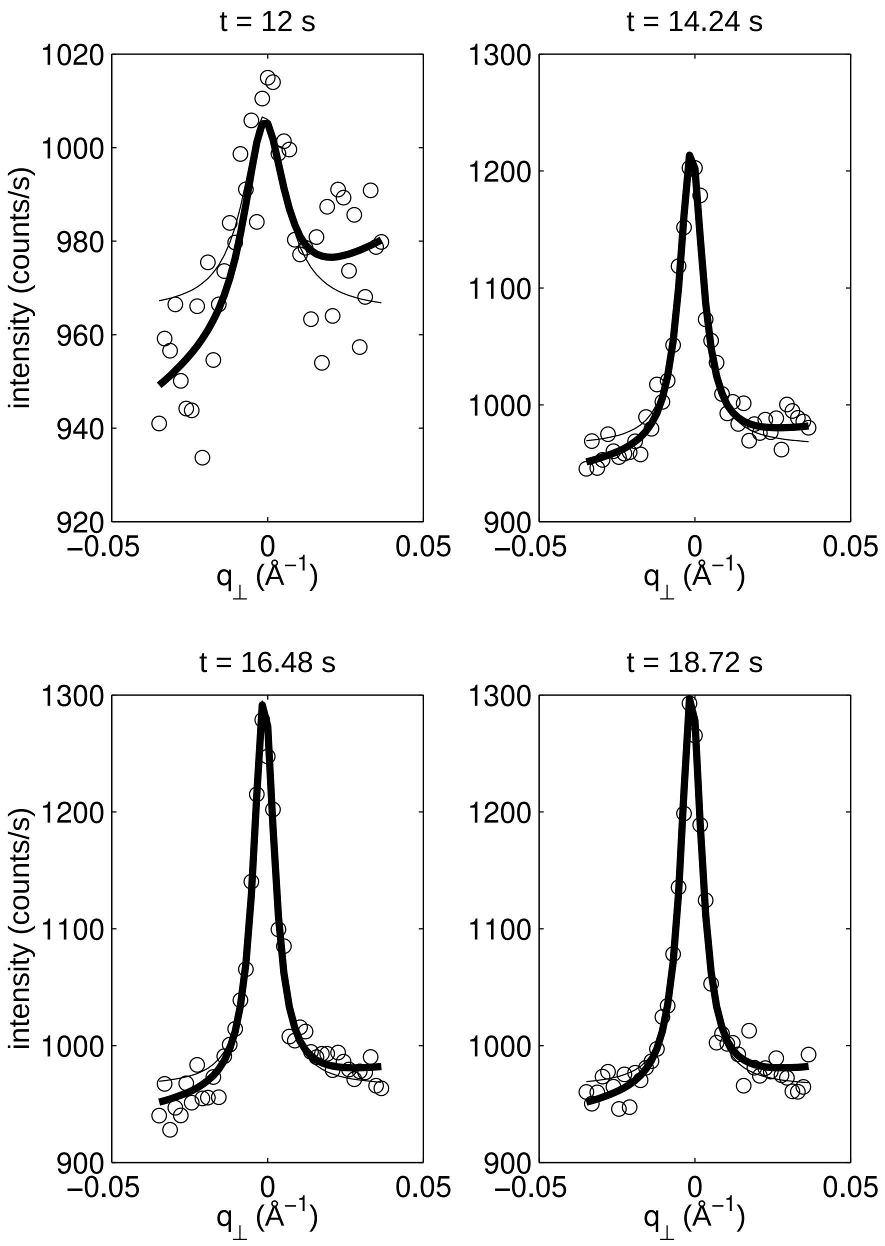

Figure 6.9: Fits of data in figure 6.8 at representative times $t = 12$, 14.24, 16.48, and 18.72 seconds. The thin lines are from fits to the individual slices, while the thick lines are from the fit to (6.23).

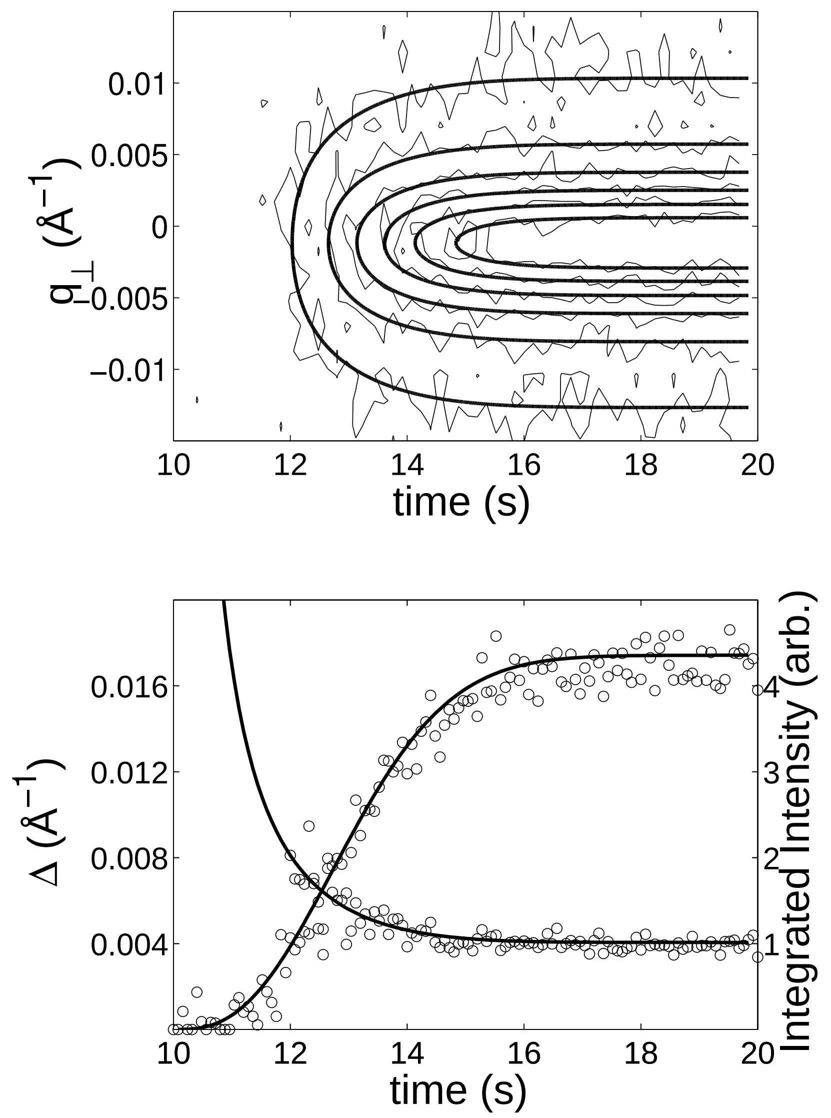

Figure 6.10: (a) Contours of constant intensity of the data set (thin lines) in figure 6.8 and from the best fit to (6.23) (thick lines). (b) Best fit results for the half-width at half-maximum (Δ; descending) and the integrated intensity (I_0; ascending) vs. time. Circles are for separate Lorentzian fits to each time slice and the solid lines are from a fit to (6.23).

now want to fit the entire data set from figure 6.8 with a simple function of few parameters. This intensity function $I(\mathbf{q}, t)$ we choose should satisfy the following conditions.

First, $I(\mathbf{q}, t)$ has a Lorentzian line shape at any fixed time t. This Lorentzian function is written

$$L(I_0(t), \Delta(t), \mathbf{q}_0; \mathbf{q}) = \frac{1}{\pi\Delta(t)} \frac{I_0(t)}{1 + \frac{(\mathbf{q}-\mathbf{q}_0)^2}{\Delta(t)^2}} \tag{6.19}$$

where I_0 is the integrated intensity, Δ is the half-width at half maximum, and $\mathbf{q}_0$ is the peak position in $\mathbf{q}$. Second, the integrated intensities $I_0(t)$ are proportional to the coverage $\theta(t)$. This coverage follows the Avrami form (6.12)

$$\theta = 1 - \exp(-\theta_{\text{ext}}) \tag{6.20}$$

where

$$\theta_{\text{ext}}(t) = \pi N_\infty \left(\frac{k_g}{k_N \rho}\right)^2 \left[k_N^2 t^2 - 2k_N t + 2 - 2e^{-k_N t}\right] \tag{6.21}$$

was given by (6.18). Third, the half-width at half-maxima $\Delta(t)$ depend on the mean island size. The individual length scale of each island i should be a function only of the island growth rate k_g and elapsed time for growth $t - t_i'$. However, the average length scale will in general be a complicated function of several parameters. Defining the average island size as $\langle A \rangle = \theta/N$, we expect that the typical correlation length ξ_{typ} will be proportional to $\langle A \rangle^{1/2}$ and inversely proportional to Δ. So we constrain $\Delta(t)$ to be

$$\Delta(t) = \sqrt{C_N N(t)/\theta(t)} \tag{6.22}$$

with the proportionality constant C_N.

Combining (6.19), (6.20), (6.21), and (6.22), the two-dimensional model function is

$$I(\mathbf{q},t) = C_I L(\theta(t), \Delta(t), \mathbf{q}_0; \mathbf{q}, t) + b_0 + b_1(q - q_0) \tag{6.23}$$

where C_I is just a proportionality constant relating coverage and x-ray intensity, and b_0 and b_1 parameterize the linear background.

We can now re-fit the entire data set (2×10^4 points) shown in figure 6.8 to the single function (6.23). The best fit to this simple model produces $\chi^2 = 1.04$. The intensities from the model and the data are compared in figure 6.11, and appear to agree. However, it is easier to compare the contours of constant intensity that are shown in figure 6.10a. The contours of constant intensity for the model and the data agree very well. The generated integrated intensity $I_0(t)$ and $\Delta(t)$ functions are plotted as solid lines in figure 6.10b. They agree with our previous results (plotted as circles) where each time slice was fit independently. Returning to figure 6.9, we can also compare the intensities from the two-dimensional model (thick lines) with our previous results (thin lines) and the data itself (circles). Both of the lines fit the data quite well; the minor discrepancies between them are due to a difference in the form of the background function. In sum, these kinetic data are well-described as the nucleation and growth of a two-dimensional film.

All of the fit parameters are shown in table 6.1; the physically interesting ones are summarized in the top portion. The initial time t_0, against which times t are measured, was allowed to float above 10 seconds (when the voltage was stepped), but fit to 10 seconds. There seems to be no time delay before the nucleation process begins. The growth parameter $N_\infty(k_g/\rho)^2$ is a product of various parameters

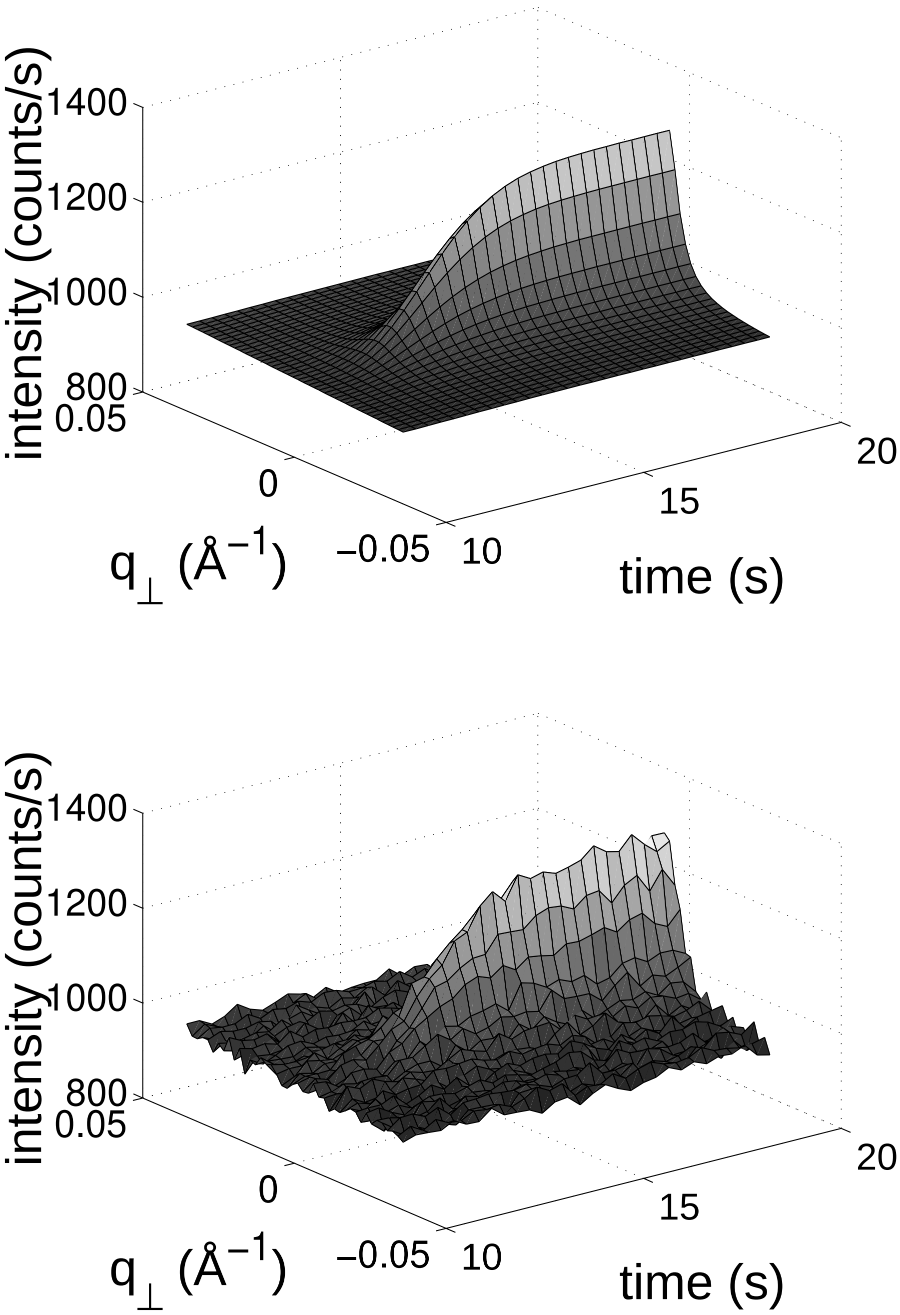

Figure 6.11: Comparison of (top) intensity generated from a fit to (6.23) with (bottom) measured x-ray intensity; time bins have been merged for clarity.

Table 6.1: Parameters obtained from fits to figure 6.8. The physically interesting parameters are shown in the top portion, and the remainder are shown in the bottom portion.

parameter	variable	fit value	units
initial time	t_0	10.0 ± 0.32	s
growth parameter	$N_\infty (k_g/\rho)^2$	0.0404 ± 0.0069	Å^2 s^{-2}
saturation island number	$C_N N_\infty$	$1.644 \times 10^{-5} \pm 3.2 \times 10^{-7}$	Å^{-2}
nucleation rate constant	k_N	1.33 ± 1.33	s^{-1}
peak intensity coefficient	C_I	4.367 ± 0.035	arbitrary
peak position	$q_\perp$	$-0.00117 \pm 3 \times 10^{-5}$	Å^{-1}
background constant	b_0	962.1 ± 0.4	counts s^{-1}
background slope	b_1	443 ± 14	Å counts s^{-1}

from (6.21) that cannot be separated. The saturation island number N_∞ is likewise coupled with a proportionality factor that cannot be isolated. From the uncertainties shown in the table, all of the fit parameters are well-determined except for k_N, to which the fit is relatively insensitive. This is an indication that either the data at early times (when there is very low signal) is insufficient to fix this parameter, or that the observations are in the instantaneous limit (6.15), where θ does not depend on k_N.

We have attempted to test the assumption of first-order nucleation kinetics.

Rearranging (6.9), we have

$$k_N t = \ln\left(\frac{N_\infty}{N_\infty - N(t)}\right) \tag{6.24}$$

and noting from (6.22) that $N \propto \Delta^2\theta$, we obtain

$$k_N t = \ln\left(\frac{\Delta^2(\infty)\theta(\infty)}{\Delta^2(\infty)\theta(\infty) - \Delta^2(t)\theta(t)}\right) \tag{6.25}$$

where $\Delta(t = \infty)$ and $\theta(t = \infty)$ are the saturation values. If the first-order assumption given by (6.9) is correct, then a plot of the right-hand side of (6.25) vs. t should be linear and provide a measure of k_N. This plot is shown in figure 6.12. Unfortunately, the noise in our data makes such a determination inconclusive. Better data may be able to prove or disprove this hypothesis.

6.11 Density-Driven Nucleation and Growth Kinetics

Previously, we posited a voltage-dependent Gibbs free energy (6.6). For the case of two-dimensional circular clusters,

$$\Delta G_{\text{crit}} = \frac{(\gamma a)^2}{4ze\eta} = \frac{\gamma^2\pi}{\rho ze\eta} \tag{6.26}$$

where we have solved (6.4) for the geometrical constant $a = 2\sqrt{\pi/\rho}$. One way to obtain this form is to assume (as Schmickler [117] does) the deposition of metal ions from solution M^+_{sol} directly into a crystalline phase on the surface M_{cry}, as shown by the right side of figure 6.13.

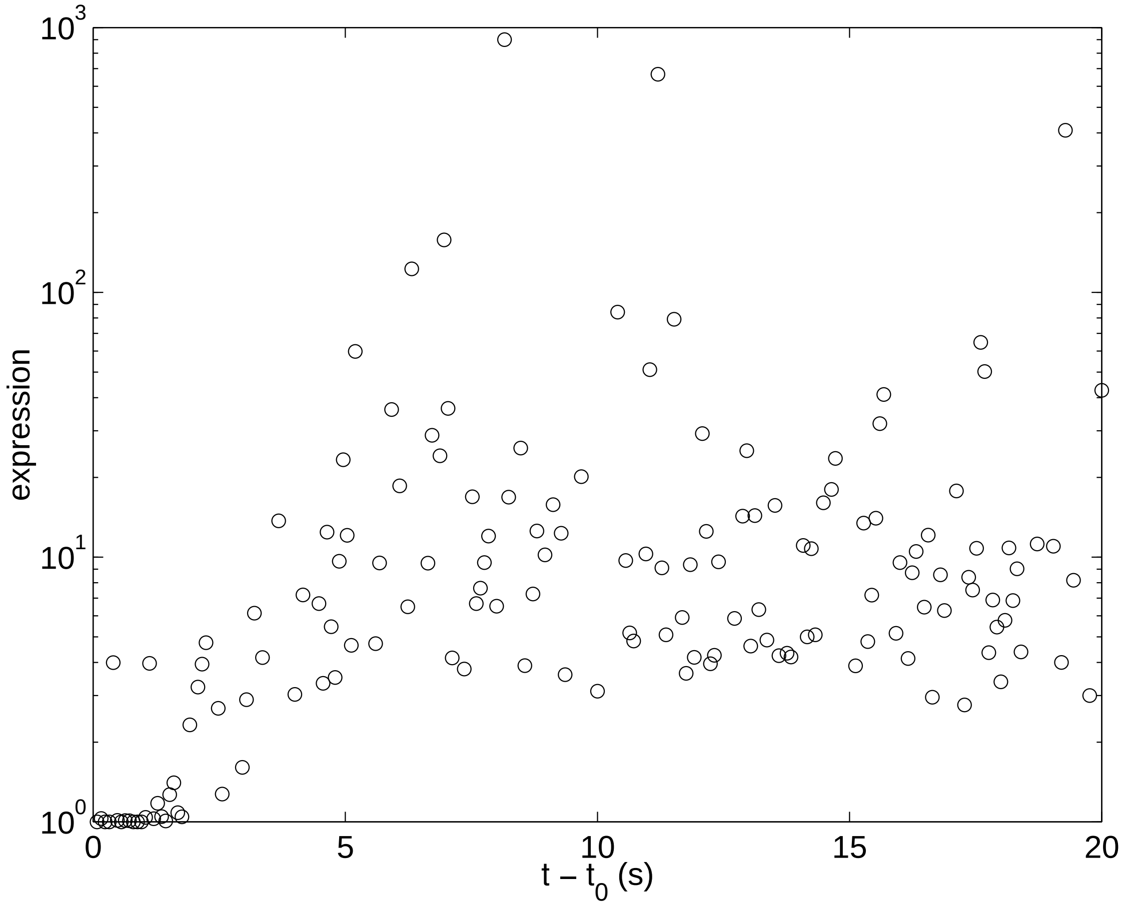

Figure 6.12: Plot of the expression on the right-hand side of (6.25) vs. t. The noise in the y-values are primarily due to the uncertainty in $\Delta(t)$, and make a test of (6.25) impossible.

In this section, an alternative route to obtaining (6.26) is demonstrated. (This treatment was initially developed by Joel Brock [48].) Consider a model in which adsorption (described by a Langmuir isotherm) is driven by the change in potential. As the potential is varied the coverage varies, and the increasing coverage then drives a conventional phase transition. This is shown by the left side of figure 6.13. This density-driven phase transition may occur well before the adsorption transition is completed, in which case the system may still be in the linear region of the Langmuir isotherm (2.59).

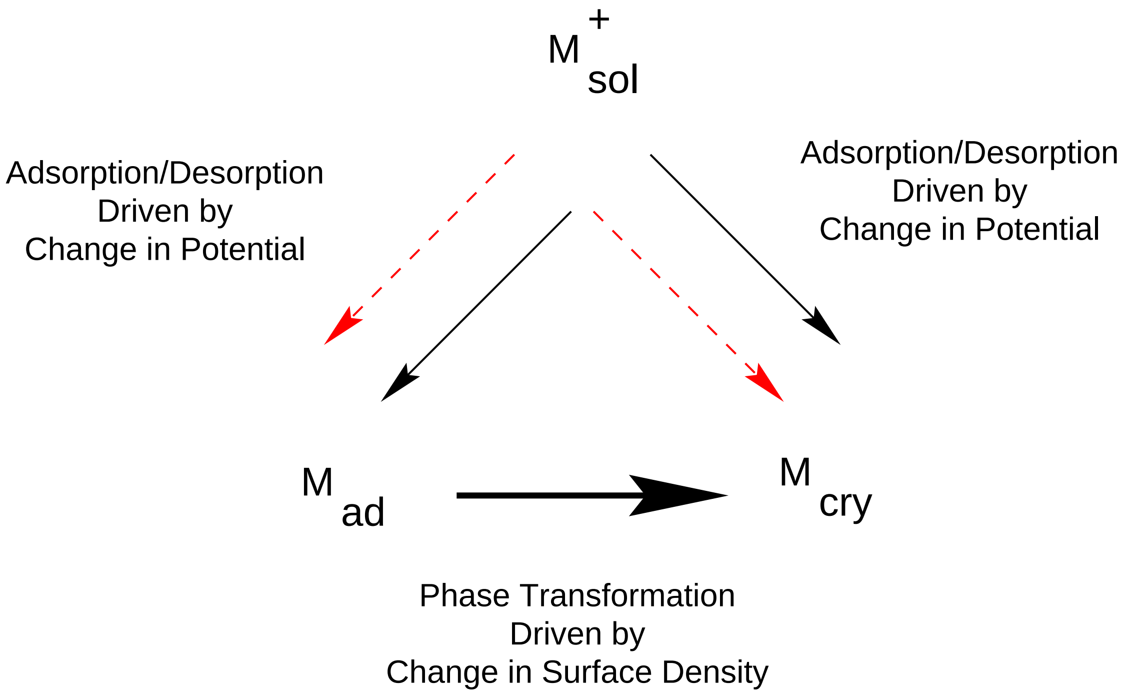

Figure 6.13: Schematic of two possible deposition processes. The solid lines represent mass flow (particle transfer) and dotted lines represent current flow (charge transfer).

Upon the formation of a circular cluster with radius r, the Gibbs free energy of the system changes by ΔG. ΔG has contributions from the difference of chemical potentials of the lattice phase μ_{lat} and disordered adsorbed phase μ_{ad} and from the surface energy.

$$\Delta G = \pi r^2 \rho \left(\mu_{lat} - \mu_{ad}\right) + 2\pi\gamma r \tag{6.27}$$

where ρ is the atom/area density in the lattice phase (section 6.7), and γ is the energy per unit length of the interface (section 6.3). Setting $\partial \Delta G / \partial r = 0$ we obtain the critical radius r_c,

$$r_c = \frac{\gamma}{\rho(\mu_{ad} - \mu_{lat})} \ . \tag{6.28}$$

For simplicity, treat the adsorbed phase as an ideal gas. Define P_r to be the pressure at which a circular nucleus of radius r is in equilibrium with the gas phase. At P_∞, $\mu_{ad} = \mu_{lat}$. At P_r, $\mu_{ad} - \mu_{lat} = \frac{\gamma}{\rho r}$. From thermodynamics we have

$$dg = -s\, dT + \frac{1}{\rho}\, dP \tag{6.29}$$

where g and s are the Gibbs energy and entropy per particle. In equilibrium, $(dg)_{ad} = (dg)_{lat}$ so at constant temperature we obtain,

$$(1/\rho_{ad} - 1/\rho)\, dP = -\frac{\gamma}{\rho r^2}\, dr \tag{6.30}$$

Now assume that $\rho_{ad} \ll \rho$ and use the ideal gas law $P = \rho_{ad} kT$.

$$kT \frac{dP}{P} = -\frac{\gamma}{\rho r^2}\, dr \tag{6.31}$$

Integrating from ∞ to r_c (P_∞ to P_{r_c}),

$$kT \ln\left(\frac{P_{r_c}}{P_\infty}\right) = \frac{\gamma}{\rho r} \tag{6.32}$$

and using this value of r_c in (6.27),

$$\Delta G_c = \frac{\pi\gamma^2}{kT\rho \ln\left(P_{r_c}/P_\infty\right)} \,. \tag{6.33}$$

Using the ideal gas relation again, $P = \Gamma kT$, where Γ is the surface excess concentration (section 2.8) of the adsorbed phase. Then,

$$\frac{P_r}{P_\infty} = \frac{\Gamma_r}{\Gamma_\infty} = \exp\left(-ze\eta/kT\right) \tag{6.34}$$

where the latter equality assumes a linearized isotherm (2.59). Substituting into (6.33),

$$\Delta G_c = \frac{\pi\gamma^2}{\rho ze\eta} \tag{6.35}$$

which duplicates (6.26) exactly. Therefore, in this limit of low coverages, the energy barrier for a density-driven phase transition and the potential-driven phase transitions are identical. The primary difference is that the current transfer precedes the nucleation and growth in a density-driven transition, while the two processes occur in tandem in a potential-driven phase transition. The wide separation in time scales between the current transient and the onset of ordering (section 6.2 and figure 6.1) indicate a density-driven transition.

6.12 Step Chronoamperometry of an Ideal System

In section 2.5.2, we considered the electrode to be a perfect sink for ions: any ions that arrive at $z = 0$ are deposited onto the electrode irreversibly. This is the meaning of the boundary condition (2.45)

$$c(z = 0^+, t > 0) = 0 \tag{6.36}$$

which is reasonable for bulk diffusion where the deposition kinetics are very fast, and so the rate-limiting step is the diffusion of ions to the electrode surface.

However, this is not a reasonable approximation for UPD. Firstly, the coverage θ will not exceed unity. Secondly, the kinetics of deposition can not be neglected. As in section 5.2.1, a simple model is one with a Langmuir isotherm. We will make a further assumption, that we can linearize the Langmuir isotherm, as in (2.59),

$$\theta \approx c \exp\left(-\frac{\Delta G_0}{kT}\right) \tag{6.37}$$

where we are now keeping only the linear term. This will be adequate for sufficiently low coverages, and has the advantage of simplicity. In the particular Cu/Cl/Pt(111) UPD system studied in this dissertation, a phase transition occurs once the coverage reaches a certain point. So the behavior will deviate from the Langmuir result in that case, anyway.

The treatment follows the derivation of the Cottrell equation (section 2.5.2). We arrive at the same result as (2.48),

$$c(z,s) = A(s)\exp\left[(s/D)^{1/2}z\right] + B(s)\exp\left[-(s/D)^{1/2}z\right] + c_\infty/s \tag{6.38}$$

where $A(s) = 0$ because $c(z \to \infty, t) = c_\infty$. The boundary condition at $z = 0$ is not $c(z = 0^+, t > 0) = 0$ as for the Cottrell equation. To complete the solution, we need to find the appropriate boundary condition. (The following mathematics are borrowed from [48].)

The surface excess is

$$\Gamma(t) = \int_0^t dt' D \left.\frac{\partial c(z,t')}{\partial z}\right|_{z=0} \tag{6.39}$$

and its Laplace transform is

$$\Gamma(s) = \left(\frac{D}{s}\right) \left.\frac{\partial c(z,s)}{\partial z}\right|_{z=0} . \tag{6.40}$$

Using (6.37), we can relate Γ to the concentration,

$$\Gamma(t) = \Gamma_{\text{sat}}\theta = \Gamma_{\text{sat}}\, c(z=0,t) \exp\left(-\frac{\Delta G_0}{kT}\right) . \tag{6.41}$$

Defining $b(t) = \Gamma(t)/c(t)$ we can substitute (6.38) into (6.41) and Laplace transform to obtain

$$\Gamma(s) = b\left[B(s) + \frac{c_\infty}{s}\right] . \tag{6.42}$$

Similarly, substituting (6.38) into (6.40) we obtain

$$\Gamma(s) = -\left(\frac{D}{s}\right)^{1/2} B(s) . \tag{6.43}$$

Now we can equate (6.42) and (6.43) and solve for $B(s)$:

$$B(s) = -\frac{b\, c_\infty}{b\, s + (Ds)^{1/2}} . \tag{6.44}$$

We now substitute (6.44) into our previous solution (6.38), and obtain the Laplace transform of $c(z,t)$.

$$c(z,s) = -\frac{b\, c_\infty}{b\, s + (Ds)^{1/2}} \exp\left[-(s/D)^{1/2} z\right] + \frac{c_\infty}{s} . \tag{6.45}$$

We can now obtain the current density by substituting (6.45) into Fick's Law (2.35):

$$j(s) = neD \left.\frac{\partial c}{\partial z}\right|_{z=0} = D\left[-\frac{b\, c_\infty}{b\, s + (Ds)^{1/2}}\right]\left[-\left(\frac{s}{D}\right)^{1/2}\right] = \frac{b\, c_\infty}{b\,(s/D)^{1/2} + 1} . \tag{6.46}$$

The last step is to perform the inverse Laplace transform on (6.46). The following transform [55]

$$\mathcal{L}\left[\frac{1}{\sqrt{\pi t}} - a e^{a^2 t}\mathrm{erfc}\left(a\sqrt{t}\right)\right] = \frac{1}{\sqrt{s}+a} \tag{6.47}$$

completes the solution:

$$j(t) = nec_{\infty}\sqrt{D}\left[\frac{1}{\sqrt{\pi t}} - \frac{\sqrt{D}}{b}\exp\left(\frac{Dt}{b^2}\right)\mathrm{erfc}\left(\frac{\sqrt{Dt}}{b}\right)\right] . \tag{6.48}$$

In the limit that adsorption kinetics play no role ($\Gamma_{\mathrm{sat}} \to \infty$, or $b \to \infty$), then the second term in (6.48) vanishes and we recover the Cottrell current (2.53). Equation (6.48) is plotted in figure 6.14 for various values of b.

6.13 Discussion

The basic scenario is that the applied potential step drives copper off of the surface and the Cu–Cl grains then nucleate and grow. Upon reversal of the potential step, the Cu–Cl bilayer is destroyed as the commensurate copper layer is formed.

From the exponential dependence of the time scale on voltage (figure 6.7), it is now clear why Cu/Cl/Pt(111) cyclic voltammetry (figure 5.2) always shows hysteresis, even for extremely slow sweep rates. Incorporating the nucleation and growth model into the cyclic voltammetry formula should lead to quantitative predictions for the degree of hysteresis as a function of sweep rate. However, it is unlikely that cyclic voltammetry alone would provide sufficient evidence for nucleation and growth; there are many processes that can affect electrode kinetics and cause similar responses. Instead, electrochemists typically study nucleation with chronoamperometry [79, 80].

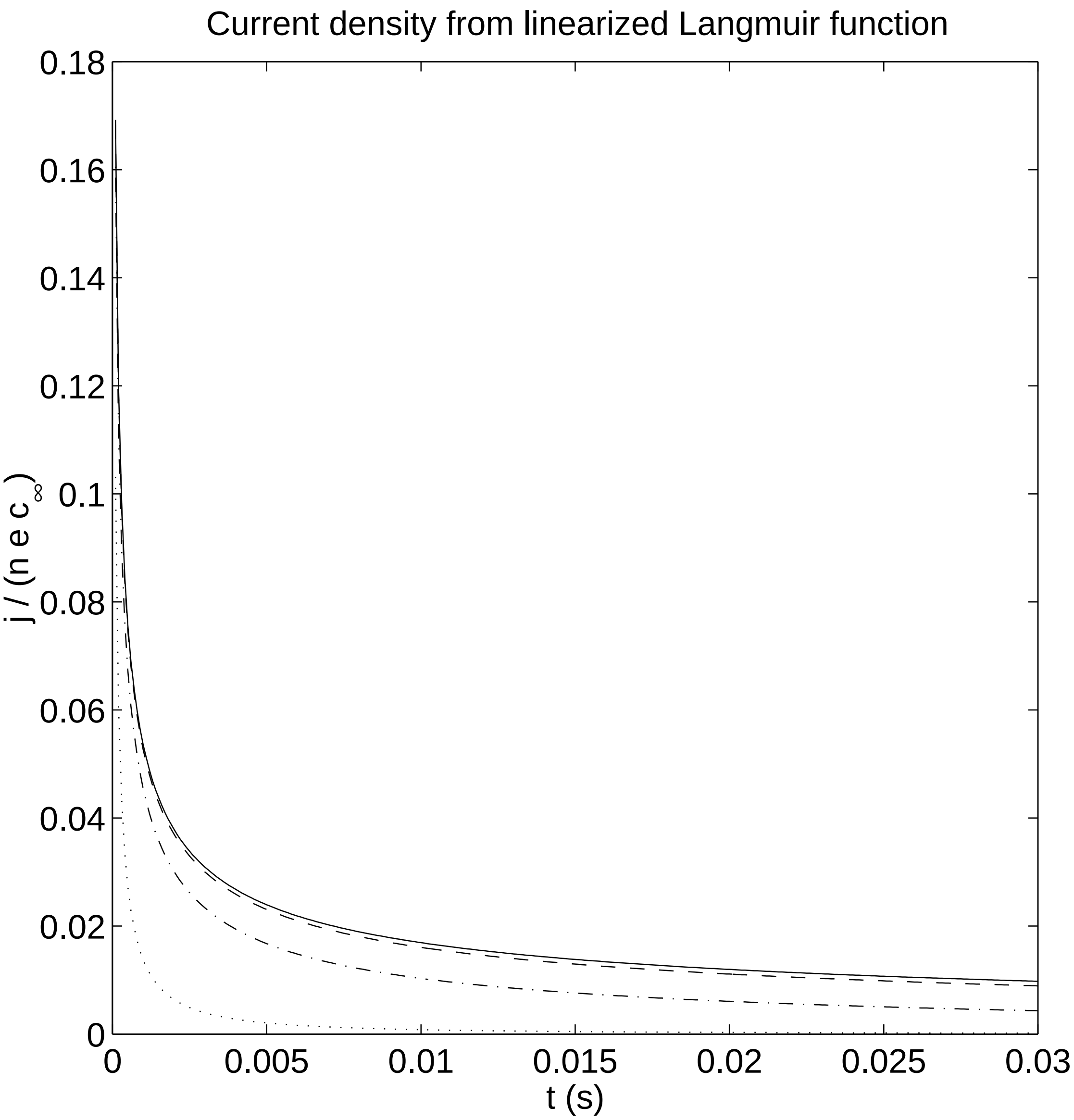

Figure 6.14: Current density at the electrode surface from (6.48) with $b = 0.0001$ (dotted), $b = 0.001$ (dot-dashed), and $b = 0.01$ (dashed). Note that $b = 0.01$ is nearly indistinguishable from the Cottrell result (solid). I have chosen $D = 9 \times 10^{-6}\mathrm{cm}^2/\mathrm{s}$, which is typical of aqueous solutions.

We have carefully considered possible effects of the thin solution layer on the ordering kinetics after a potential step. If the thin-layer were an inhibiting factor, we would expect to find an upper limit to the rate at which the nucleation process could take place. This is not apparent in our data. As shown in figure 6.7, the fastest observable time scale is limited by the constraint that the voltage quench not reach into phase A, beyond the incommensurate phase B. Furthermore, there is no evidence of any roll-over in the voltage dependence of the ordering time constant. Finally, the ordering time constant is always longer than the electronic time constant.

In standard deposition-nucleation problems [117], the voltage dependence in the Gibbs free energy (6.3) is a result of the differing electric potentials in the bulk solution and at the surface of the electrode. In our problem, the incommensurate and commensurate phases are both near the electrode surface. The charge transfer from the platinum surface precedes the ordering and may be voltage dependent. In particular, how much of the charge is shared between the Cu and Cl atoms is unknown. It has been shown that the ionization state does not jump directly from Cu^0 to Cu^{2+} [78, 5]. Another possibility is that the Cu or Cl ions change their positions (especially along the z direction) as a precursor to desorption out of the ordered state. Expanded or compressed layers, which are voltage-controlled, have been observed in several UPD systems.

To resolve these underlying issues, more data on this transition must be acquired. Time-resolved *in situ* reflectivity, both specular and non-specular, would help to clarify the positions and occupancies of the Cu and Cl layers throughout the desorption process. X-ray standing waves, which have been applied to UPD [4, 35, 3], are particularly sensitive to the positions of ordered layers above the electrode surface. It may also be helpful to take data on a related UPD process: Cu on Au(111) in H_2SO_4 [133]. This one of the most studied systems and has been extremely well-characterized. The gold surface is much easier to work with and does not oxidize as readily as platinum, simplifying the sample transfer (section 4.3.7) and subsequent data acquisition.

Scattering from the commensurate overlayer occurs at the same H, K positions as the Pt(111) crystal truncation rods and will be difficult to observe. Thus, experimental information on the reverse reaction, formation of the commensurate layer, will be difficult to obtain.

Finally, a comparison of the electrochemical current transients in the hanging-meniscus cell and the x-ray cell is necessary. Hanging-meniscus data show distinct nucleation bumps that are absent in the x-ray cell. While capacitive charging effects (which are enhanced in the x-ray cell) may mask some features, a systematic study of each would resolve the discrepancy and clarify the voltage dependence in (6.3).

Chapter 7

Conclusions

In conclusion, we have studied a system wherein desorption (rather than deposition) is followed by ordering. The charge-transfer process is much faster than the development of long-range order. The x-ray data are well described by a nucleation and growth model with only a few parameters. The potential-step experiments demonstrate that the rate of ordering agrees well with nucleation models over two decades in time, and is not limited by the thin-layer geometry.

Electrochemistry is a good model system for studying growth phenomena in general. In comparison with *in vacuo* systems, it has the advantage that heteroepitaxial material can be removed to recover the initial substrate. So the same deposition (or desorption) processes can be studied repeatedly, under identical conditions, and without having to change samples. Also, electrochemical systems can be simpler, and components are less expensive, than for ultra-high vacuum systems. This is more practical for traveling to distant locations (such as synchrotrons).

Despite the "conventional wisdom", it is possible to perform good kinetic x-ray measurements in a thin-layer electrochemical cell. The limiting rates are not specifically constrained by the cell itself. Voltammograms of ideal quality are a necessary condition to detecting the x-ray signal. Crystal quality is a determining factor in both voltammetry and the bilayer x-ray scattering. To this end, we developed a polishing / annealing procedure and apparatus that have now propagated to other research groups in Clark Hall.

We have simultaneously measured *in situ* x-ray scattering from the adsorbed incommensurate bilayer and current transients. This allows us to directly address the kinetics of the nonequilibrium desorption/ordering process. Upon a positive voltage step, there is Cu desorption, and the commensurate structure transforms into an incommensurate structure, with a larger in-plane lattice constant. During this process, we see a current transient and the emergence of an x-ray scattering peak. The current transients have two components: the capacitive charging of the double-layer, and the Faradaic charge transfer due to desorption/adsorption of ions. We have not yet been able to separate the two. The x-ray scattering intensity indicates the ordering of the incommensurate bilayer. The rise in integrated intensity is proportional to the increasing number density in the ordered phase. The narrowing of the peak corresponds to a increasing correlation length, which implies growing phase domains.

Using a nucleation and growth model, we can fit the entire $\mathbf{q}$–$\mathbf{t}$ data set (2×10^4 points) to a function of a few variables. Extending these arguments, we demonstrate that the ordering time scales with voltage over the entire range, in quantitative agreement with the nucleation and growth of two-dimensional islands.

All we know about the desorption process is contained in the current transient data. One could better determine when the copper ions leave the surface by performing a similar kinetic x-ray experiment but monitoring the specular reflectivity instead of the intensity of the Cu–Cl order parameter. The information gained would be very interesting; however, the experiment would be a major undertaking, requiring a different cell design and many months of experimenting. Furthermore, the results would not affect the conclusions of the current experiment. Rather, they might shed some light on what happens before the nucleation and growth process begins.

Further studies could explore the relationship between geometry-dependent diffusion processes, charge transfer at the interface, and nucleation mechanisms. Some future experimental directions have already been detailed in section 4.6. Additional chronoamperometric measurements in a cell where the thickness of the solution layer could be systematically varied would allow one to investigate whether the desorption process is diffusion-limited in one limit and reaction-rate-limited in the other. These measurements are also well beyond the scope of the current investigation, requiring new experimental cells and, again, the results would not affect our current conclusions.

Appendix A

Gaussian Distributions

This appendix summarizes some relevant results on Gaussian distributions for the reader who may not be familiar with them.

Consider the cumulant expansion [70] for $\langle e^x \rangle$, where x is considered small. Here, we will only expand to second order, though the extension to higher orders is straightforward. To derive the cumulant expansion, begin with

$$\ln(1+x) = x - x^2/2 + O(x^3) \tag{A.1}$$

for small x and expand the exponential

$$\langle e^x \rangle = 1 + \langle x \rangle + \langle x^2 \rangle/2 + O(x^3) \; . \tag{A.2}$$

Inserting (A.2) into (A.1) we obtain

$$\ln \langle e^x \rangle = \langle x \rangle + \langle x^2 \rangle/2 - \langle x \rangle^2/2 + O(x^3) \; . \tag{A.3}$$

Thus

$$\langle e^x \rangle = \exp\left\{ \langle x \rangle + \frac{1}{2}\left[\langle x^2 \rangle - \langle x \rangle^2 \right] + O(x^3) \right\} \; . \tag{A.4}$$

A "Gaussian random variable" is a random variable with a Gaussian distribution. For a Gaussian random variable x, all of the terms of order x^3 and higher are identically zero. This follows from considering a Gaussian distribution of the form

$$p(x) = \frac{\alpha}{\sqrt{\pi}} \exp\left[-\alpha^2(x-x_0)^2\right] \tag{A.5}$$

which is normalized such that $\int_{-\infty}^{+\infty} dx\, p(x) = 1$. By integrating, it is easy to show that

$$\begin{aligned} \langle x \rangle &= \int_{-\infty}^{+\infty} dx\ p(x)\ x = x_0 \ , && \text{(A.6)} \\ \langle x^2 \rangle &= \int_{-\infty}^{+\infty} dx\ p(x)\ x^2 = x_0^2 + \frac{1}{2\alpha^2} \ . && \text{(A.7)} \end{aligned}$$

Now, the expectation value of e^x is

$$\langle e^x \rangle = \int_{-\infty}^{+\infty} dx\ p(x)\ e^x = \int_{-\infty}^{+\infty} dx\ \frac{\alpha}{\sqrt{\pi}} \exp\left[-\alpha^2(x-x_0)^2 + x\right] . \tag{A.8}$$

The easiest way to solve this is by factoring judiciously to "complete the square" in the exponential:

$$\begin{aligned} \langle e^x \rangle &= \int_{-\infty}^{+\infty} dx\ \frac{\alpha}{\sqrt{\pi}} \exp\left[-\alpha^2(x-x_0)^2 + x\right] && \text{(A.9)} \\ &= e^{x_0} e^{1/(4\alpha^2)} \int_{-\infty}^{+\infty} dx\ \frac{\alpha}{\sqrt{\pi}} \exp\left[-\alpha^2(x-x_0)^2 + (x-x_0) - \frac{1}{4\alpha^2}\right] && \text{(A.10)} \\ &= e^{x_0} e^{1/(4\alpha^2)} \int_{-\infty}^{+\infty} dx\ \frac{\alpha}{\sqrt{\pi}} \exp - \left[\alpha(x-x_0) - \frac{1}{2\alpha}\right]^2 && \text{(A.11)} \\ &= e^{\langle x \rangle} e^{(1/2)\left(\langle x^2 \rangle - \langle x \rangle^2\right)} \ . && \text{(A.12)} \end{aligned}$$

For a Gaussian distribution, all of the terms of the cumulant expansion beyond second order are identically zero. For this reason, the assumption of a Gaussian distribution is equivalent to the assumption that x is sufficiently small (so that terms beyond second order can be neglected).

I mention one more useful relation, used in section 3.10. Assuming that the Gaussian approximation is valid and $\langle A + B \rangle = 0$,

$$\langle e^A e^B \rangle = \langle e^{A+B} \rangle = e^{\frac{1}{2}\langle A+B \rangle^2} = e^{\frac{1}{2}\langle A^2+2AB+B^2 \rangle} \tag{A.13}$$

follows directly from (A.4).

Appendix B

Diffusion Equation

This treatment expands upon the three-dimensional treatment by McQuarrie [99] and extends it to arbitrary dimensionality. McQuarrie actually suggests two ways to give the result (B.14); I am using the first.

The diffusion equation for G is

$$\frac{\partial G(\mathbf{r},t)}{\partial t} = D\nabla^2 G(\mathbf{r},t) \tag{B.1}$$

and we take the initial condition

$$G(\mathbf{r},0) = \delta(\mathbf{r}) \ . \tag{B.2}$$

This can be solved most easily by taking a Fourier transform

$$\frac{\partial G(\mathbf{q},t)}{\partial t} = -Dq^2 G(\mathbf{q},t) \tag{B.3}$$

and the initial condition becomes

$$G(\mathbf{q},0) = 1 \ . \tag{B.4}$$

The solution of this is

$$G(\mathbf{q},t) = \exp(-q^2 Dt) \ . \tag{B.5}$$

The Fourier transform approach is useful in another way. We can differentiate the Fourier transform expression (3.21) twice to find

$$\begin{aligned} \frac{\partial^2}{\partial q^2} G(\mathbf{q},t) &= \frac{\partial^2}{\partial q^2} \int d\mathbf{r}\ e^{-i\mathbf{q}\cdot\mathbf{r}} G(\mathbf{r},t) && \text{(B.6)} \\ &= \frac{\partial^2}{\partial q^2} \int d\mathbf{r}\ e^{-iqr\cos\theta} G(\mathbf{r},t) && \text{(B.7)} \\ &= -\int d\mathbf{r}\ r^2 \cos^2\theta\ e^{-iqr\cos\theta} G(\mathbf{r},t) \ . && \text{(B.8)} \end{aligned}$$

Take the $q = 0$ case,

$$\left. \frac{\partial^2 G(\mathbf{q},t)}{\partial q^2} \right|_{q=0} = -\int d\mathbf{r}\ r^2 \cos^2\theta\ G(\mathbf{r},t) \ . \tag{B.9}$$

The right-hand side of this equation is just $-\langle r^2 \cos^2\theta \rangle$, which can be separated into radial and angular parts $-\langle r^2 \rangle \langle \cos^2\theta \rangle$. The latter factor $\langle \cos^2\theta \rangle$ is just the average value of $\langle x^2/r^2 \rangle$ over a d-dimensional spherical shell. Since the equation of that shell is

$$x^2 + y^2 + z^2 + \ldots = r^2 \tag{B.10}$$

and taking the average value,

$$\left\langle \frac{x^2}{r^2} \right\rangle + \left\langle \frac{y^2}{r^2} \right\rangle + \left\langle \frac{z^2}{r^2} \right\rangle + \ldots = 1 \tag{B.11}$$

then the average value of each component (they are all equivalent) is just $1/d$. Then we have $\langle \cos^2\theta \rangle = 1/d$ and

$$\left. \frac{\partial^2 G(\mathbf{q},t)}{\partial q^2} \right|_{q=0} = -\frac{1}{d} \int d\mathbf{r}\ r^2\ G(\mathbf{r},t) = -\frac{1}{d} \langle r^2 \rangle \ . \tag{B.12}$$

Now, from (B.5) we know that

$$\left.\frac{\partial^2 G(\mathbf{q},t)}{\partial q^2}\right|_{q=0} = -2Dt \tag{B.13}$$

so we can equate these to find the important result

$$\langle r^2(t)\rangle = 2dDt \; . \tag{B.14}$$

where d is the spatial dimensionality. This proves (2.37).

Bibliography

[1] *Henke Atomic Scattering Factors.* http://xray.uu.se/hypertext/henke.html. Other x-ray data is available at http://xray.uu.se.

[2] *NIST Physical Reference Data.* http://physics.nist.gov/PhysRefData/contents.html. Paper version is [53].

[3] H. D. Abruna, G. M. Bommarito, and D. Acevedo. The study of solid/liquid interfaces with X-ray standing waves. *Science*, 250(4977):69–74, October 1990.

[4] H. D. Abruna, J. H. White, G. M. Bommarito, M. J. Albarelli, D. Acevedo, and M. J. Bedzyk. Structural studies of electrochemical interfaces with X-rays. *Rev. Sci. Instrum. (USA)*, 60(7):2529–32, July 1989.

[5] H.D. Abruña, J.M. Feliu, J.D. Brock, L.J. Buller, E. Herrero, J. Li, R. Gómez, and A. Finnefrock. Anion and electrode surface structure effects on the deposition of metal monolayers: Electrochemical and time-resolved surface diffraction studies. *Electrochim. Acta*, (in press).

[6] R. Adžić. In H. Gerisher and C. Tobias, editors, *Advances in Electrochemistry and Electrochemical Engineering*, volume 13, page 159. Wiley and Sons, New York, 1978.

[7] R.R. Adzic. Electrocatalysis on surfaces modified by foreign metal adatoms. *Israel Journal of Chemistry*, 18(1):166–81, 1979.

[8] Neil W. Ashcroft. Statistical mechanics. lecture notes, spring 1993.

[9] Neil W. Ashcroft and N. David Mermin. *Solid State Physics*, page 100. In [13], 1976.

[10] Neil W. Ashcroft and N. David Mermin. *Solid State Physics*, page 86. In [13], 1976.

[11] Neil W. Ashcroft and N. David Mermin. *Solid State Physics*, chapter Appendix N. In [13], 1976.

[12] Neil W. Ashcroft and N. David Mermin. *Solid State Physics*, page 794. In [13], 1976.

[13] Neil W. Ashcroft and N. David Mermin. *Solid State Physics*. W.B. Saunders, 1976.

[14] M. Avrami. Kinetics of phase change. i. *J. Chem. Phys.*, 7:1103–1112, 1939.

[15] M. Avrami. Kinetics of phase change. ii. *J. Chem. Phys.*, 8:212–224, 1940.

[16] M. Avrami. Kinetics of phase change. iii. *J. Chem. Phys.*, 9:177–184, 1941.

[17] A.-L. Barabási and H. E. Stanley. *Fractal Concepts in Surface Growth*. Cambridge University Press, Cambridge, 1995.

[18] Allen J. Bard and Larry R. Faulkner. *Electrochemical Methods: Fundamentals and Applications*, page 9. In [24], 1980.

[19] Allen J. Bard and Larry R. Faulkner. *Electrochemical Methods: Fundamentals and Applications*, page 505. In [24], 1980.

[20] Allen J. Bard and Larry R. Faulkner. *Electrochemical Methods: Fundamentals and Applications*, page 510. In [24], 1980.

[21] Allen J. Bard and Larry R. Faulkner. *Electrochemical Methods: Fundamentals and Applications*, page 563. In [24], 1980. Figure 13.4.2.

[22] Allen J. Bard and Larry R. Faulkner. *Electrochemical Methods: Fundamentals and Applications*, page 60. In [24], 1980.

[23] Allen J. Bard and Larry R. Faulkner. *Electrochemical Methods: Fundamentals and Applications*, pages 500–515. In [24], 1980.

[24] Allen J. Bard and Larry R. Faulkner. *Electrochemical Methods: Fundamentals and Applications*. Wiley, 1980.

[25] Allen J. Bard and Larry R. Faulkner. *Electrochemical Methods: Fundamentals and Applications*, pages 128–131. In [24], 1980.

[26] Allen J. Bard and Larry R. Faulkner. *Electrochemical Methods: Fundamentals and Applications*, pages 121–127. In [24], 1980.

[27] Allen J. Bard and Larry R. Faulkner. *Electrochemical Methods: Fundamentals and Applications*, page 51. In [24], 1980.

[28] Allen J. Bard and Larry R. Faulkner. *Electrochemical Methods: Fundamentals and Applications*, pages 142–146. In [24], 1980.

[29] Allen J. Bard and Larry R. Faulkner. *Electrochemical Methods: Fundamentals and Applications*, page 515. In [24], 1980.

[30] Allen J. Bard and Larry R. Faulkner. *Electrochemical Methods: Fundamentals and Applications*, chapter 12.1. In [24], 1980.

[31] Allen J. Bard and Larry R. Faulkner. *Electrochemical Methods: Fundamentals and Applications*, pages 521–523. In [24], 1980.

[32] U. Bergmann, D.P. Siddons, and J.B. Hastings. Time-dependent polarization in Mössbauer experiments with synchrotron radiation. *Hyperfine Interactions*, 92(1-4):1113–21, November 1994.

[33] A. Bewick and B. Thomas. *J. Electroanal. Chem.*, 70:239, 1976.

[34] J. O'M. Bockris, M. A. Devanathan, and K. Müller. *Proc. R. Soc.*, A274:55, 1963. Cited in Brett and Brett.

[35] G. M. Bommarito, D. Acevedo, J. F. Rodriguez, and H. D. Abru na. *In-Situ* x-ray standing wave study of Cu UPD on an iodine covered surface. In J. Gordon and A. Davenport, editors, *Symposium on X-ray Methods in Electrochemistry*, page 125. The Electrochemical Society, Pennington, NJ, 1972.

[36] Itamar Borukhov, David Andelman, and Henri Orland. Steric effects in electrolytes: A modified Poisson-Boltzmann equation. *Phys. Rev. Lett.*, 79(3):435–438, July 1997.

[37] R.N. Bracewell. *The Fourier Transform and its Applications.* McGraw-Hill, New York, 1986.

[38] Christopher M.A. Brett and Ana Maria Oliveira Brett. *Electrochemistry: Principles, Methods, and Applications*, page 52. In [42], 1993.

[39] Christopher M.A. Brett and Ana Maria Oliveira Brett. *Electrochemistry: Principles, Methods, and Applications*, pages 44–54. In [42], 1993.

[40] Christopher M.A. Brett and Ana Maria Oliveira Brett. *Electrochemistry: Principles, Methods, and Applications*, pages 138–140. In [42], 1993.

[41] Christopher M.A. Brett and Ana Maria Oliveira Brett. *Electrochemistry: Principles, Methods, and Applications*, pages 85–90. In [42], 1993.

[42] Christopher M.A. Brett and Ana Maria Oliveira Brett. *Electrochemistry: Principles, Methods, and Applications*. Oxford Univ. Press, 1993.

[43] Christopher M.A. Brett and Ana Maria Oliveira Brett. *Electrochemistry: Principles, Methods, and Applications*, page 22. In [42], 1993.

[44] Christopher M.A. Brett and Ana Maria Oliveira Brett. *Electrochemistry: Principles, Methods, and Applications*, page 137. In [42], 1993.

[45] J.D. Brock, A.C. Finnefrock, K.L. Ringland, and E. Sweetland. Detailed structure of a charge-density wave in a quenched random field. *Physical Review Letters*, 73(26):3588–91, December 1994.

[46] Joel D. Brock. *X-ray Scattering Study of Bond Orientational Order in Liquid Crystal Films*. PhD thesis, Massachusetts Institute of Technology, May 1987.

[47] Joel D. Brock. *X-ray Scattering Study of Bond Orientational Order in Liquid Crystal Films*. PhD thesis, Massachusetts Institute of Technology, May 1987.

[48] Joel D. Brock. Linearized langmuir nucleation model. Unpublished, 1997.

[49] F. Brossard, V. H. Etgens, and A. Tadjeddine. In situ surface X-ray diffraction using a new electrochemical cell optimised for third generation synchrotron light sources. *Nuclear Instruments and Methods in Physics Research B*, 129:419–422, 1997.

[50] Stanley Bruckenstein and Barry Miller. Unraveling reactions with rotating electrode. *Accounts of Chemical Research*, 10:54–61, 1977.

[51] E. Budevski, G. Staikov, and W.J. Lorenz. *Electrochemical Phase Formation and Growth: An Introduction to the Initial Stages of Metal Deposition*. VCH Publ., Weinheim, 1996.

[52] Lisa Jean Buller. *Electrochemical and X-ray Studies of the Structure and Dynamics of Deposition of Metal Monolayers*. PhD thesis, Cornell University, August 1997.

[53] C. T. Chantler. *J. Phys. Chem. Ref. Data*, 24:71, 1995.

[54] D. L. Chapman. *Phil. Mag.*, 25:475, 1913. Cited in Brett and Brett.

[55] Ruel Vance Churchill. *Operational Mathematics*. McGraw-Hill, New York, 1971. Cited in [48].

[56] R. Coisson. X-ray sources. In M. Schlinker, M. Fink, J.P. Goedgebuer, C. Malgrange, J. Ch. Viénot, and R.H. Wade, editors, *Imaging Processes and Coherence in Physics*, pages 51–56. Springer-Verlag, Berlin, 1980.

[57] B.D. Cullity. *Elements of X-Ray Diffraction*. Addison-Wesley, Reading, Massachusetts, second edition, 1978.

[58] B.D. Cullity. *Elements of X-Ray Diffraction*, page 112. In [57], second edition, 1978.

[59] B.D. Cullity. *Elements of X-Ray Diffraction*, page 392. In [57], second edition, 1978.

[60] B.D. Cullity. *Elements of X-Ray Diffraction*, chapter Appendix 12. In [57], second edition, 1978.

[61] B.D. Cullity. *Elements of X-Ray Diffraction*, pages 135–139. In [57], second edition, 1978.

[62] B.D. Cullity. *Elements of X-Ray Diffraction*, page 14. In [57], second edition, 1978.

[63] B.D. Cullity. *Elements of X-Ray Diffraction*, pages 135–139. In [57], second edition, 1978.

[64] G.J. Edens, X. Gao, and M.J. Weaver. *J. Electroanal. Chem.*, 375:357, 1994.

[65] A.C. Finnefrock, L.J. Buller, K.L. Ringland, J.D. Brock, and H.D. Abruña. Time-resolved surface x-ray scattering study of surface ordering of electrodeposited layers. *Journal of the American Chemical Society*, 119:11703–11704, December 1997.

[66] A.C. Finnefrock, L.J. Buller, K.L. Ringland, P.D. Ting, H.D. Abrunar, and J.D. Brock. Time-resolved measurements of overlayer ordering in electrodeposition. In P. C. Andricacos, S. G. Corcoran, J.-L. Delplancke, T. P. Moffat, and P. S. Searson, editors, *Electrochemical Synthesis and Modification of Materials. Symposium*, volume 451, pages 49–55. Mater. Res. Soc; Pittsburgh, PA, USA, 1997.

[67] Luigi Galvani. *Commentary on the effect of electricity on muscular motion; a translation of Luigi Galvani's De viribus electricitatis in motu musculari commentarius.* E. Licht, Cambridge, Mass., 1953. English translation.

[68] Luigi Galvani. *Opere scelte ... A cura di Gustavo Barbensi.* Unione tipografico editrice torinese, Torino, Italy, 1967. Annotated copy of original. In Italian.

[69] Doon Gibbs, B. M. Ocko, D. M. Zehner, and S. G. J. Mochrie. Absolute x-ray reflectivity study of the Au(100) surface. *Phys. Rev. B*, 38(11):7303–7310, 1988.

[70] N. Goldenfeld. *Lectures on Phase Transitions and the Renormalization Group*, page 261. Addison-Wesley, 1992.

[71] R. Gómez, J.M. Feliu, and H. D. Abruña. *Langmuir*, 10:4315, 1994.

[72] R. Gómez, H. S. Yee, G. M. Bommarito, F. M. Feliu, and H. D. Abru na. Anion effects and the mechanism of Cu UPD on Pt(111): X-ray and electrochemical studies. *Surf. Sci.*, 335:101, 1995.

[73] G. Gouy. *Compt. Rend.*, 149:654, 1910. Cited in Brett and Brett.

[74] D. C. Grahame. *Chem. Rev.*, 41:441, 1947. Cited in Brett and Brett.

[75] G. Grübel, K. G. Huang, Doon Gibbs, D. M. Zehner, A. R. Sandy, and S. G. J. Mochrie. *Phys. Rev. B*, 48:18119, 1993.

[76] T. Hachiya, H. Honbo, and K. Itaya. *J. Electroanal. Chem.*, 315:275, 1991.

[77] Herman and Winick, editors. *Synchrotron Radiation Science: A Primer.* World Scientific.

[78] E. Herrero, L.J. Buller, J. Li, A.C. Finnefrock, A.B. Solomón, C. Alonso, J.D. Brock, and H.D. Abruña. Electrodeposition dynamics: Electrochemical and x-ray scattering studies. *Electrochim. Acta*, (in press).

[79] M. H. Hölzle, U. Retter, and D. M. Kolb. The kinetics of structural changes in Cu adlayers on Au(111). *J. Electroanal. Chem.*, 371:101–109, 1994.

[80] M. H. Hölzle, V. Zwing, and D. M. Kolb. The influence of steps on the deposition of Cu onto Au(111). *Electrochim. Acta*, 40(10):1237–1247, 1995.

[81] J.D. Jackson. *Classical Electrodynamics*, page 516. In [83], second edition, 1975.

[82] J.D. Jackson. *Classical Electrodynamics*, page 679. In [83], second edition, 1975.

[83] J.D. Jackson. *Classical Electrodynamics*. John Wiley & Sons, New York, second edition, 1975.

[84] J.D. Jackson. *Classical Electrodynamics*, pages 281–282. In [83], second edition, 1975.

[85] J.D. Jackson. *Classical Electrodynamics*, pages 284–288. In [83], second edition, 1975.

[86] M. Kardar, G. Parisi, and Y. Zhang. Dynamic scaling of growing interfaces. *Phys. Rev. Lett.*, 56:889, 1986.

[87] Kwang-Je Kim. Characteristics of synchrotron radiation. In Douglas Vaughn, editor, *X-Ray Data Booklet*, chapter 4. Lawrence Berkeley Laboratory, April 1986.

[88] James B. Knight, Ashvin Vishwanath, James P. Brody, and Robert H. Austin. Hydrodynamic focusing on a silicon chip: Mixing nanoliters in microseconds. *Phys. Rev. Lett.*, 80(17):3863–3866, April 1998.

[89] D. Kolb. In H. Gerisher and C. Tobias, editors, *Advances in Electrochemistry and Electrochemical Engineering*, volume 11, page 125. Wiley and Sons, New York, 1978.

[90] D. M. Kolb, A. Jaff-Golze, and M. S. Zei. *Dechema Monographien*, 102:53–64, 1986.

[91] J. Li and H. D. Abruña. *J. Phys. Chem.*, 101:244, 1997.

[92] O.M. Magnussen, J. Hotlos, R.J. Nichols, D.M. Kolb, and R.J. Behm. Atomic structure of Cu adlayers on Au(100) and Au(111) electrodes observed by in situ scanning tunneling microscopy. *Physical Review Letters*, 64(24):2929–32, June 1990.

[93] S. Manne, P.K. Hansma, J. Massie, V.B. Elings, and A.A. Gewirth. *Science*, 251:183, 1991.

[94] N. Marković and P. N. Ross. Effect of anions on the underpotential deposition of Cu on Pt(111) and Pt(100) surfaces. *Langmuir*, 9(2):580–590, 1993.

[95] H. Matsumoto, J. Inukai, and M. Ito. *J. Electroanal. Chem.*, 379:223, 1994.

[96] Donald A. McQuarrie. *Statistical Mechanics*, page 87. In [100], 1976.

[97] Donald A. McQuarrie. *Statistical Mechanics*, chapter 20. In [100], 1976.

[98] Donald A. McQuarrie. *Statistical Mechanics*, chapter 15. In [100], 1976.

[99] Donald A. McQuarrie. *Statistical Mechanics*, pages 513–514. In [100], 1976.

[100] Donald A. McQuarrie. *Statistical Mechanics*. Harper Collins, New York, NY, 1976.

[101] O.R. Melroy, M.F. Toney, G.L. Borges, M.G. Samant, J.B. Kortright, P.N. Ross, and L. Blum. *Phys. Rev. B*, 38:10962, 1988.

[102] R. Michaelis, M. S. Zei, R. S. Zhai, and D. M. Kolb. The effect of halides on the structure of copper underpotential-deposited onto Pt(111): a low-energy electron diffraction and X-ray photoelectron spectroscopy study. *J. Electroanal. Chem.*, 339:299–310, 1992.

[103] Anthony D. Novaco and John P. McTague. Orientational epitaxy – the orientational ordering of incommensurate structures. *Phys. Rev. Lett.*, 38(22):1286, 1977.

[104] B. M. Ocko, O. M. Magnussen, J. X. Wang, and Th. Wandlowski. One-dimensional commensurate-incommensurate transition: Bromide on the Au(100) electrode. *Phys. Rev. B*, 53(12):R7654–R7657, March 1996.

[105] B. M. Ocko, J. X. Wang, and T. Wandlowski. *Phys. Rev. Lett.*, 79:1511, 1997.

[106] B. M. Ocko, Jia Wang, Alison Davenport, and Hugh Isaacs. *Phys. Rev. Lett.*, 65:1466, 1990.

[107] B.M. Ocko, G.M. Watson, and J. Wang. *J. Phys. Chem.*, 98:897, 1994.

[108] J. M. Orts, R. Gómez, J. M. Feliu, A. Aldaz, and J. Clavilier. *Electrochim. Acta*, 39:1519, 1994.

[109] V. L. Pokrovsky and A. L. Talapov. *Phys. Rev. Lett.*, 42(66), 1979.

[110] V. L. Pokrovsky and A. L. Talapov. *Theory of Incommensurate Crystals*, volume 1 of *Soviet Scientific Reviews, Supplement Series Physics*. Harwood Academic Publishers, New York, NY, 1984. translated by J. George Adashko.

[111] I. K. Robinson. Crystal truncation rods and surface roughness. *Phys. Rev. B*, 33(6):3830, 1986.

[112] J.J. Sakurai. *Advanced Quantum Mechanics.* Addison-Wesley, 1967.

[113] M. G. Samant, M. F. Toney, G. L. Borges, L. Blum, and O. R. Melroy. *Surf. Sci. Lett.*, 193:L29, 1988.

[114] Wolfgang Schmickler. *Interfacial Electrochemistry*, page 1. In [117], 1996.

[115] Wolfgang Schmickler. *Interfacial Electrochemistry*, pages 21–32. In [117], 1996.

[116] Wolfgang Schmickler. *Interfacial Electrochemistry*, pages 33–34. In [117], 1996.

[117] Wolfgang Schmickler. *Interfacial Electrochemistry.* Oxford University Press, New York, 1996.

[118] Wolfgang Schmickler. *Interfacial Electrochemistry*, pages 17–20. In [117], 1996.

[119] J. W. Schultze. *Ber. Bunsenges. Phys. Chem.*, 74:705, 1970.

[120] J. W. Schultze and K. J. Vetter. *J. Electroanal. Chem.*, 44:63, 1973.

[121] J.W. Schultze and D. Dickertmann. *Surf. Sci.*, 54:489, 1976.

[122] Christopher G. Shaw, S. C. Fain, Jr., and M. D. Chinn. Observation of orientational ordering of incommensurate argon monolayers on graphite. *Phys. Rev. Lett.*, 41(14):955, 1978.

[123] Z. Shi, S. Wu, and J. Lipkowski. *Electrochim. Acta*, 40:9, 1995.

[124] S.K. Sinha, E.B. Sirota, S. Garoff, and H.B. Stanley. X-ray and neutron scattering from rough surfaces. *Phys. Rev. B*, 38:2297, 1988.

[125] O. Stern. *Z. Elektrochem.*, 30:508, 1924. Cited in Brett and Brett.

[126] Mark Sutton. private communication.

[127] E. Sweetland, A.C. Finnefrock, W.J. Podulka, M. Sutton, J.D. Brock, D. DiCarlo, and R.E. Thorne. X-ray-scattering measurements of the transient structure of a driven charge-density wave. *Physical Review B (Condensed Matter)*, 50(12):8157–65, September 1994.

[128] S. Szabó. *Int. Rev. Phys. Chem.*, 10:207, 1991.

[129] A. Tadjeddine, G. Tourillon, and D. Guay. *Electochim. Acta*, 36:1859, 1991.

[130] Saul Teukolsky. Properties of synchrotron radiation. handout for Physics 561, Cornell University, 1992.

[131] I. M. Tidswell, C. A. Lucas, N. M. Markovic, and P. N. Ross. Surface-structure determination using anomalous X-ray scattering: underpotential deposition of copper on Pt(111). *Phys. Rev. B*, 51(15):10205–8, April 1995.

[132] M.F. Toney, J.G. Gordon, M.G. Samant, G.L. Borges, O. Melroy, L.-S. Kau, D.G. Wiesler, D. Yee, and L.B. Sorensen. *Phys. Rev. B*, 42:5594, 1990.

[133] M.F. Toney, J.N. Howard, J. Richer, G.L. Borges, J.G. Gordon, O.R. Melroy, D. Yee, and L.B. Sorensen. *Phys. Rev. Lett.*, 75:4772, 1995.

[134] Richard D. Varjian. Electrolytic processing. *Interface*, 3(3):24–28, Fall 1994.

[135] I. Villegas and J. L. Stickney. *J. Electrochem. Soc.*, 138:1310, 1991.

[136] I. Villegas and J. L. Stickney. *J. Electrochem. Soc.*, 139:686, 1992.

[137] H. L. F. von Helmholtz. *Ann. Physik*, 89:211, 1853. Cited in Brett and Brett.

[138] H. L. F. von Helmholtz. *Ann. Physik*, 7:337, 1879. Cited in Brett and Brett.

[139] J. Wang, A.J. Davenport, H.S. Isaacs, and B.M. Ocko. *Science*, 255:1416, 1992.

[140] J. Wang, B.M. Ocko, A.J. Davenport, and H.S. Isaacs. *Phys. Rev. B*, 46:10321, 1992.

[141] B.E. Warren. *X-ray Diffraction*, chapter 1. In [148], 1990.

[142] B.E. Warren. *X-ray Diffraction*, pages 7–12. In [148], 1990.

[143] B.E. Warren. *X-ray Diffraction*, chapter Appendix 4 and 5. In [148], 1990.

[144] B.E. Warren. *X-ray Diffraction*, pages 331–332. In [148], 1990.

[145] B.E. Warren. *X-ray Diffraction*, pages 35–38. In [148], 1990.

[146] B.E. Warren. *X-ray Diffraction*, chapter 11. In [148], 1990.

[147] B.E. Warren. *X-ray Diffraction*, pages 316–320. In [148], 1990.

[148] B.E. Warren. *X-ray Diffraction*. Dover, 1990.

[149] J. H. White and H. D. Abruña. *J. Phys. Chem.*, 94:894, 1990.

[150] J. H. White and H. D. Abruña. *J. Electroanal. Chem.*, 300:521, 1991.

[151] A. J. C. Wilson, editor. *International Tables for X-Ray Crystallography*, chapter 6.1. Volume C of Wilson [152], second edition, 1995.

[152] A. J. C. Wilson, editor. *International Tables for X-Ray Crystallography*, volume C. Kluwer Academic Publishers, for the International Union of Crystallography, Norwell, Massachusetts, USA, second edition, 1995.

[153] T.A. Witten and L.M. Sander. Diffusion-limited aggregation, a kinetic critical phenomenon. *Phys. Rev. Lett.*, 47:1400, 1981.

[154] T.A. Witten and L.M. Sander. Diffusion-limited aggregation. *Phys. Rev. B*, 27:5686, 1983.

[155] S. Wu, J. Lipkowski, T. Tyliszczak, and A. P. Hitchcock. Effect of anion adsorption on early stages of copper electrocrystallization at Au(111) surface. *Prog. Surf. Sci. (UK)*, 50(1):227–36, September–December 1995.

[156] H. S. Yee and H. D. Abruña. *Langmuir*, 9:2460, 1993.

[157] H. S. Yee and H. D. Abruña. *J. Phys. Chem. B*, 97:6278, 1993.

[158] P. Zelenay, M. Gamboa-Aldeco, G. Horányi, and A. Wieckowski. *J. Electroanal. Chem.*, 357:307, 1993.